AIAA 2019-2020 Undergraduate Team RFP
High Capacity Short Range Transport Aircraft

Final Design Report

Nicolas Alvarado, Ben Baker, Joshua Daniel, Charlie Rovin, Sejal Sahu, Weizhuo Wang, Jack Wu
Department of Aerospace Engineering
University of Illinois at Urbana-Champaign, Urbana, Illinois, 61801

Team Mustang
AE443 Aerospace Systems Design II

Faculty Advisor: Dr. Jason Merret | AIAA Member #155270
Department of Aerospace Engineering
University of Illinois at Urbana-Champaign, Urbana, Illinois, 61801

Date of Submission: May 13, 2020

I. The Team

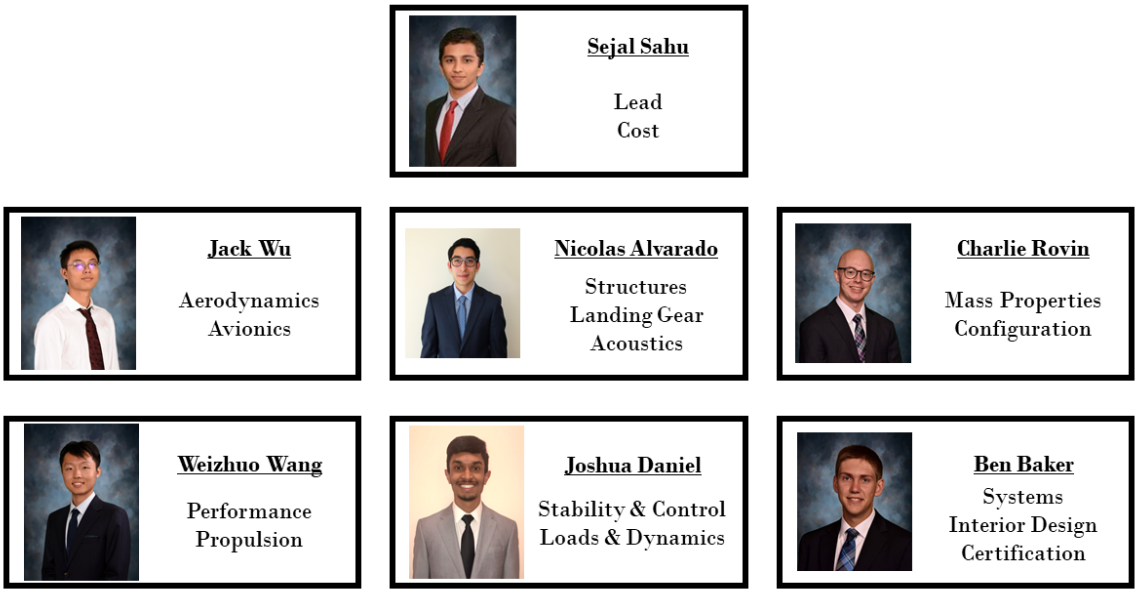

Fig. 1 Team members

Table 1 Member Affiliations

Name	AIAA #	Signature
Nicolas Alvarado	905262	
Ben Baker	983506	
Joshua Daniel	1109118	
Charlie Rovin	1108705	
Sejal Sahu	1086939	
Weizhuo Wang	981656	
Jack Wu	1109057	
Jason Merret (Advisor)	155270	

Contents

List of Figures

List of Tables

II. Nomenclature

a	=	Speed of Sound
α	=	Angle of attack
b	=	Span
$\frac{c}{4}$	=	Quarter Chord
C_{D0}	=	Zero-Lift Drag Coefficient
C_{Dexcr}	=	Excrescence Drag Coefficient
C_{Dflap}	=	Drag Coefficient Increment from Flap and Slat
C_{Di}	=	Induced Drag Coefficient
C_{Dtot}	=	Total Drag Coefficient
C_{Dtrim}	=	Trim Drag Coefficient
C_{Dwave}	=	Wave Drag Coefficient
C_g	=	Center of Gravity
C_{HT}	=	Horizontal Tail Volume Coefficient
C_L	=	Lift Coefficient
C_{L_α}	=	Derivative of Lift w.r.t. AoA Coefficient
$C_{l_{max}}$	=	Maximum Lift Coefficient
C_{m_α}	=	Derivative of Pitching Moment w.r.t. AoA Coefficient
$C_{m_{cg}}$	=	Moment about the C_g Coefficient
$C_{m_{\delta e}}$	=	Derivative of Pitching Moment w.r.t. δe Coefficient
C_{n_β}	=	Derivative of Yawing Moment w.r.t. Sideslip Coefficient
$C_{n_{\delta r}}$	=	Derivative of Yawing moment w.r.t. δr Coefficient
C_{n_r}	=	Derivative of Yawing Moment w.r.t. Roll Rate Coefficient
C_{l_β}	=	Derivative of Rolling Moment w.r.t. Sideslip Coefficient
$C_{l_{\delta r}}$	=	Derivative of Rolling Moment w.r.t. δr Coefficient
C_{l_r}	=	Derivative of Rolling Moment w.r.t. Roll Rate Coefficient

C_{VT}	=	Vertical Tail Volume Coefficient
δa	=	Aileron Deflection Angle
δe	=	Elevator Deflection Angle
δr	=	Rudder Deflection Angle
ϵ_α	=	Derivative of Downwash Angle w.r.t. AoA Coefficient
Γ	=	Dihedral Angle
λ	=	Taper Ratio
$\Lambda_{c/4}$	=	Quarter Chord Sweep Angle
$\Lambda_{H.L.}$	=	Hinge Line Angle
L/D	=	Lift to Drag Ratio
l_{HT}	=	Distance between C_g and Horizontal Tail Aerodynamic Center
l_m	=	Distance between C_g and Main Gear
l_n	=	Distance between C_g and Nose Gear
l_{VT}	=	Distance between C_g and Vertical Tail Aerodynamic Center
$\dot{m}$	=	Engine Mass Flow Rate
M_{dd}	=	Drag-Divergence Mach Number
M_{ult}	=	Ultimate Moment Load
ω_n	=	Natural Frequency
P_m	=	Load on Main Gear Strut
P_n	=	Load on Nose Gear Strut
$S_{flapped}$	=	Wing Flapped Area
S_{ref}	=	Wing Reference Area
t/c	=	Thickness to Chord Ratio
T	=	Thrust
$T_{1/2}$	=	Time to Half Amplitude
T_2	=	Doubling Time
T_P	=	Period
τ	=	Time Constant
v	=	Speed
$V1$	=	Decision Speed
$V2$	=	Takeoff Safety Speed
V_b	=	Design Speed for Maximum Gust Intensity
V_c	=	Design Cruise Speed
V_d	=	Design Dive Speed
Vr	=	Rotation Speed
V_{ult}	=	Ultimate Shear Load
W_E	=	Empty Weight
W_{Fuel}	=	Fuel Weight
W_{TO}	=	Takeoff Weight
ζ	=	Damping Ratio

III. Acronyms

AEO	=	All Engine Operative
APU	=	Auxiliary Power Unit
AR	=	Aspect Ratio
BFL	=	Balanced Field Length
CER	=	Cost Estimating Relationships
CFD	=	Computational Fluid Dynamics
CFR	=	Code of Federal Regulations
EIS	=	Entry Into Service
EPNdB	=	Effective Perceived Noise in Decibels
FADEC	=	Full Authority Digital Engine Control
FAR	=	Federal Aviation Regulations
FBW	=	Fly-By-Wire
FEM	=	Finite Element Method
FL	=	Flight Level
GE	=	General Electric
IFR	=	Instrument Flight Rules
ISA	=	International Standard Atmosphere
KCAS	=	Knots Calibrated Airspeed
KEAS	=	Knots Equivalent Airspeed
KTAS	=	Knots True Airspeed
LFL	=	Landing Field Length
MAC	=	Mean Aerodynamic Chord
MLW	=	Maximum Landing Weight
MRamp	=	Maximum Ramp Weight
MTOW	=	Maximum Takeoff Weight
MZFW	=	Maximum Zero Fuel Weight
OEI	=	One Engine Inoperative
OEW	=	Operating Empty Weight
OSHA	=	Occupational Safety and Health Administration
RDTE	=	Research, Design, Testing, and Evaluation
RFP	=	Request for Proposal
RR	=	Rolls-Royce
SFC	=	Specific Fuel Consumption
TOFL	=	Takeoff Field Length
TSFC	=	Thrust Specific Fuel Consumption
VFR	=	Visual Flight Rules

IV. Executive Summary

The advancement of the commercial airline industry in the coming decades comes with unique challenges. As markets in developing countries expand and worldwide air travel transitions from hub to regional routes, a new class of aircraft will be needed. This report documents the preliminary design of a high capacity short range transport aircraft as requested by the AIAA Undergraduate Challenge [1].

The formal requirements of the RFP call for an aircraft with the capability to carry 400 passengers a distance of 3,500 nmi, along with a TOFL and LFL length of 9,000 ft. The RFP has a number of other miscellaneous requirements relating to the aircraft mission. It is expected that the aircraft meet all FAA 14 CFR Part 25 specifications as well. The year of entry into service is 2029. Subsequently, developing technologies can be incorporated into the design. The RFP design objectives call for aircraft optimized for a 700 nmi mission. Operating and production cost should be minimized through sources such as fuel/energy, maintenance, personnel, manufacturing, and materials. The aircraft reliability and maintenance should also be equal or better to that of similar aircraft.

This report covers the preliminary design and sizing of Jay Jay the Jet Plane (JJJP). The JJJP features a conventional tube-and-wing design. It can carry a nominal payload of 93,400 lb to a maximum range of 3,500 nmi at a cruise speed of Mach 0.78 . The JJJP contains a fuselage length of 203 ft and in-flight wingspan of 184 ft that can fold to 171 ft on the ground. It utilizes two Rolls-Royce UltraFan engines. The MTOW and empty weight are 443,000 lb and 241,500 lb respectively. The unit price is expected to be $ 180 million and at an operating cost of $ 23,500 per hour. The JJJP is capable of meeting all RFP requirements.

Fig. 2 Jay Jay the Jet Plane (JJJP)

V. Introduction

The transition of global airline markets calls for an aircraft with a short-range high capacity mission profile. As determined by the AIAA RFP, a 400 passenger aircraft with 3,500 nmi range (optimized for 700 nmi) is to be designed. The RFP also stated that the design objectives are to minimize operating/ production cost and ensure high aircraft reliability/ maintenance.

The target group of the JJJP is low-cost airliners in emerging markets. Primarily those that aim to maximize flights across short-distance regional flights. To survive in this niche of the airline industry, there is an emphasis on minimizing costs and maximizing passengers moved. As such, the JJJP has been designed with a focus on cost from the very beginning. The JJJP contains design traits that give it an unparalleled efficiency at a competitive price point. The Rolls-Royce UltraFan engines and large wingspan provide maximum fuel economy. The aluminum airframe allows for rapid manufacturing and maintenance. Onboard auxillary systems and avionics ensure safety during all phases of flight. The interior cabin is arranged to be volume efficient for a high passenger count. And finally, the folding wingtip systems

gives the JJJP the flexibility to access Group IV airports, maximizing it's global and local access.

The JJJP is capable of carrying a 400 passenger payload a range of 3,500 nmi. Cruise speed and altitude are Mach 0.78 and 37,000 ft respectively. It has a 184 ft wingspan (171 ft folded) and 203 ft fuselage length. The MTOW and empty weight are 443,000 lb and 241,500 lb respectively. It utilizes two Rolls-Royce UltraFan engines with a maximum thrust of 62,500 lbf. The entry into service is expected to be 2029 at a unit cost of $ 180 million. A CAD model of the JJJP can be seen below in Fig. 2.

VI. Concept of Operations

The major requirements as set by the RFP are listed in Table 2 [1]. The payload, range, and TOFL/LFL requirements are the largest influencers of the aircraft design. One further requirement that was chosen to be incorporated was sizing the aircraft to fit into Group IV airports. This was to allow for increased access to regional airports.

Table 2 RFP Requirements

Type	Requirement	Comments
Payload	400 passengers + Crew (2 pilots, 8 flight attendants)	Dual class configuration
Range	3,500 nmi	With specified reserve energy
Reserves	200 nmi range to alternate airport + 30 min. hold + 5% contingency fuel	N/A
Takeoff	Maximum 9,000 ft over a 35 ft obstacle	Dry pavement, sea level ISA + 15 °C at MTOW
Landing	Maximum 9,000 ft	Dry pavement, sea level ISA + 15 °C
Approach speed	Maximum 145 KCAS	Optional requirement
Cabin pressurization	Pressurized to 8,000 ft at maximum flight altitude	N/A
Flight capabilities	Capable of VFR and IFR with an autopilot	N/A
Flight capabilities	Capable of flight in icing conditions	N/A
Certification	Meet FAA Part 25 and relevant ICAO/EASA regulations	N/A

Optimal and divert mission profiles are shown in Figure 3. There are straightforward segments such as taxi/takeoff, climb, cruise, descent, and landing/taxi. There is also the necessary capability to loiter for a certain range. This is specified as a 200 nmi range to an alternate airport, a 30 minute hold, and a 5% contingency fuel.

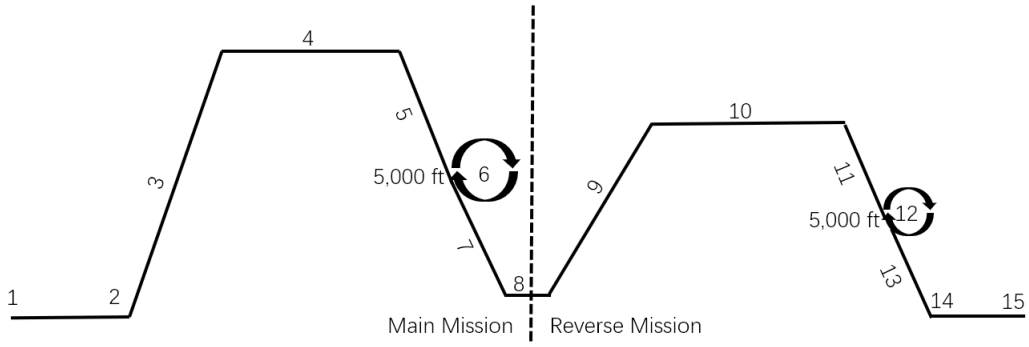

Main Mission
1 - Taxi
2 - Take off [ISA+15C]
3 - Climb + Accelerate
4 - Cruise [M0.78 @ FL350 for 3,500 nmi]
5 - Descent [To 5,000 ft]
6 - Loiter [5 min]
7 - Approach
8 - Land

Reverse Mission
9 - Divert Climb + Accelerate
10 - Divert Cruise [M0.5 @ FL150 for 200 nmi]
11 - Descent [To 5,000 ft]
12 – Loiter [35 min]
13 - Approach
14 - Land [ISA+15C]
15 - Taxi

Fig. 3 Mission profile

VII. Sizing Analysis

A. Similarity Analysis

When searching for an aircraft to use as a seed for this design, the main parameters that were taken into consideration were number of passengers and range. These two requirements have a significant impact on the overall size and performance needed for the aircraft. Furthermore, modern aircraft were chosen over older ones to reflect the technology that would be present in this design. From these criteria, the Boeing 777-200 and the Boeing 787-8 were used as the two seed aircraft when designing the JJJP. A list of all other important parameters from the seed aircraft can be seen compiled in Table 3 [2–5].

Table 3 Seed Data

	Passengers	Empty weight	Fuel Weight	Range	Aspect Ratio	Thrust
777-200	313	297,300 lb	207,700 lb	5,240 nmi	8.68	77,200 lbf
787-8	242	264,500 lb	223,378 lb	7,355 nmi	9.67	64,000 lbf

For the aircraft that is being designed, a minimum of 400 passengers needs to be carried over a range of 3,500 nmi.

From Table 3 the Boeing 777-200 more closely aligns with these specifications. However, both seeds were used to do the initial sizing process to verify that the dimensions would converge to similar values and that the sizing program is working properly.

B. Initial Sizing and Constraint Analysis

In order to quickly test out the effect of various parameters, a MATLAB sizing program was developed to conduct an iterative sizing analysis, pragmatically. Specifically, the program first took in the requirements, seed parameters, and starting guesses of the design parameters. It then applied the sizing equations from Raymer [6] and Roskam [7] to update the design parameters until it converged.

The program repeated the iterations for different parameters such as cruise mach number, altitude, wing area, aspect ratio, etc. Since these parameters were all varied across sizing iterations, it was critical to visualize the interactions between the parameters. Therefore the program plotted a contour, allowing decisions to be made on the optimal parameters for the preliminary design.

The constraints shown in Table 4 define the design space. These constraints were derived from the requirements specified in the RFP in addition to operational requirements, determined by the group.

Table 4 Constraint & Requirements

Parameter	Value
Range	Min. 3,500 nmi
BFL @ ISA+15°C	Max. 9,000 ft
Landing Distance	Max. 9,000 ft
Loiter	30 min
Service Ceiling	Min. 43,000 ft
Payload Weight	Min. 94,300 lb
Span	Max. 170.5 ft

The constraints listed presented a valid design region in the constraint diagram in Fig. 4. The diagram is limited by maximum cruise speed, takeoff distances, landing distances, and cruise limitations. The maximum cruise speed used is mach 0.9. The blue cross denotes the designed point of JJJP. Specifically at maximum takeoff weight, the thrust to weight ratio is 0.282, with wing loading at 114 psf. At this point, lowest thrust is required and penalties from takeoff thrust and extra weight from large wing area are both minimized.

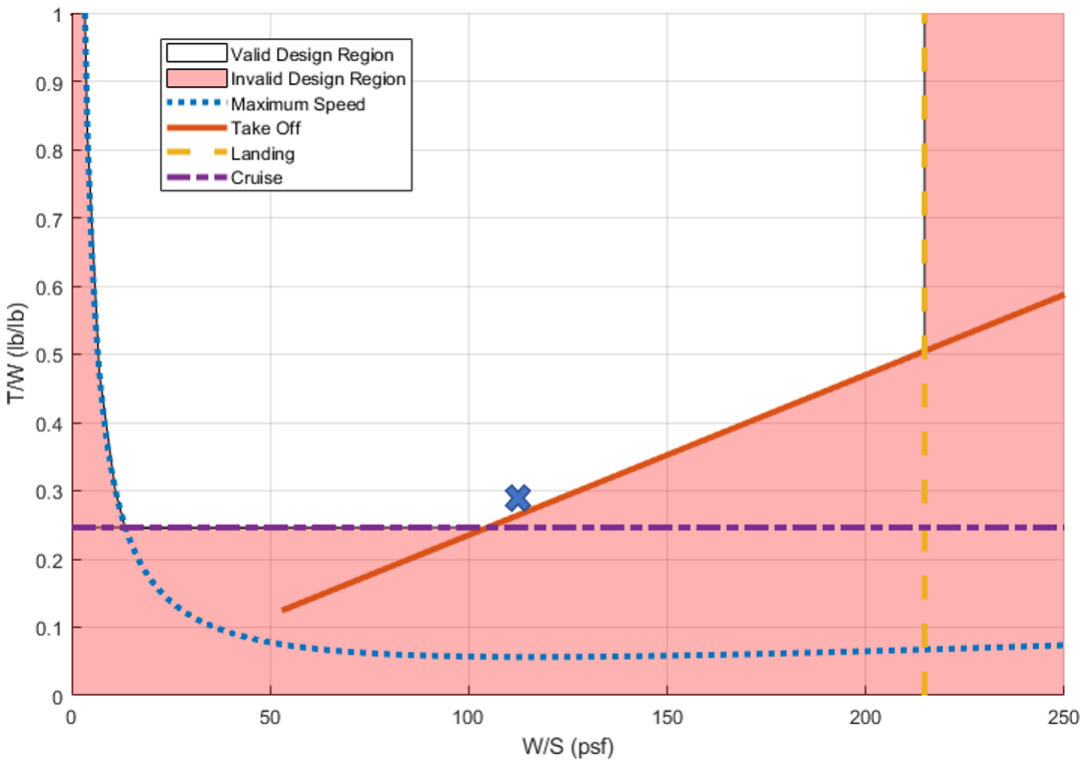

Fig. 4 Constraint diagram

C. Trade Studies

A set of trade studies were conducted to determine an optimal design. The qualifications for success in these studies were (1) minimize fuel weight to reduce operating cost and (2) minimize empty weight to reduce manufacturing cost. To determine fixed geometry parameters and flight conditions of the aircraft that optimize for the aforementioned qualifications of success, the following set of values were varied: wing aspect ratio, wing area, wing sweep, wing taper, cruise speed, and cruise altitude.

By utilizing rough estimates, a lifetime cost model was incorporated into the trade studies. An empty weight to unit cost estimation of $850 per pound and fuel cost to fuel weight of $1.12 per pound were added to the sizing code outputs. After rerunning the sizing code, with this cost model implemented, the contour in Fig. 5 was produced. This contour illustrates lifetime cost.

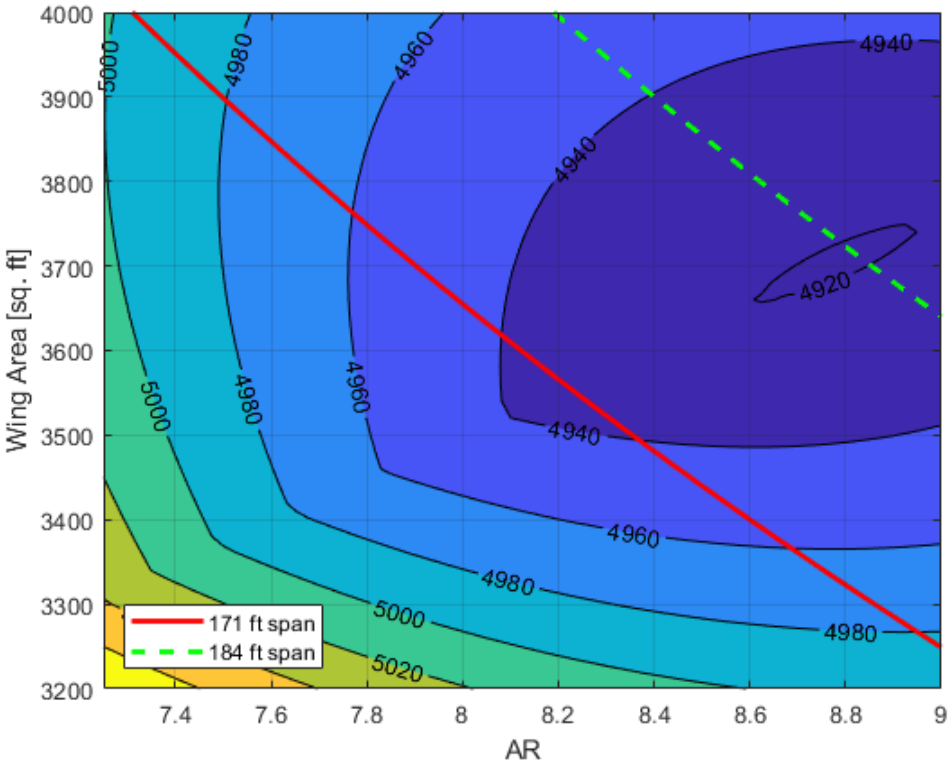

Fig. 5 Unit + fuel cost (USD millions) of AR vs. wing area

A key takeaway from this analysis was that rather than having a 171 ft fixed wingspan, it would be more economically viable to have a 184 ft wingspan with wingtips that fold to 171 ft. This is assuming that the folding wingtip system would weigh under approximately 2,000 lb. Based upon further trade studies for different parameters, final optimal values were chosen, as presented in Table 5.

Table 5 Optimal Parameters

Parameter	Value
Aspect ratio	8.7
Wing area	3,880 ft^2
Wing sweep	25 deg
Wing taper	0.15
Cruise speed	Mach 0.78
Cruise altitude	37,000 ft

The optimized parameters from Table 5 were input into the sizing program, and the aircraft model was then recomputed. The final overall aircraft parameters are shown in Table 6.

Table 6 Key Design Parameters

Parameter	Value	Parameter	Value
Passengers	400	Takeoff Thrust	62,500 lbf
Range	3500 nmi	Cruise Speed	Mach 0.78
L/D	16.3	Cruise Altitude	37,000 ft
$C_{L_{Max}}$ (high lift)	2.44	Fuselage Length	203 ft
Wingspan	184 ft	Fuselage Diameter	21 ft
Wing Area	3,880 ft^2	Empty weight	241,500 lb
Aspect Ratio	8.7	MTOW	443,000 lb
SFC	0.43 $\frac{lb}{lb\text{-}hr}$	Fuel Weight	110,000 lb

VIII. Configuration

A. Design Morphology

The aircraft configuration was originally designed in an effort to optimize for the design objectives specified in the AIAA RFP [1]. Principally, the objective of optimizing cost for a 700 nmi range mission was closely considered. To that end, considerations were made for FAA Advisory Circular AC 150/5300-13A, wherein specifications are listed for geometric layout of runways, taxiways, aprons, and other facilities at civil airports [8]. The document specifies airport design groups and their corresponding aircraft classes. Each design group is categorized by both the range of wingspans and maximum tail height that the airport can accommodate. For instance, there are approximately one dozen airports in the world that are built to accommodate aircraft within the specifications of "Group VI" [9]. A comprehensive description of airport classification is provided in Table 7 [9].

Table 7 Airport Classifications for per FAA and ICAO

FAA Advisory Circular 150/5300-13			ICAO Annex 14		
Group	Wing Span	Tail Height	Code	Wing Span	Outer Main Gear Span
Group I	0-49 ft	0-20 ft	Code A	0-15 m	0-4.5 m
Group II	49-79 ft	20-30 ft	Code B	15-24 m	4.5-6 m
Group III	79-118 ft	30-45 ft	Code C	24-36 m	6-9 m
Group IV	118-171 ft	45-60 ft	Code D	36-52 m	9-14 m
Group V	171-214 ft	60-66 ft	Code E	52-65 m	9-14 m
Group VI	214-262 ft	66-80 ft	Code F	65-80 m	14-16 m

Qualitative analysis was performed on alternative configurations, including a twin-fuselage design and a double-decker design. A twin-fuselage design initially appeared enticing from a cost standpoint, as an existing fuselage configuration (e.g. Boeing 737-800) could simply be duplicated, with a wing extending between the fuselages. Such a design, similar to Scaled Composites' Stratolaunch aircraft [10], could potentially save on both research and design costs, as well as manufacturing costs via existing tooling and production facilities. The design was ultimately abandoned due to the accelerations that would be experienced by passengers during turns, as a result of centripetal force. Additional concerns were noted in the required structures for a wing spanning between the two fuselages.

The double-decker design was abandoned due to anticipated costs associated with the structural components required to support the design and general manufacturing and transportation costs. In the same way that Airbus is required to produce a380 components at multiple factories across Europe due to the size of the components, any double-decker aircraft design may require similar manufacturing logistics. Similar to the Airbus a380, such a design would have large sections (e.g. fuselage, wings, etc.) and traditional component transportation methods would not be feasible [11].

After the initial configuration, a trade study was performed to analyze potentially novel applications of technology that would allow the aircraft to perform competitively in its class. The qualifications for the trade study were that any configuration change would need to both further optimize cost for a 700 nmi mission and be realistically implementable by the EIS date. Table 8 provides details on technologies that were studied.

Table 8 Innovative Technology Trade Study Concepts

Technology	Rationale	Technology Readiness Level (1-9) [12]
Folding Wingtips	Allows for extended wing span (subsq. lower induced drag) without exceeding current airport classification limits	8
Digital Display Instead of Windows	Removing Window Structures would save weight	3
Additive Manufactured Parts	Can create parts without excess material subsq. save weight	9

While all of the studied technologies had the potential to improve performance, it was ultimately decided that the Technology Readiness Level of the window-less configuration was too low to pursue at this time. Experts also believe that passengers simply prefer window views to digital displays [13]. In contrast, despite having a very high Technology Readiness Level, additive manufacturing was determined to be too expensive for this design, violating the qualifications of this trade study. The folding wingtips concept was accepted as both technologically realistic and expected to provide cost savings. This decision drove a wingspan configuration change from 171 ft to 184 ft. The consequence of this decision was a new wing design with a larger wing span, larger aspect ratio, and larger wing area–improving in-flight performance via lowering drag– while still allowing the aircraft to fly into Group IV airports. Analysis is presented in Section XVI to verify that the added weight of the larger wing and folding system do not result in greater performance cost than just keeping the original, smaller wing.

1. Modeling

The original design, created in OpenVSP, consisted of a traditional low-wing single fuselage design, as shown in Fig. 6. This design did not offer significant consideration to the nose cone or tail cone. Subsequently, they were left in arbitrary configurations based on the software's default geometry.

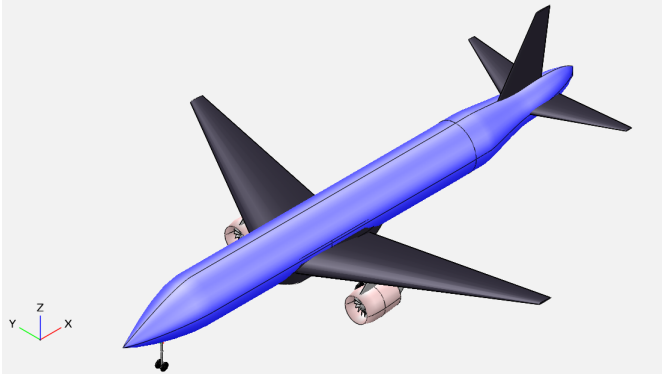

Fig. 6 Preliminary design model

The design was later migrated into the Siemens NX environment and refined to incorporate a nose and tail cone that more closely resembled those of existing high capacity aircraft, as shown in Fig. 7. This choice was made assuming that such a configuration would likely have had previous analysis performed around it, acting as a good starting point for additional refinement. Further consideration was paid to fitting internal structures in addition to simply allowing room for the requisite seating. Higher fidelity details such as control surfaces and high lift devices (ailerons, flaps, rudder, and elevators) were added to the model with the intention of undergoing further geometry changes as analysis was performed. Details such as windows, doors, and landing gear were not yet included in the model.

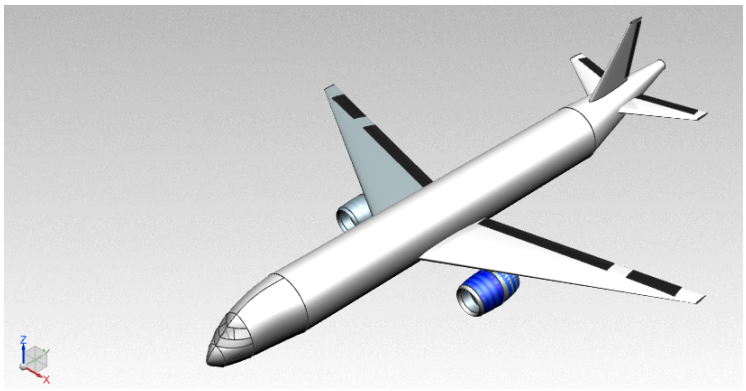

Fig. 7 Higher fidelity model based on first order analysis

As a result of in-depth analysis, presented throughout the rest of this report, in areas such as Stability and Control, Aerodynamics, Structures and Loads, etc., the configuration was further refined to include additional details such as a yehudi, landing gear, sized control surfaces and high lift devices, and other details (ref. Fig. 8). A 3-view and engineering drawing of the current design can be found on page 11 and 12, respectively.

Fig. 8 FDR configuration at cruise

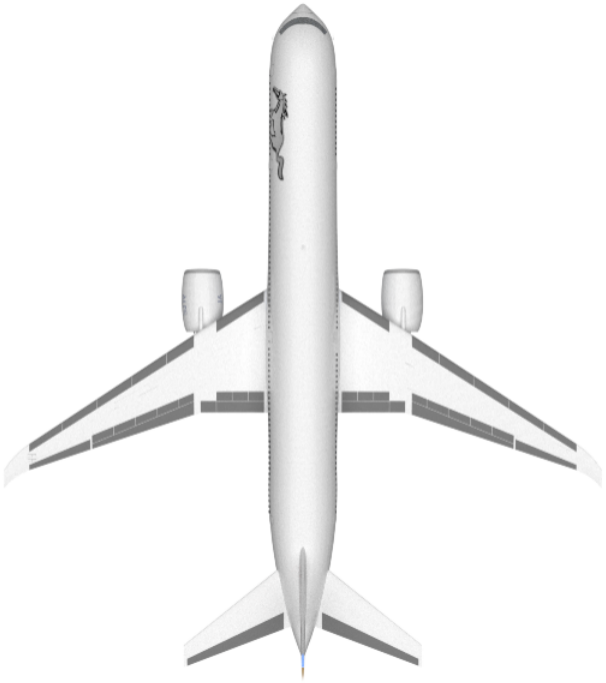

(a) Top View

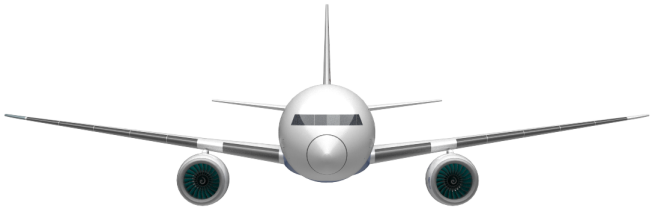

(b) Front View

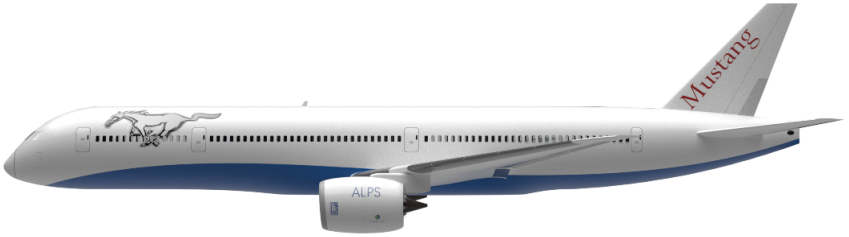

(c) Side View

Fig. 9 FDR configuration 3-view

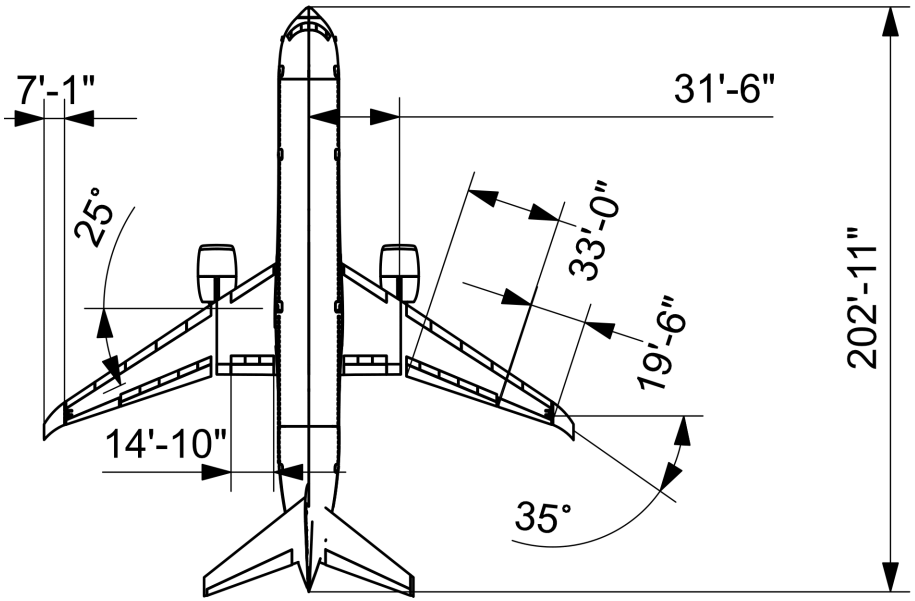

JJJP
FDR REV B
04/29/2020

Center of Gravity (x,y,z)	(102, 0, 15) [ft]
Neutral Point (1-D)	109.8 [ft]
Wing Area	3,880 [ft^2]
Wing Span (folded)	171 [ft]
Wing Twist	-3 [deg]
Nose Gear Height	10.5 [ft]
Main Gear Height	11.4 [ft]
Tail Strike Angle	15.04 [deg]
Vtail Moment Arm	22 [ft]
Htail Moment Arm	76 [ft]

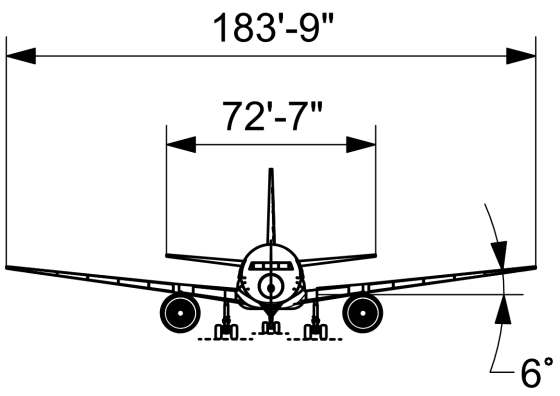

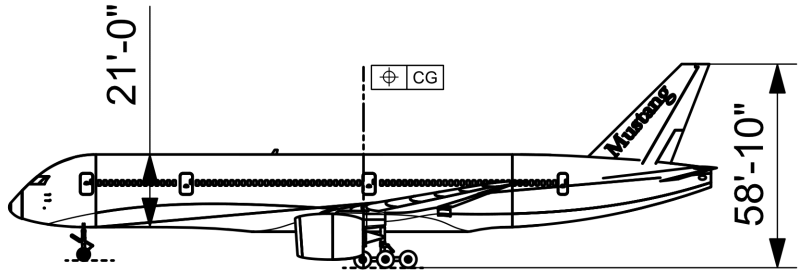

Fig. 10 Engineering drawing

With consideration to manufacturing costs, a traditional low-wing single body fuselage design was selected, as shown on page 11. **Note:** details on the landing gear can be found in Section XV.A. Key configuration parameters are presented in Table 9.

Table 9 Notable Configuration Parameters

Parameter	Value
Fuselage Length	203 ft
Fuselage Diameter (in "barrel" section)	21 ft
$\frac{C}{4}$ Sweep	25 deg
Taper	.15
Wing Span	183.75 ft
Wing Area	3,880 ft^2
Wing MAC	24.58 ft
Horizontal Tail Area	1055 ft^2
Vertical Tail Area	468 ft^2

B. Pilot Viewing Angles

Pilot viewing angles are a necessary part of the design and regulatory process for development of any aircraft because of the need for the pilot to see outside to operate the aircraft. This has been taken into account in the design of the JJJP. More specifically, this is proved by meeting the Advisory Circular 25.773-1 that clarifies 14 CFR §25.773 [14]. For simplification, the minimum angles required for viewing in the vertical and horizontal direction will be used. If the JJJP meets the minimum required angles, then it should be certifiable in terms of the regulations. Another important note is that although this model uses a human height of 5'8", with seat adjustments any height within the range specified by the FAA could pass the viewing angle requirements. Table 10 shows the minimum viewing angles needed, and Fig 11 shows that all requirements are achieved on the JJJP.

Table 10 Required Pilot Viewing Angles

Pilot View	Above Center	Below Center	Left of Center	Right of Center	Left Unobstructed	Right Unobstructed
Angle	35 deg	27 deg	120 deg	20 deg	20 deg	20 deg

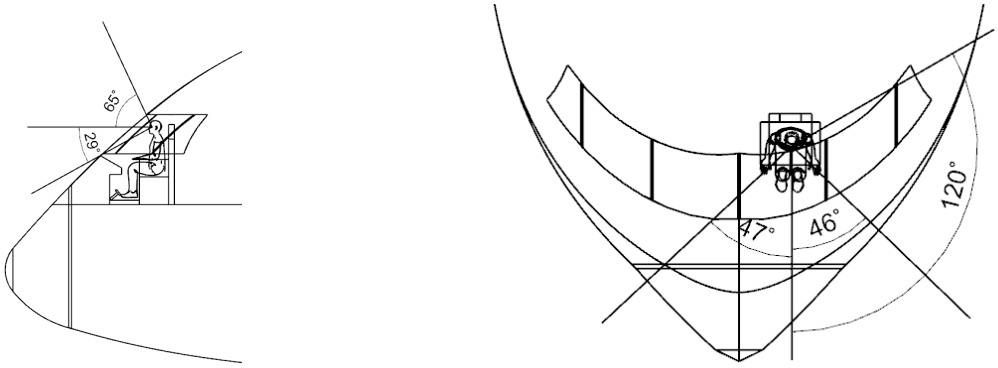

(a) Vertical viewing angles **(b) Horizontal viewing angles**

Fig. 11 Maximum pilot viewing angles

C. Interior Design Layout

The interior design of this aircraft was driven by three main objectives: Meeting the RFP requirements for passenger counts, meeting FAA safety and evacuation requirements, and making sure the passenger experience is positive.

The RFP had a few specific requirements that had to be complied with in the design of the interior. There were to be at least 50 business class seats with a pitch of 36 in and a width of 21 in .There were also to be at least 350 economy seat with a pitch of 32 in and a width of 18 in [1]. These were all complied with according to Fig. 12 . The decision was made to stay at the minimum seat dimension values outlined by the RFP because these values are more in line with the seat standards of other primarily short-haul airlines.

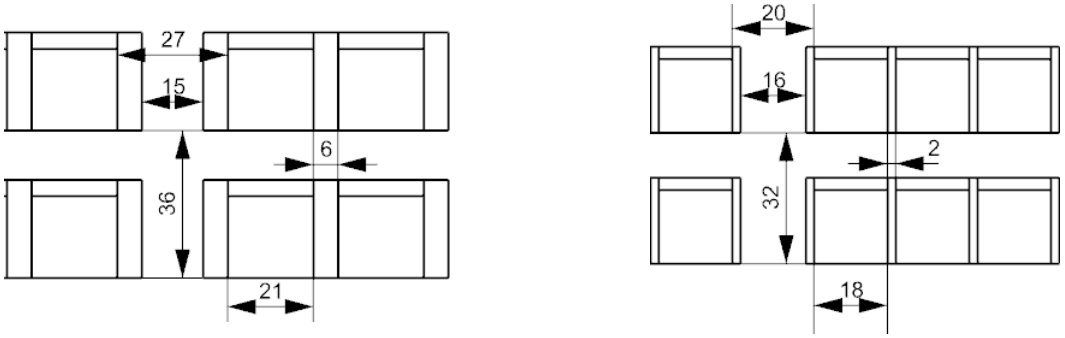

(a) Business class seat specifications **(b) Economy class seat specifications**

Fig. 12 Seat specifications for both seat classes

The next step was to fulfill the requirements from the FAA on the interior of the aircraft. Mainly, these requirements are 14 CFR §25.815 for required aisle width, and 14 CFR §25.803 with clarifying regulations 14 CFR §25.807 and 14 CFR §121.291 for evacuation of the aircraft. Looking again at Fig. 12, it can be seen that the aisle width for business class is 15 in on the ground and 27 in above the arm rest. For the economy class, the aisle is 16 in on the ground and 20

in. This meets the minimum requirements according to 14 CFR §25.815. For evacuation regulations, the focus was mostly put on the type of exits needed in order to evacuate under the required 90 seconds with the consideration of a possibility of fire on part of the aircraft. The JJJP employs three Class A exits per side and one Class B per side. Per 14 CFR §25.807, Class A exits can evacuate up to 110 passengers, and Class B exits can evacuate up to 75 passengers. This means in total the airplane should be certifiable to evacuate in total 810 passengers or 405 passengers on one side in case of fire on one side.

The layout of our interior seating is a 2-3-2 configuration for business class, and a 3-4-3 for the economy class. This was done in order to balance passenger comfort, passenger count, and meeting requirements. Based on qualitative research on seat configurations of different aircraft and airline companies, it was found that both configurations were one of the most popular for their respective classes. This analysis, along with these classes being efficient at getting more seats into a given area, makes this setup the best choice for the JJJP. An image of the overall seating configuration that could be used for seat marketing is shown in Fig. 13. Please note that this image is not completely sized dimensionally, but instead depicts general locations of the interior elements.

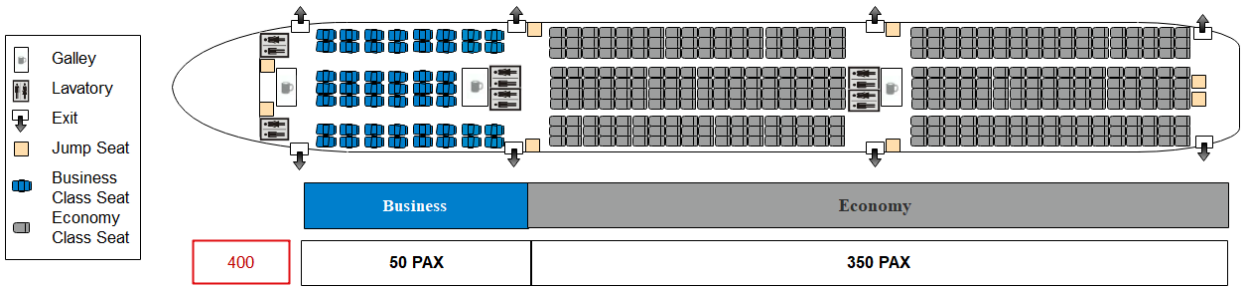

Fig. 13 Seating chart for the JJJP

All dimensions for the interior of the aircraft are shown below in Fig. 14 in inches. Not shown in the figure are two doors, two bathrooms, two jump seats, and one galley space near the front of the aircraft. These will be contained in the nose section of the aircraft behind the cockpit, so they were not included in the cabin drawing. Also not shown on Fig. 14 is the length of the baggage compartments. The forward baggage compartment has a length of 62 ft, and the aft baggage compartment has a length of 64.5 ft with the last 12 ft tapering down in the tail section. For reference, this corresponds to a total of 24 LD3 containers in the forward baggage compartment, and 20 LD3 containers in the aft baggage compartment. LD3 containers are common containers used in the airline industry for baggage. These containers have a maximum width of 79 in and a height of 64 in [15]. With the average width in the baggage compartment being 170 in, there is more than enough room to house two rows of LD3 containers in the forward and aft baggage compartments.

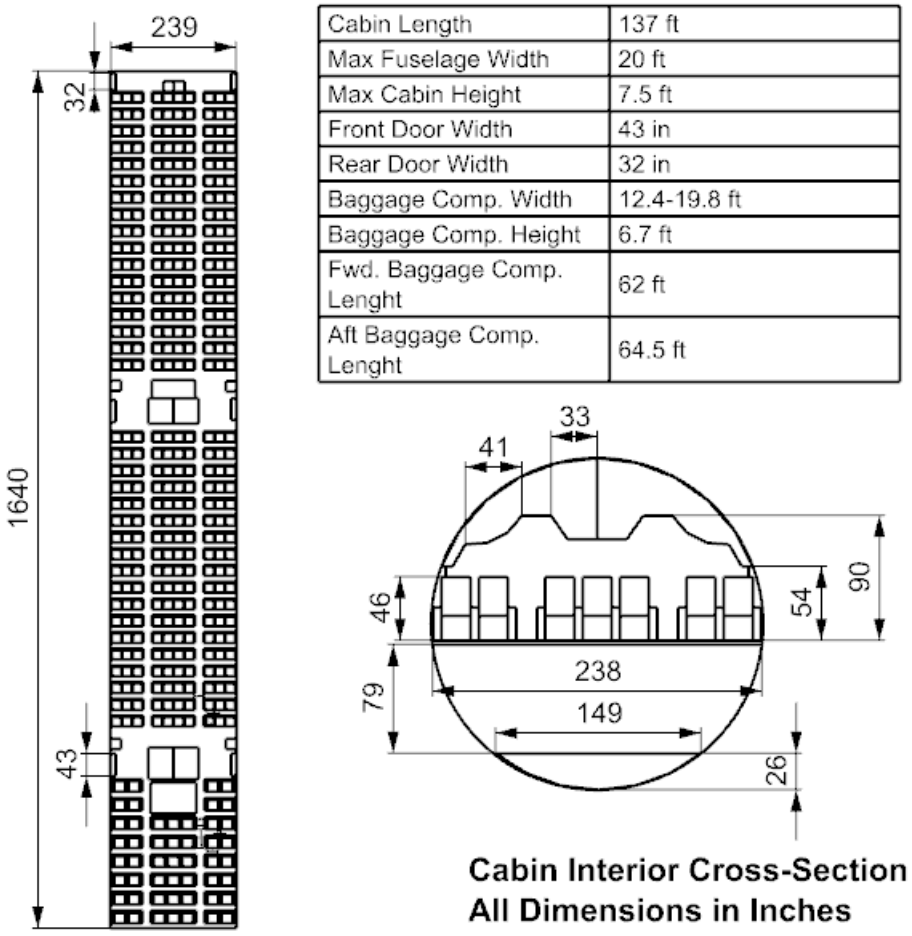

Cabin Length	137 ft
Max Fuselage Width	20 ft
Max Cabin Height	7.5 ft
Front Door Width	43 in
Rear Door Width	32 in
Baggage Comp. Width	12.4-19.8 ft
Baggage Comp. Height	6.7 ft
Fwd. Baggage Comp. Lenght	62 ft
Aft Baggage Comp. Lenght	64.5 ft

Fig. 14 2D view of seating arrangement and barrel section dimensioning

IX. Propulsion

A. Design Approach

The team's design philosophy utilizes a rubber engine approach. The engine parameters were scaled from the seed parameters according to varying thrust requirements. Specifically, parameters such as fan diameter, nacelle diameter, integrated power plant system weight, engine length, and nacelle wetted area were scaled. According to the sizing result discussed in section VII, the required total thrust was 125,000 lbf at sea level.

B. Trade Studies

At 125,000 lbf thrust requirement, turboprop technology would struggle to meet performance without great expense in weight and subsequent cost. Even with the most powerful [16] turboprop in production (Europrop TP400), the design still needs at least six engines. Electric propulsion requires carrying a very heavy battery that would not reduce weight in flight. According to Raymer [6], jet fuel has a energy density 11000 Wh/kg , while the battery has at most 600 Wh/kg.

This means the equivalent battery would weigh over 2 million pounds. This factor alone determines that electric aircraft is infeasible for this type of mission. This analysis narrows down the engine choice to turbofan or turbojet, provided the selected, subsonic cruise speed.

The design of the propulsion system is mainly concerned with factors such as fuel economy, range requirements, and cruise speed. The JJJP aims to maximize fuel economy while achieving the required range and capacity, as the demand for short-haul routes can be highly sensitive to ticket prices [17]. Considering that the aircraft will be cruising at transonic speeds, turbofan technology is a better choice than turbojet technology, since turbofan has a slower exhaust velocity and higher mass flow rate. Specifically, the highest overall efficiency is achieved when exhaust velocity equals two times the cruise velocity[6], which is closest to turbofan's exhaust speed. The high mass flow rate of turbofan also adds to the total thrust since $T = v\dot{m}$. To achieve optimal fuel economy, SFC becomes the primary factor when choosing the engine.

Four engine configurations bring extra complexity and weight to the aircraft and do not provide any real gain in fuel economy. Three engines configuration has inherent risks due to the mid-engine placement. When the failure occurs to the mid engine, it is often catastrophic (AA191 O'Hare 1979 [18]). It was then decided to use two engines to power the aircraft, each providing 62,500 pounds of thrust to meet the total thrust requirement.

C. Safety Considerations

In coordination with performance analyses, with one engine inoperative (OEI), the aircraft can meet the takeoff and landing requirements set in the RFP (9000 ft) [1]. In such a condition, the pilot should immediately abort takeoff and apply the brake if the speed is under V1 calculated in the performance section (Sec. XII). On the other hand, if the speed is above V1, the pilot should continue to take off with only one engine. In both cases, the pilot is guaranteed to have enough thrust and runway to continue takeoff or stop.

D. System Operation Over Mission Profile

To illustrate the engine operation over the designed mission, a plot of Throttle vs Time is provided below in Fig 15. The orange line denotes cruise with step climb, while blue denotes same mission without step climb. This plot includes the 3500 nmi primary mission and 200 nmi diversion. Specifically, primary mission ends at 28000 s as shown in Fig 15.

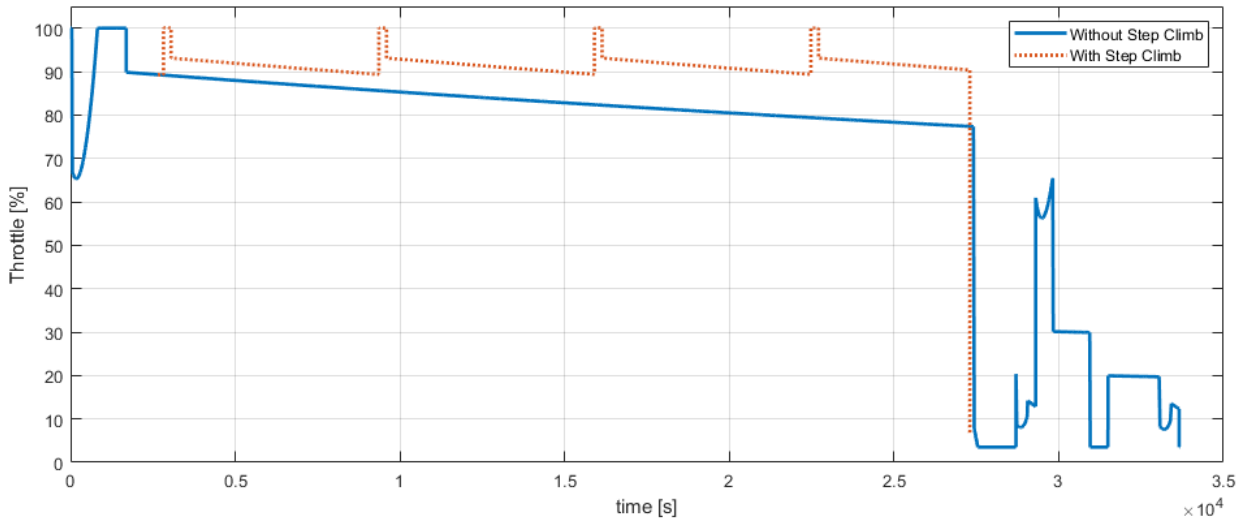

Fig. 15 Throttle used throughout the flight

From Fig 15, the JJJP is designed to cruise at 78%-90% throttle depending on the cruise condition. If step climb is used, since the aircraft will be cruise at a higher altitude with thinner air, the throttle is maintained around 90% throughout the cruise with short periods of 100% in order to climb to a higher altitude. A detailed analysis of the performance benefits of step climb is provided in performance Sec.XII.

E. Engine Selection

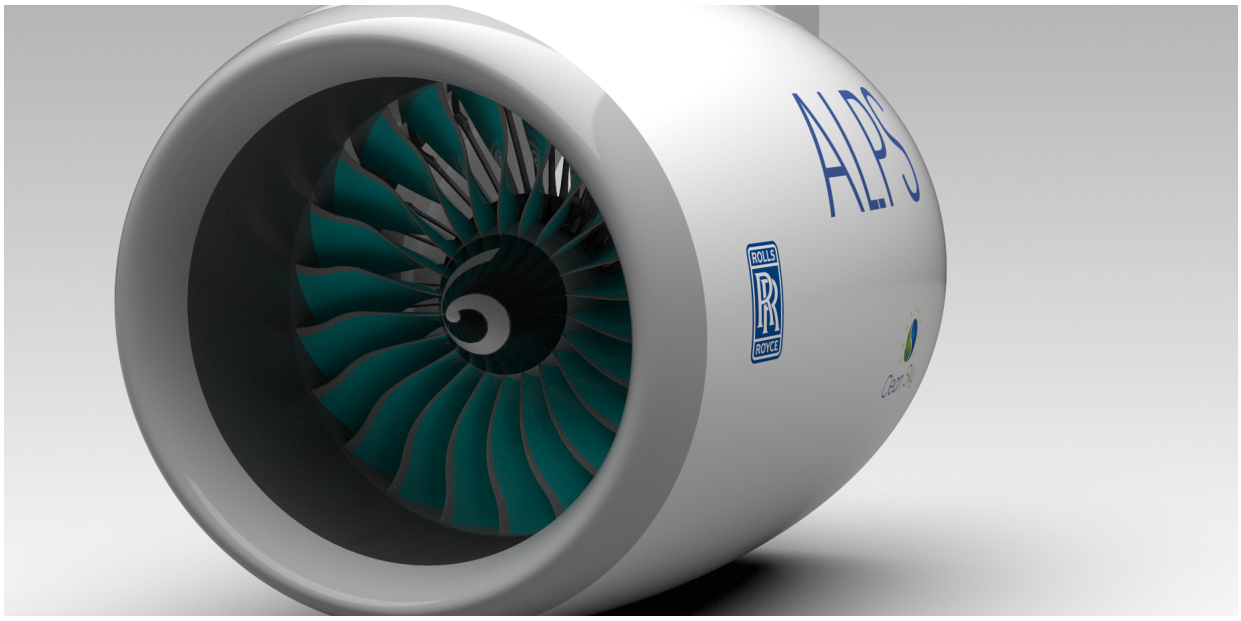

Fig. 16 CAD model of the engine selected

To summarize, an optimal engine should have low SFC, low weight, and at least 62,500 lb of thrust. With these factors in mind, six current generation engine families and one in development engine were found to fulfill all the requirements. Some key parameters for those engines are listed below in Table 11. GE90, GE9X, and Trent XWB are slightly overpowered for this aircraft. However, they are worth mentioning in case more payload is desired, or the need arises to cover high altitude airports. Also, it should be noted that each family of the engine comes with multiple models. Therefore some parameters are shown as a range of values in table. For the next generation engine UltraFan, the parameters are estimated based on the frozen design provided by Rolls-Royce. A CAD model was made according to the parameters and pictures released by Rolls-Royce. Figure 16 is a rendering of the CAD model. The estimations of UltraFan below are based on worst case parameters to provide a margin for JJJP design in case the supplier fails to meet the target.

Table 11 Engine Parameters

Engine Family	Application	Takeoff Thrust (dry) [lbf]	SFC [lbf/lb-hr]	Weight (dry) [lb]
GEnX [19]	787-8/9/10, 747-8	66,500-76,100	0.505	13,552
RR Trent 1000 [20]	787-8/9/10	59,600-81,000	0.495	13,300
RR Trent 7000 [20]	A330 NEO	72,834	0.508	14,209
RR UltraFan [21]	EIS 2025	25,000-100,000 scalable	0.424	12,200 [22]
RR Trent XWB [23]	A350 XWB	84,200-97,000	0.492	16,300
GE90 [24]	777	76,400-115,000	0.52-0.545	16,000
GE9X [24]	777X	93,000-134,300	0.47-0.49	19,000

The next-generation engine surpasses the current generation on almost all parameters, even with the most conservative estimations. The engine is also scalable from 25,000 lb of thrust to 100,000 lb of thrust, meaning that there are much more flexibility in the design process. RR UltraFan is chosen as it provides an unparalleled advantage on both fuel economy and weight.

F. Engine Characteristics

Since the UltraFan is not currently available, the performance characteristics of the engine need to be estimated. Applying Raymer [6] equation of SFC vs. altitude vs. Mach on the known parameters of the UltraFan gives the following characteristics (Fig 17). As altitude increases, specific fuel consumption decreases. And as the speed of the aircraft increases, the SFC increases as less thrust is produced with same fuel flow rate.

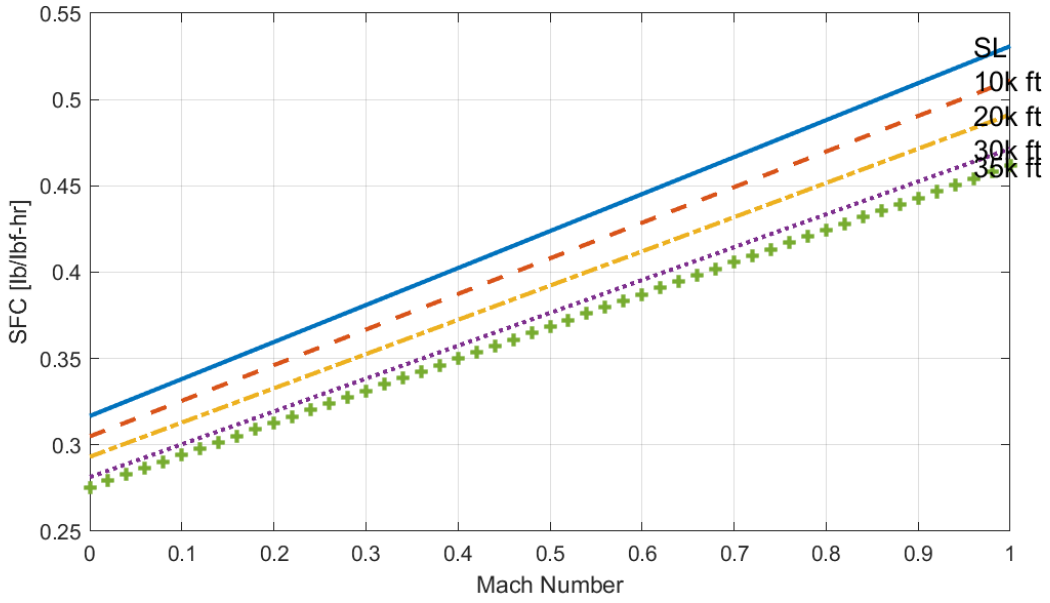

Fig. 17 Raymer SFC estimation

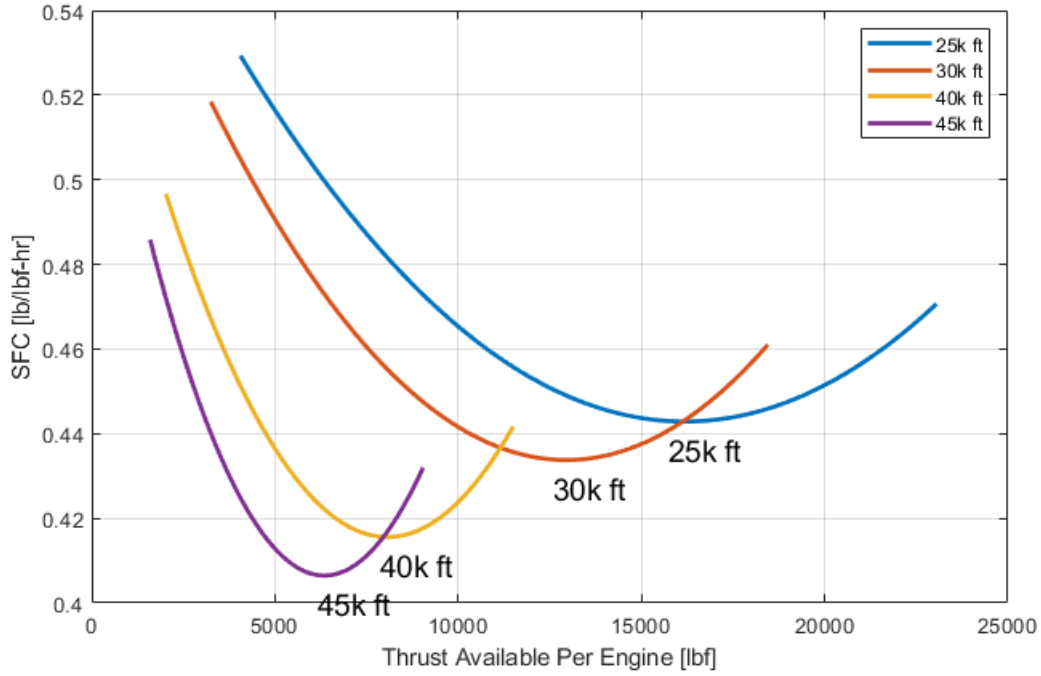

Fig. 18 Thrust Used vs SFC

Apart from mach number and altitude, SFC is also dependent on the throttle level. The engine characteristic model took into account the throttle level too according to the method provided in Artur Bensel's paper [25]. Figure 18 is produced assuming cruise at M=0.8. As illustrated in the plot, thrust available decreases with altitude and the optimal

SFC occurs around 70% throttle.

The thrust available from each engine vs. altitude relation is estimated from the pressure ratio between the cruising altitude and the sea level. The relation is shown in Fig. 19. From the plot, at cruise altitude each engine can produce 15,000 lbf thrust.

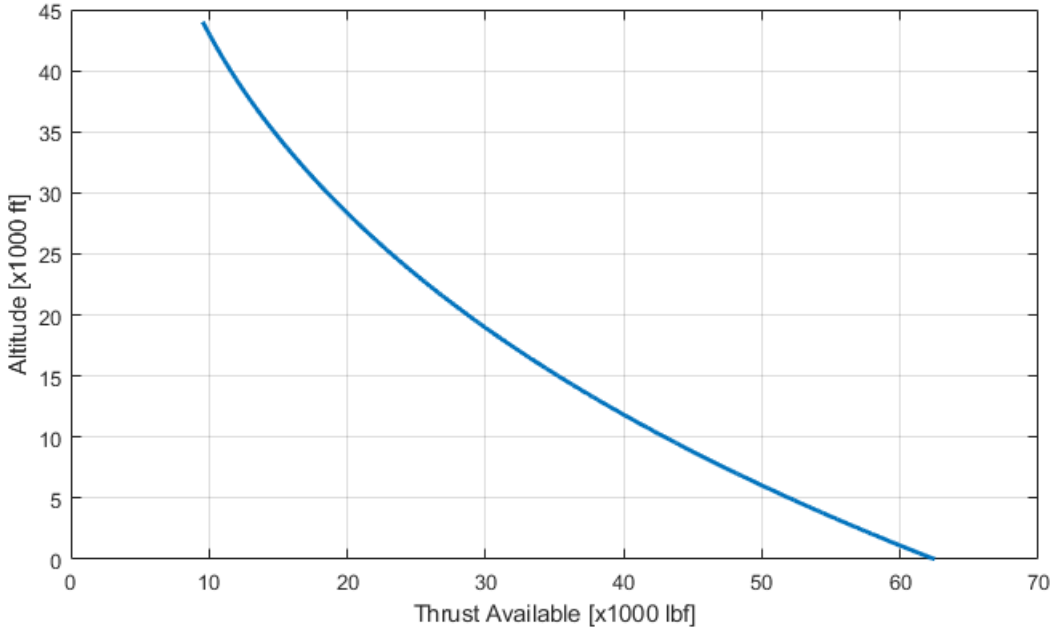

Fig. 19 Thrust Available from Each Engine vs Altitude

G. Inlet, Nacelle, and Exhaust

The inlet is designed to tilt downward 4 degrees to compensate for the cruising angle of attack and increase the inlet capture area at cruise condition. At cruise condition, the inlet capture area is 90.5 ft^2 , and the engine inlet area is 65.5 ft^2 . At optimal cruise condition M=0.78, this area ratio can decelerate the air to M=0.45 and convert 86.8% of the total pressure to static pressure. According to Raymer equations [6], the inlet pressure recovery is estimated to be 99.15%.

Figure 20 shows the cross section of the engine. The nacelle cross-section is designed to be like an airfoil to minimize drag. Located inside the nacelle are accessory gearbox, power management systems, and fuel delivery systems. The nacelle can be opened at the end of the fan cowling to provide reverse thrust upon landing.

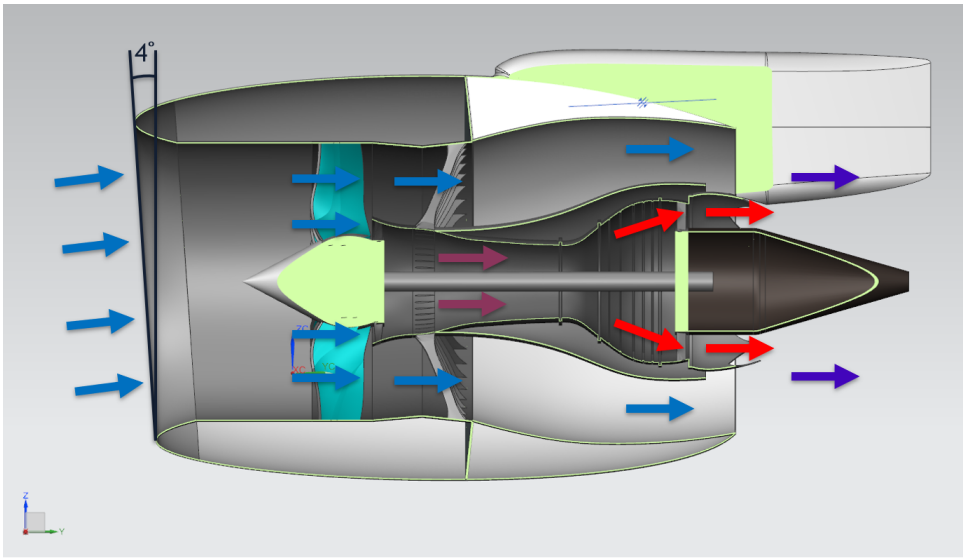

Fig. 20 Inlet, nacelle, and exhaust

The engine has two exhausts in total. One is bypass channel exhaust, and the other is combustion chamber exhaust. Similar to current generation design, the hot core exhaust will be gradually mixed with cold bypass exhaust through a chevron-shaped exhaust to reduce noise (Fig. 21). The routing of the exhaust is shown in the CAD cross-section (Fig 20).

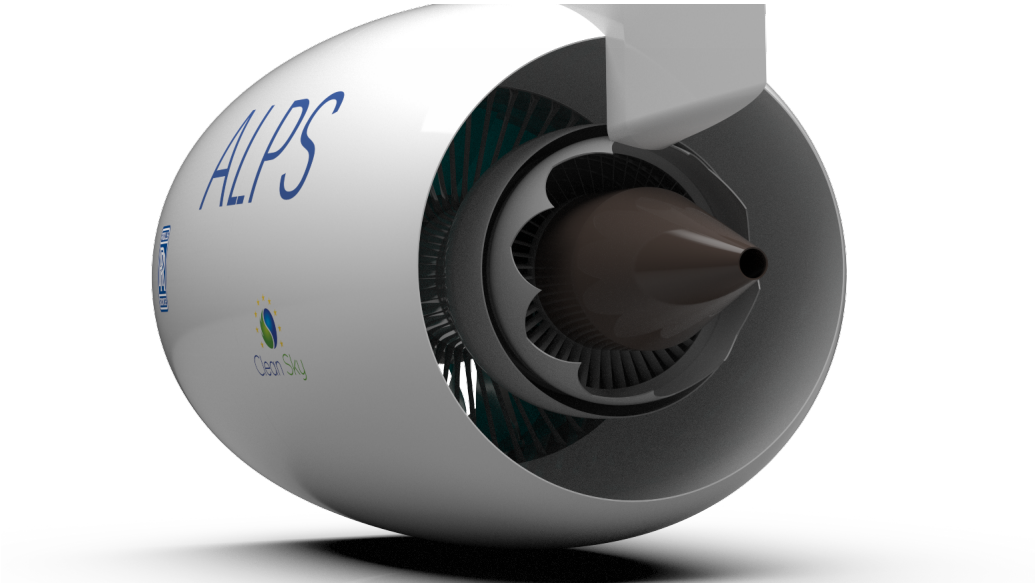

Fig. 21 Chevron Exhaust

Since typical thrust losses due to installation are 4% for low bypass and 8% for high bypass ratio engine ([26]) , the installed thrust loss for UltraFan is estimated to be 10% since this engine is an ultra high bypass ratio engine (15:1). With installed thrust requirement stands at 62,500 lbf, the uninstalled thrust required is estimated to be 69,500 lbf.

H. System Perspectives

1. Engine System

In general, engines are placed below the wing like majority of the commercial aircrafts, for both safety consideration and structural reasons. Refer to Auxiliary Systems section (Sec. XVIII.B) for the details on FADEC setup and system architecture.

2. Fuel System

The detail of the fuel system is further covered in the Auxiliary Systems section (Sec.XVII.C). The total amount of fuel required for JJJP on a 3,500 nmi mission is 83,610 lb, according to the performance calculation (Sec.XII.J). The maximum fuel capacity is therefore set to 110,000 lb.

X. Aerodynamics

A. Airfoil Selection

Airfoil selection was performed using the vortex-lattice software XFLR5. The software is useful as a means to quickly compare characteristics of similar airfoils. However, it does not analyze airfoils in the transonic regime. When cruising in the transonic regime, air flow on top of the airfoil will become supersonic and generate shock waves. This is not desirable for the aircraft because upper-surface shock waves will cause loss of lift and increased drag. At the same time, the shift in center of pressure will change pitching moment. For a swept wing, loss of lift will result in sudden pitch down moment or "Mach tuck". Supercritical airfoils are design to minimize these effects by having a more uniform thickness distribution. They move the camber location to the trailing edge to delay shock wave and turn strong shock waves into weak shock waves [6]. SC-0412, SC-0714, RAE-5215, and DFVLR R-4 were chosen for potential airfoil candidates [27]. They were analyzed at a fixed Reynolds number to get a sense of their performance.

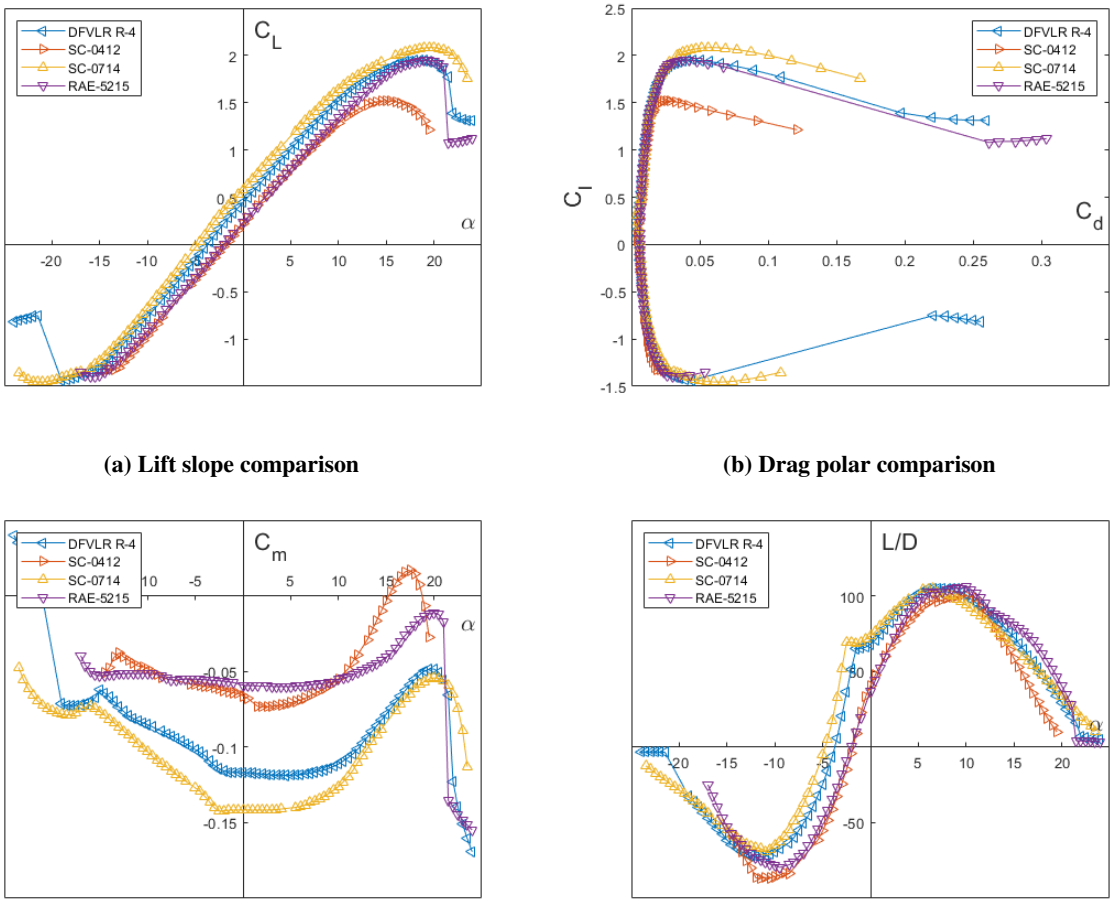

(a) Lift slope comparison

(b) Drag polar comparison

(c) Moment coefficient comparison

(d) Lift to drag ratio comparison

Fig. 22 Comparison of Airfoil Aerodynamic Characteristics at Re = 3 million, Mach=0.0 using XFLR5

Figure 22 shows the aerodynamic performance of two high cambered airfoils (R-4 and SC-0714) and two relatively low cambered airfoils (SC-0412 and RAE-5215). High cambered airfoils offer more lift and L/D compared to low cambered airfoil but suffer from a high moment coefficient, as shown in Fig 22c. For example, the SC-0714 has a $L/D = 66.3$ at $\alpha = 1.25$, but the moment coefficient is 69.86% higher than the SC-0412. This contrast has a direct impact on stability and control (e.g. increasing tail size to counter the pitching moment). As shown in the drag polars in Fig 22b, performance of all four airfoils were similar in the non-stall region.

OpenVSP was used to do high speed trade studies for airfoil selection. Since OpenVSP cannot analyze 2D airfoils, a 3D wing will be sufficient for comparison.

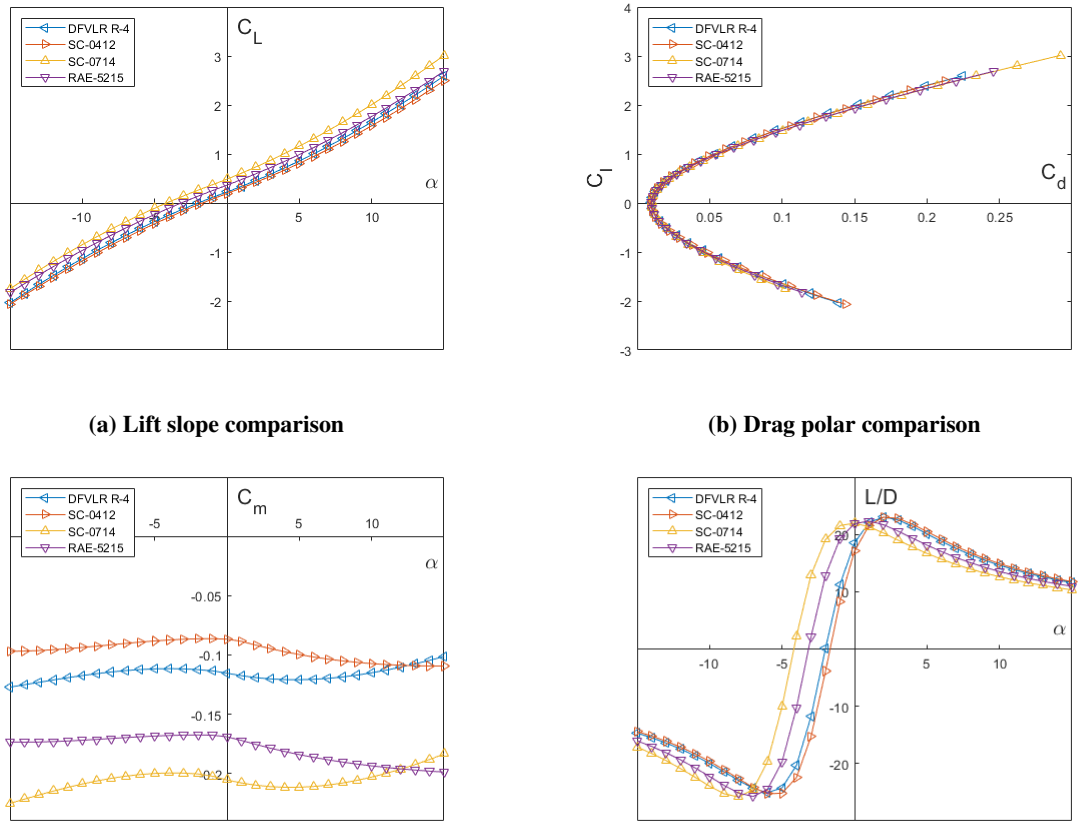

(a) Lift slope comparison

(b) Drag polar comparison

(c) Moment coefficient comparison

(d) Lift to drag ratio comparison

Fig. 23 Comparison of Airfoil Aerodynamic Characteristics at Mach=0.78 using OpenVSP

Figure 23 shows aerodynamics characteristics of the 3D wing using OpenVSP. Despite the general trend of the aerodynamic performance curves matching the results from XFLR5, the lift slope is higher compared to XFLR5. The Moment coefficient diagram and lift-to-drag ratios are consistent with XFLR5, where the low camber airfoils have lower pitching moments and the lift-to-drag curves shift to the right. One of the limitation of OpenVSP however is the inability to predict stall.

Because of this analysis, the selection was narrowed down to the SC-0412 and RAE-5215. Historical trends provided by Raymer in Chapter 4 of *Aircraft Design : A Conceptual Approach* suggest that a thickness to chord ratio (t/c) of around 13% is appropriate for transonic aircraft [6], which makes the SC-0412 a more favourable pick than the RAE-5215. Although a thinner airfoil will minimize drag and especially wave drag, it hinders other systems such as fuel tank size, structural integrity, and high-lift system. Although the SC-0412 is lacking in terms of aerodynamic efficiency, it was a well rounded airfoil. Thus it was chosen to be the airfoil that best met the necessary performance requirements of the JJJP. The SC-0412 geometry is shown in Fig. 24. For tail airfoil selection, see section XII.B.

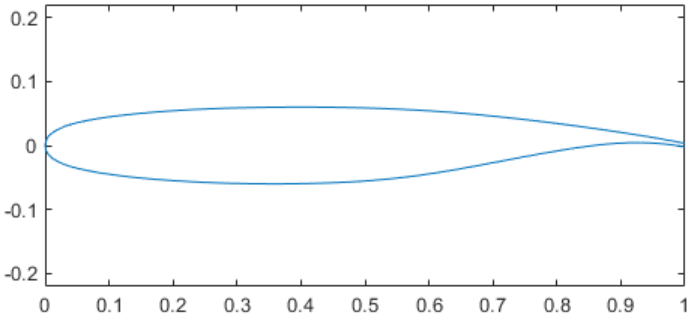

Fig. 24 NASA SC(2)-0412 Airfoil, max thickness of 0.12% at 37% chord, max camber of 0.13% at 83% chord

B. Wing Design

Wing parameters were determined by multiple trade studies in the initial sizing phase. Those studies examined parameters such as wing area, aspect ratio, and taper. Other parameters were chosen based on historical data. Wing twist is a solution for improved stall performance, so the outboard section of the wing doesn't stall first. For geometric twist, a typical -3 deg of twist will provide adequate stall characteristics suggested by Raymer [6]. For wing dihedral, a low wing transonic aircraft will typically have three to seven degrees of dihedral [6]. The JJJP dihedral was determined to be 6 deg based on roll stability calculations and engine ground clearance. Wing sweep reduced wave drag due to reduction of chordwise flow and shock wave at an oblique angle on the wing.

Since the aircraft is designed for short haul high capacity missions, the cruise speed impact on travel time has less of an effect than longer range missions. Initial sizing trade studies concluded that reducing the wing sweep from the seed aircraft's 31 degrees to 25 degrees would be a more optimal due to the lower cruise speed of Mach 0.78 [28]. A lower wing sweep will also lower the weight of the wing. Wing sweep reduces the M_{dd} by a factor of inverse square root of cosine of sweep angle according to Equation 4.15 in Roskam [29]. The Boeing 777-200 cruises at Mach 0.84 [27] with a 31 degree sweep. A quick calculation shows, using Equation 4.15 with the same wing, a reduction of six degrees of sweep will lower M_{dd} to 0.817. Reduction of $\Delta M_{dd} = 0.025$ is an acceptable compromise for the benefit of less structural weight. Wing parameters are listed in Table 12.

A further investigation on this trade study was conducted using Delta method. Wing sweep angle for commercial aircraft are typically around 31 deg. However, sweeping beyound 25 deg will see diminishing return due to its minimum wave drag reduction. Using Delta method, 2 count of wave drag reduction was predicted going from 25 deg to 31 deg wing sweep.

Table 12 Wing Parameters

Parameter	Value
Wingspan	183.7 ft
Wing Area	3,880 ft^2
$\frac{S_{wet}}{S_{ref}}$	6.2
$\frac{C}{4}$ Sweep	25 deg
Taper	.15
Twist	0 deg to -3 deg
Dihedral	6 deg
Wing Incidence Angle	3 deg

For steady level flight at Mach 0.78 at 38,000 feet, a lift coefficient of 0.44 was calculated via the initial sizing code. OpenVSPAERO, a fast vortex lattice solver, was used to do aerodynamic analysis on the wing for cruise condition. The lift curve was determined by scaling the OpenVSP result at Mach 0 with Raymer's prediction of transonic lift slope. To obtain the scaling factor, simply use the typical swept wing high aspect ratio curve in Raymer Fig. 12.6 [6], and take the ratio of lift slope at Mach 0.78 to lift slope at Mach 0. With the wing cruise lift curve, incidence angle was determined to be 3 deg because the wing will satisfy the lift requirement at that angle of attack. C_L and L/D were plotted against α in Fig 25a and Fig 25c respectively, and the mission points are indicated with black star. $C_L = 0.44$ at $\alpha = 0°$ in Fig 25a satisfied the cruise lift requirement. Additionally, $L/D = 15.714$ at $\alpha = 0°$ is within a reasonable range when compared to aircraft at this size. For example, the Boeing 747-400 has cruise L/D of 15.5 [30].

C. Aircraft Aerodynamic Characteristics

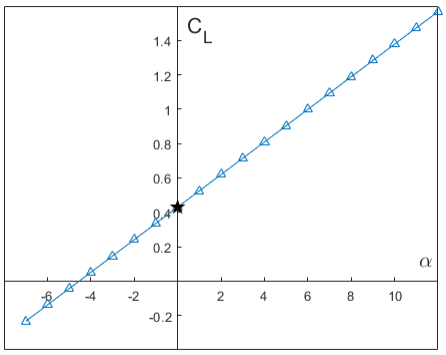

(a) Aircraft cruise Lift Curve Slope Graph

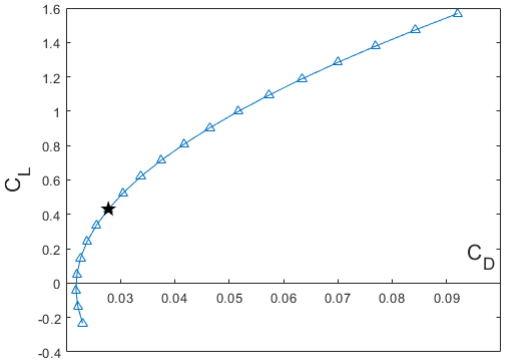

(b) Aircraft cruise drag polar

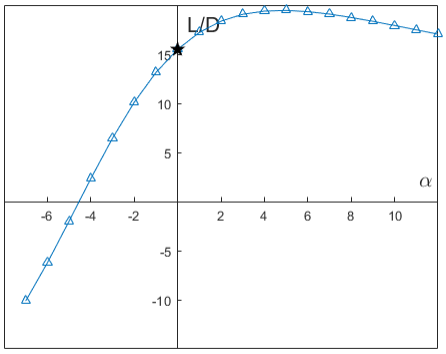

(c) Aircraft cruise L/D curve

Fig. 25 Aircraft cruise aerodynamic characteristics

For aircraft aerodynamics characteristics at cruise, three diagrams that showcases lift curve, drag polar, and L/D curve are shown in Fig. 25. Cruise lift curve and L/D cruise were determined by shifting the wing's polar to the left by 3 deg.

For takeoff/landing analysis, XFLR5 was used as a mean to construct aircraft polars. To use XFLR5, the airfoil needs to be analyzed at a Reynold's number from 8 million to 55 million (From tip chord to root chord) at Mach 0.202 for landing and Mach 0.23 for takeoff. Both analyses used an inviscid Vortex lattice method for flapped wings. Since XFLR5 can only model plain flaps and slats, highlift device modeled for the JJJP closely resemble those of the Boeing 777 [31]. As shown in Fig. 27, landing flaps were set to 35 deg for leading edge flap and 50 deg for plain flap. 24 deg and 34 deg was set respectively for takeoff. Key mission points are marked by the black star.

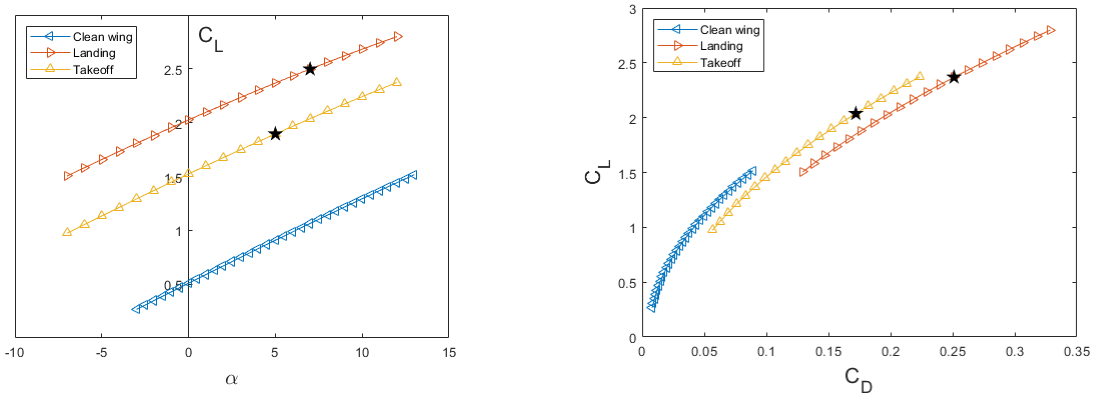

(a) Aircraft takeoff/landing Lift Curve Slope Graph

(b) Aircraft takeoff/landing drag polar

Fig. 26 Aircraft takeoff/landing aerodynamic characteristics

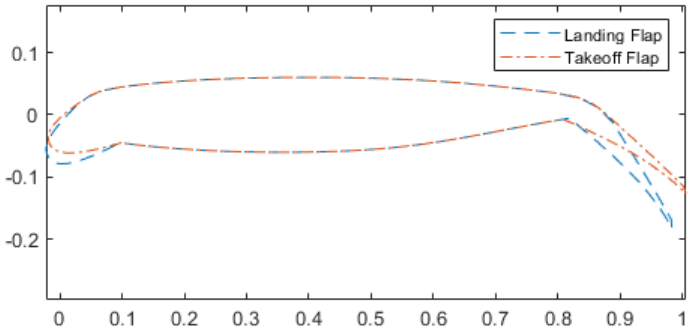

Fig. 27 XFLR5 flap model

D. High Lift Device

The wing was sized by maximum lift coefficient as determined by performance. C_{Lmax} based upon the design requirement is around 2.49, so the goal is to size the high lift devices to meet that. Leading edge slats and double slotted Fowler flaps were used to achieve landing requirement. This was done mainly because double slotted Fowler flaps gave two advantages. Extending the flap increase projected area to shift the lift curve to the left. On the other hand, slots increase C_{Lmax} by allowing high energy airflow from the bottom surface to the top. However, the wing will stall much quicker. To counter that, leading edge slat is used to delay the stall, which shifts the lift slope to the right. At the same time, increase C_{Lmax} due to the increase in projected area. Using the combination of slat and double slotted flap will be able to produce more lift maintaining the same stall angle of attack [6].

Sizing of the flap is done by using the similar configurations and dimensions of the high-lift system on the Boeing 777 and the SCW-2A airfoil [31][32]. It was then verified in XFLR5. However, XFLR5 model is limited in that it can only model plain flaps. This can be adjusted for as XFLR5's aerodynamics model uses the Vortex Lattice method. The

Vortex Lattice method does not account for flow separation, which can be used to simulate flow around slats and slotted flaps. This is because slats and slotted flaps induce high energy air to flow from the bottom surface to the top, and thus reduce adverse flow or flow separation. High-lift device dimensions were shown in Table 13.

Table 13 High-lift device dimensions

Dimension	value
Flap span (from wing/fuselage interface)	99.2 ft
Slat span (from wing/fuselage interface)	129.6 ft
Flapped area (flap)	2,454 ft^2
Flapped area (slat)	2,895 ft^2
Flap extention ratio (cf/c)	1.11
Slat extention ratio (cf/c)	1.06
Hinge angle	21.8 deg

The flap layout of the airfoil is going to be similar to SCW-2A [32]. This is possible as in comparison to the SCW-2A, the SC-0412 has the same thickness to chord ratio at the same location and a minor difference in camber. According to flap layout diagram in Fig. 29, the slat uses 14% of the chord, the vane uses 18%, and the flap uses 12%. The cove should be properly sized to include volume for the flap extension hydraulics and actuators.

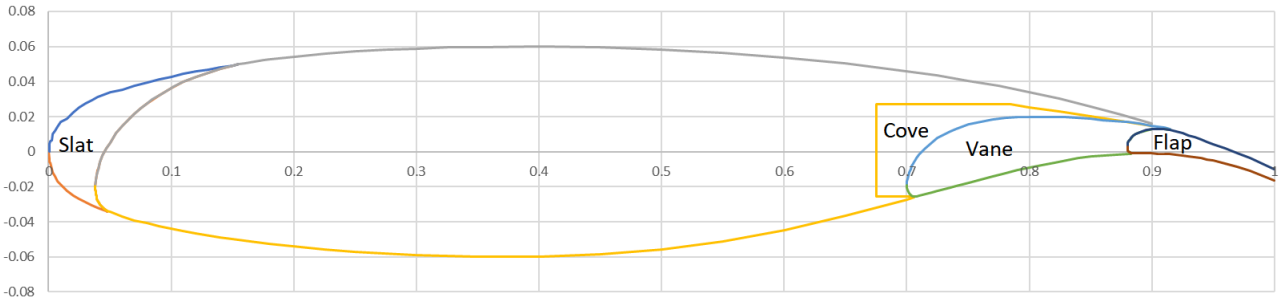

Fig. 28 SCW-2A flap layout

E. CAD Drawings

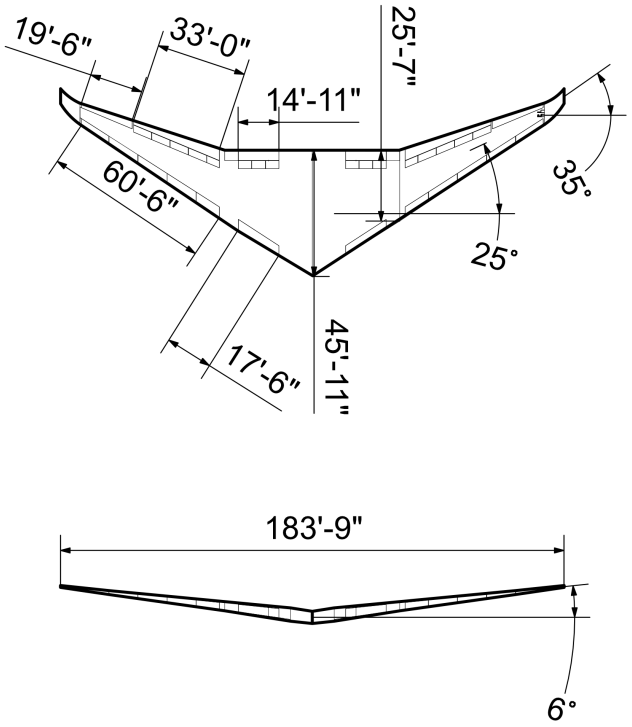

Fig. 29 Top and front drawing with major wing dimensions, along with flap layouts

F. Drag Buildup

Drag buildup is important because it impacts performance in cruise. Buildup was mainly done using Raymer's component buildup method. It yields similar cruise drag values when compared to Raymer's equivalent skin friction method, which verifies that cruise drag was accurately approximated. Wave drag was calculated using the Delta method [33], with an estimated design lift coefficient of 0.50. Next, the design mach number was estimated using inputs of the 2D drag divergence Mach number, aspect ratio correction, and wing sweep correction. The design Mach number is 0.83, which agrees with an earlier assumption. If the aircraft is cruising at M_{dd} or design Mach number, the aircraft will experience 20 counts of drag. 10 counts of wave drag was estimated at Mach 0.78. Trim drag was determined using Nicolai's assumption of 10% of induced drag [34].

Takeoff and landing drag buildup was estimated using a combination of Raymer for component drag and Roskam for high-lift drag [6] [29]. Flap drag consisted of flap pressure drag, flap induced drag increment, and interference drag. Flap induced drag increment and pressure drag contribute to the majority of the drag. The large induced drag increment was due to flaps disturb the lift distribution, and thus it is no long being elliptical. Pressure drag on the other hand was cause by large flap deflection angle. Drag buildup for landing and takeoff is shown in Fig. 16. For $\frac{S_{wet}}{S_{ref}}$ calculation, see section X.B Table 12.

Table 14 Cruise Raymer component drag buildup with Delta wave drag prediction

Component	Swet (ft^2)	FF	Q	CD0	Contribution (%)
Fuselage	12,270	1.0733	1	0.0055	32.8
Wing	7,954	1.5219	1	0.0063	37.6
Vertical Tail	895	1.5788	1.08	9.02E-04	5.4
Horizontal Tail	1,741	1.5788	1.03	0.0017	10.1
Pylons	263	1.2153	1.3	2.51E-04	1.5
Engine Nacelle	2,376	1.1865	1.3	0.0021	12.5

Table 15 Cruise-Drag Buildup comparison

Drag type	Raymer equivalent skin friction	Raymer component buildup
C_{Do}	0.0161	0.0163
C_{Dexcr}	0.00081	0.00082
C_{Dtrim}	0.00090	0.00090
C_{Di}	0.00090	0.00895
C_{Dwave}	0.0010	0.0010
C_{Dtot}	0.0278	0.0280

Table 16 Takeoff and landing drag buildup

Drag type	Landing drag	Takeoff drag
C_{Do}	0.0171	0.0170
C_{Dexcr}	0.00086	0.00085
C_{Dtrim}	0.00906	0.00876
C_{Di}	0.0885	0.0885
C_{Dflap}	0.1438	0.0803
C_{Dtot}	0.262	0.195

G. Trade study

For the wing sweep angle trade study, see Subsection X.B. For the airfoil selection trade study, see Subsection X.A.

H. Key Aircraft Parameters

Table 17 Key aircraft information

Parameter	cruise	landing	takeoff
Angle of attack	0 deg	7 deg	5 deg
C_L	0.44	2.49	1.89
C_{Dtot}	0.0280	0.262	0.195

XI. Performance

A. Performance Requirements

According to the RFP, the JJJP must be able to fly 3,500 nmi missions carrying 410 people on board [1]. This is equivalent to a normal payload of 94,300 lb. It should also have a balanced field length of less than 9,000 ft and a landing field length at the end of mission less than 9,000 ft when operating at ISA + 15°C. The approach speed at the end of 3,500 nmi mission should also be less than 145 KCAS.

Additionally, the RFP states that an appropriate mission profile would be takeoff, 3,500 nmi cruise, descent, loiter 5 minutes, approach, divert climb, divert cruise 200 nmi, descent, loiter 30 minutes, approach, and then land, as shown in Fig. 3.

It was decided by the group that a higher fidelity estimation of the performance, through out the stages of flight, should be simulated. Specifically, a simulation was developed that took in the design parameters such as weight, thrust, TSFC, maximum Cl, a drag model, etc. Within the simulator, the equations of motion were implemented to predict the state of the aircraft. Then the simulation progressed in a time step fashion, simulating each stage of the mission, including takeoff, climb, cruise, descent, loiter, approach, and landing. Additional capabilities were developed within the performance simulator. For instance, the simulator can solve for the optimal amount of fuel to carry that would fulfill the reserve requirement. It is also capable of performing a trade study to find the optimal operational schemes. It can also be used to generate a payload range diagram, pragmatically.

B. Takeoff & Landing Performance

To accurately account for the requirement stated in the RFP, all the takeoff and landing performance simulations were simulated under a ISA+15°C condition. For takeoff distance, a 35 ft obstacle was assumed. In order to find the V1

speed, a range of speeds at which one engine fails was tested. Provided this data, the simulator then calculates the total distance needed to continue with the take off or stop. From the simulated result, the V1 is found to be 165 KCAS at maximum takeoff weight (MTOW), and balanced field length is found to be 7,850 ft, which easily fulfills the 9,000 ft requirement set in the RFP.

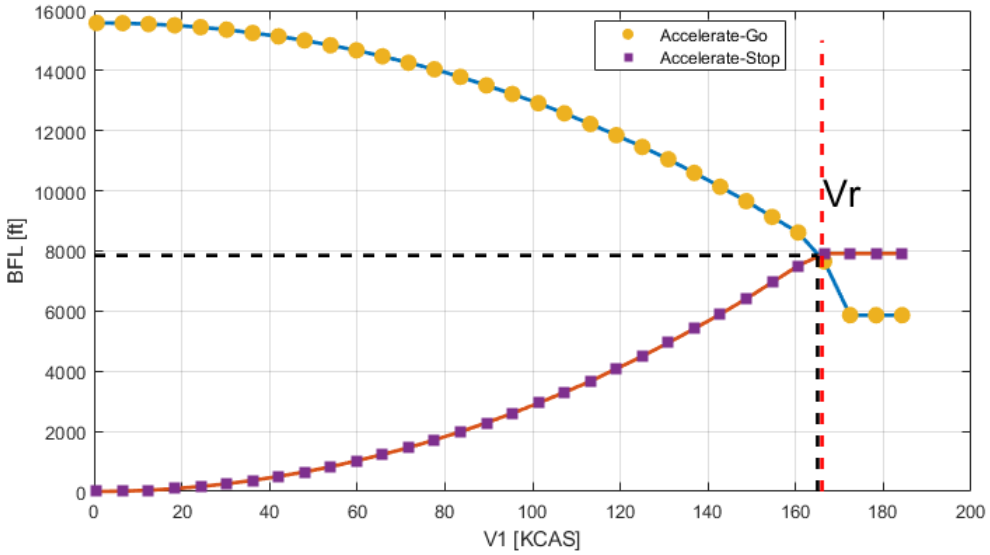

Fig. 30 BFL analysis

The comparison plot of the takeoff flight path is shown below in Fig 31. The plot shows a takeoff trajectory for AEO and OEI conditions.

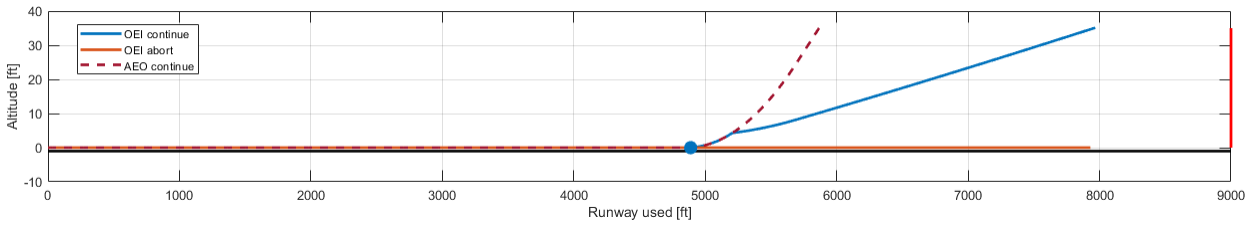

Fig. 31 Takeoff path

Similarly, the landing performance can be determined with the time integration simulator. At ISA+15°C dry condition, the landing distance of maximum landing weight (MLW) was 4,420 ft. Note that in all conditions, a thrust reverser was not used.

Alternate conditions considered were wet and icy concrete/asphalt. Dirt and grass were not considered as the team decided an aircraft of this size will not be used on grass and dirt strips. The BFL and LFL on all conditions were summarized in Table 19:

Table 18 BFL / LFL at Sea Level

Condition	BFL@MTOW	LFL@MLW	LFL@End of 3,500 nmi mission
Dry concrete/asphalt	7,850 ft	4,420 ft	3,980 ft
Wet concrete/asphalt	8,910 ft	5,870 ft	5,250 ft
Icy concrete/asphalt	11,300 ft	13,500 ft	12,000 ft

From the table above, JJJP can achieve the 9,000 ft requirement under both dry and wet conditions without the help of thrust reversers. For icy conditions, further analysis was done with thrust reverser and the resulting landing field length was found to be 6,960 ft. Therefore it is suggested that, when landing the JJJP on icy runways, thrust reverser should be used for safety considerations.

C. Other Performance Parameters

The maximum rate of climb at MTOW and takeoff condition is 3,500 ft/min. However, in normal operating conditions, a less aggressive initial rate of climb of around 1,700 ft/min can be used. The JJJP is perfectly capable of achieving this initial rate of climb.

The service ceiling of the aircraft is dependent on the weight and speed that the aircraft is flying. The analysis assumed a design cruise speed of mach 0.78. Therefore it was possible to calculate the heavy-weight (MTOW) ceiling, medium-weight (50% fuel, normal payload) ceiling and light-weight (20% fuel, no payload) ceiling. Notice that the ceiling calculated here was only the mechanical limit of the aircraft, purely dependent on the thrust and lift available. Often time, the other systems would exert a lower limit on cruising altitude.

Table 19 Service Ceiling

Condition	Fuel Carried	Payload Carried	Service Ceiling
Heavy-weight	100%	94,300 lb	36,700 ft
Medium-weight	50%	94,300 lb	39,200 ft
Light-weight	20%	0 lb	47,200 ft

D. Drag for All Flight Segments

Examples of drag and drag coefficients for each flight segment are summarized in Table 20. At takeoff and landing, drag are very low since the wing is not producing much lift at low speed. While for majority of the stages, JJJP is flying with a similar range of drag values just above 20,000 lbf. The two exceptions are climb and approach. For climb, JJJP is

using more lift and consequently generating more induced drag. For approach, as flaps and slats are extended, more drag are created to both descent and slow the aircraft down.

Table 20 Segment Drag Summary

Segment	C_D	Drag
Takeoff	0.03060	4,500 lbf
Climb	0.02756	26,880 lbf
Cruise	0.03036	24,650 lbf
Descent	0.03389	21,390 lbf
Loiter	0.03686	20,810 lbf
Approach	0.12540	29,760 lbf
Landing	0.01959	3,710 lbf

E. Aircraft Performance Coefficients

Using the same drag model and aircraft parameters as the simulation, it was possible to calculate various performance coefficients at different cruising speeds. Using automated tools, the following diagram was plotted at MTOW and cruising altitude FL350 (Fig. 32). The coefficients are recorded in the Table 21.

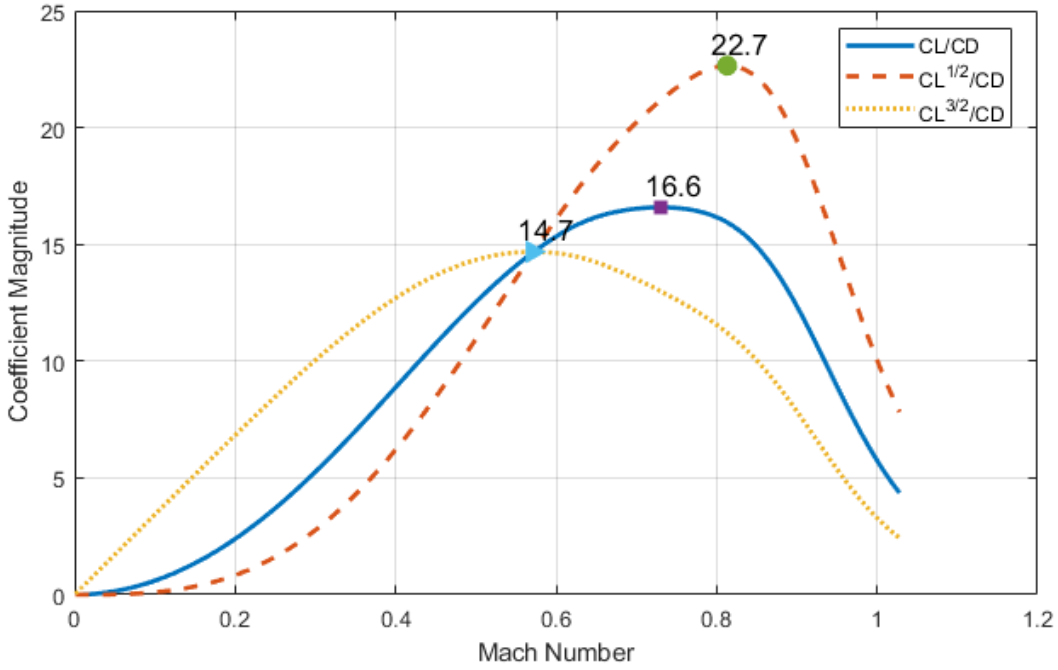

Fig. 32 Performance coefficients

The three coefficients each represented the performance of the aircraft in different scenarios. Specifically, $\frac{C_L}{C_D}$ represented the endurance performance of the aircraft. At $\left(\frac{C_L}{C_D}\right)_{max}$ the drag was at minimum and therefore the thrust required is at minimum. The fuel consumption is minimized and the aircraft could stay airborne the longest. From the plot, the best endurance occurred at Mach 0.73. The $\frac{C_L^{\frac{1}{2}}}{C_D}$ represented the range performance. At $\left(\frac{C_L^{\frac{3}{2}}}{C_D}\right)_{max}$ the aircraft could achieve its maximum range. From the plot, maximum range occurred at Mach 0.81. The third coefficient $\frac{C_L^{\frac{3}{2}}}{C_D}$ represented the loiter performance. The optimal loiter speed was Mach 0.6 according to the location of $\left(\frac{C_L^{\frac{3}{2}}}{C_D}\right)_{max}$.

Table 21 Performance Coefficients

Coefficient	Value	Mach Number
$\left(\frac{C_L}{C_D}\right)_{max}$	16.58	0.730
$\left(\frac{C_L^{\frac{1}{2}}}{C_D}\right)_{max}$	22.65	0.813
$\left(\frac{C_L^{\frac{3}{2}}}{C_D}\right)_{max}$	14.68	0.571

F. Payload-Range & Range Mach Diagram

The JJJP had a maximum payload cap higher than the requirements set in RFP[1]; this brought multiple advantages when conducting short haul flights. Specifically the maximum payload of the aircraft was 150,000 lb, meaning it could carry 50,000 lb of revenue payload on top of 400 passengers. It had plenty of capacity to either carry more people or fit more than a dozen LD3 containers.

A plot of payload range diagram was provided below (Fig. 33). Each blue solid line represented the payload-range performance at specific takeoff gross weight, while the outer most line represented the performance at MTOW. From the plot, the JJJP can carry 103,550 lb of payload for 3500 nmi mission, 9,250 lb more than required. Otherwise, it can go on mission up to 1455 nmi with maximum payload of 150,000 lbs. From the diagram, maximum range of the ferry mission was 4800 nmi.

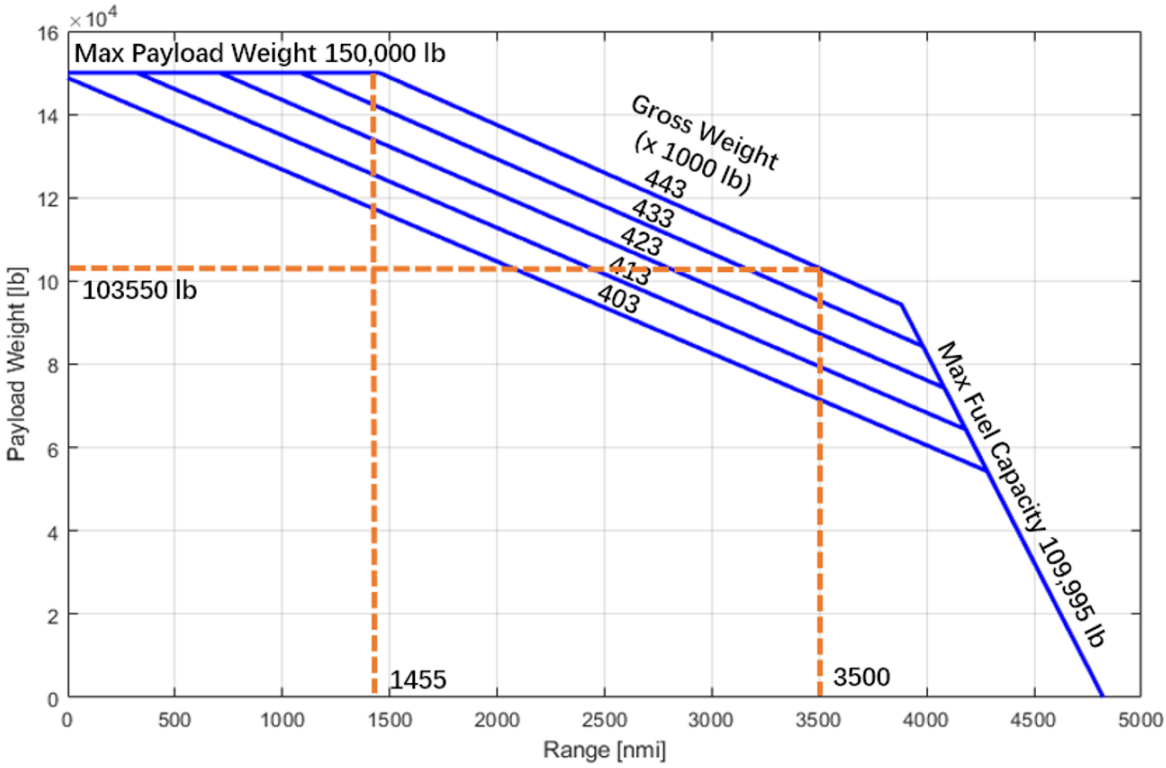

Fig. 33 Payload-range diagram

G. Flight Envelope Diagram

The flight envelope diagram at MTOW was shown below (Fig. 34). The absolute ceiling (heavy-weight) was 36,800 ft . The diagram considered the effect of the wave drag using the delta method [33]. Notice at low altitude, the structural strength determined the maximum speed. The maximum equivalent airspeed of JJJP was 321 knots, which was shown by the purple dashed line. The maximum speed at sea level was roughly Mach 0.49.

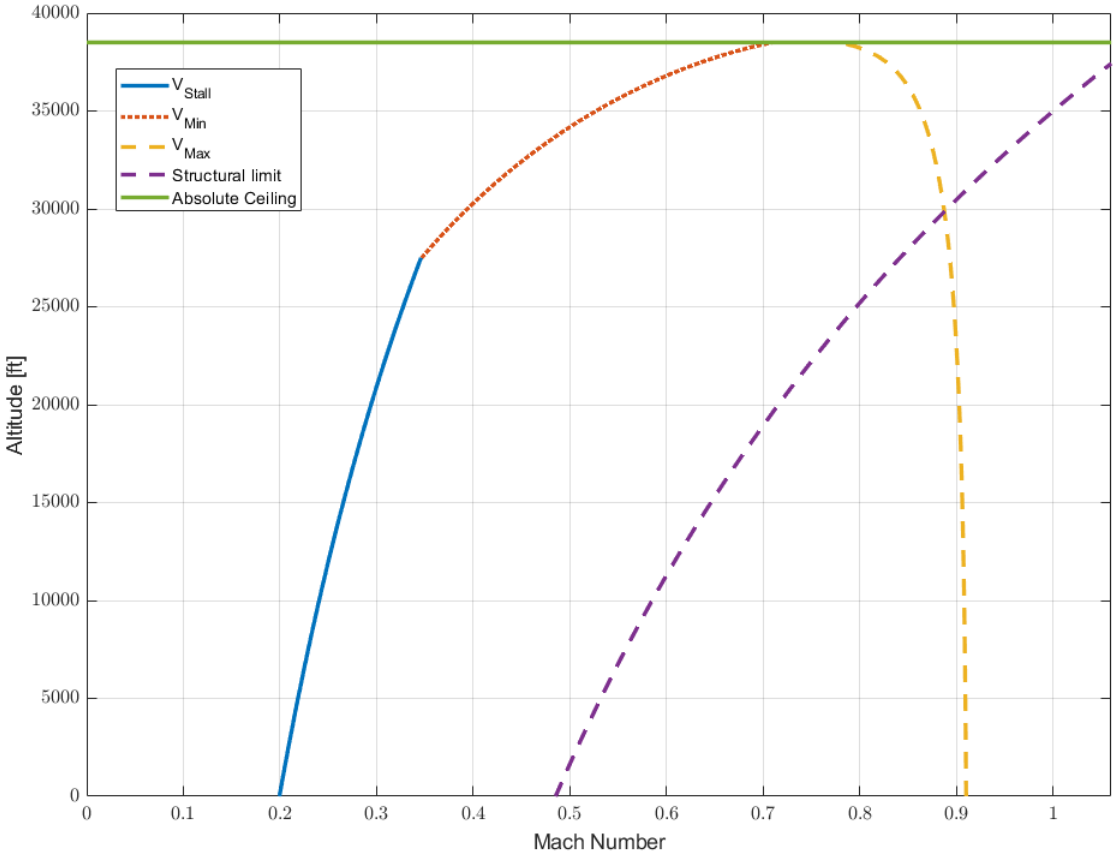

Fig. 34 Flight envelope @ MTOW

H. Specific Excess Power Diagram

To study the climb performance of the aircraft, a specific excess power contour was plotted (Fig. 35). This plot showed the power available to climb at certain speeds and altitudes. For example, at takeoff (Mach 0.25, altitude 0 ft), the diagram suggested specific excess power was roughly 60 ft/s, which was equal to the 3,600 fpm maximum climb rate. This agreed with our takeoff analysis that JJJP had a maximum initial climb rate of 3,500 fpm.

The red line denoted the maximum specific excess power at certain altitudes, which was ideally the best rate of climb line. However in reality, flight envelope determined that the aircraft actually can not reach the optimal line when flying at low altitude. Since the structural limit restricted the maximum speed JJJP can achieve at those altitudes.

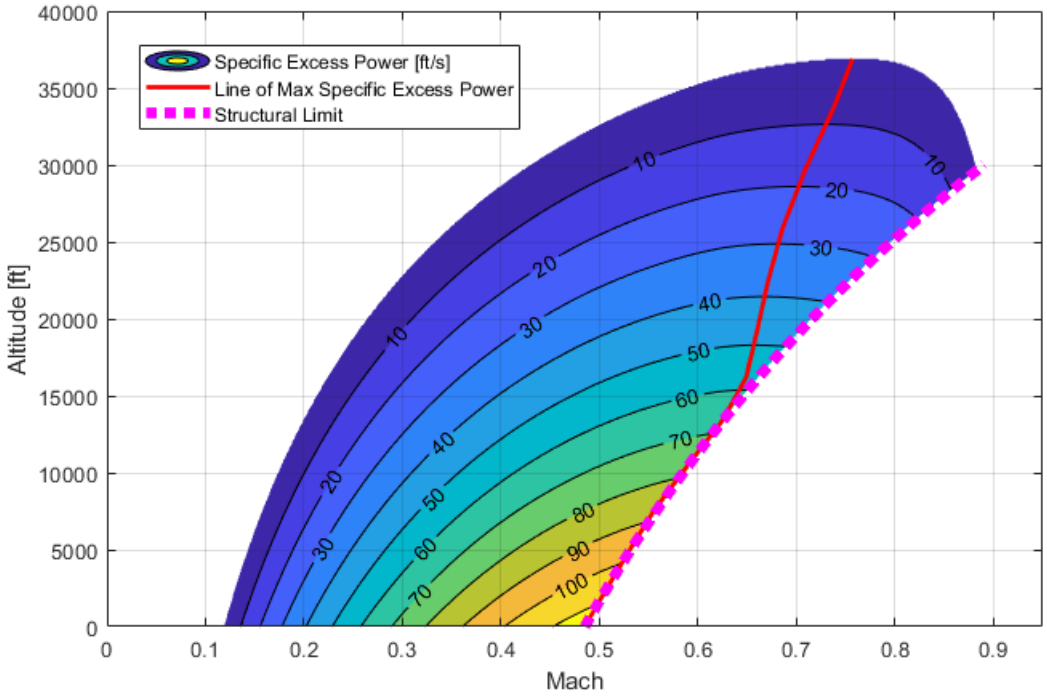

Fig. 35 Specific excess power diagram

I. Trade Studies

1. Cruise condition trade study

The two most important factors in operation was the cruise speed and altitude, both of which determined the fuel consumption in a significant way. If they were chosen poorly, the aircraft could be burning much more fuel than optimal or even unable to reach the destination. It was possible to predict the fuel consumption performance with high fidelity simulation available. Looping over different combinations of cruise speed and altitude, the contour map (Fig. 36) was plotted to conduct the trade study. The contour in the plot showed the amount of fuel in pounds burnt in flying the 3,500 nmi mission, not counting the reserve, contingency or diverting fuel. The simulation accounted for the transonic wave drag using the delta method [33], and accounted for the SFC change with respect to altitude, Mach number and throttle level using the method provided in Raymer [6] and Artur's paper ([25]).

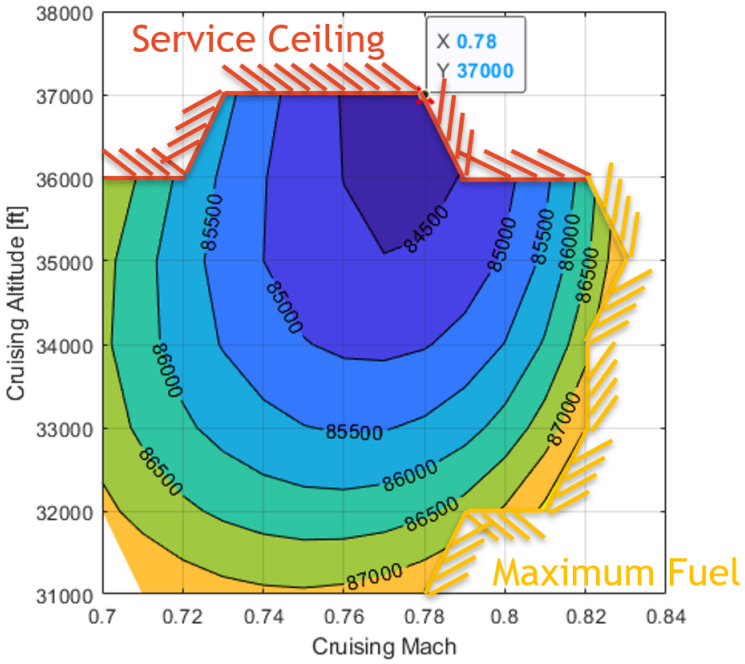

Fig. 36 Cruising mach & altitude trade

The white regions on the contour plot were configurations that won't reach the destination. Specifically, the red limit on the top was set by the initial service ceiling of the JJJP, while the yellow limit on the right was set by the amount of fuel carried to conduct the mission. In this case, the aircraft takes off with 90% full tank.

The optimal cruising Mach number and altitude were found to be M0.78 @ FL370, which was very close to the designed cruise of M0.8 @ FL350. Also, notice that any speed too fast or too slow would cause the aircraft to burn more fuel. This was expected since flying too slow would make the trip time unnecessarily long, while cruising at higher speed would add wave drag. From the diagram, there was a trend that the higher the cruising altitude was, the lower the fuel consumption. However, at MTOW, the aircraft reached the service ceiling at 37,000 ft, making it hard to climb to a higher altitude. Step climb was a potential solution to this dilemma without requiring extra thrust or weight reduction.

2. Step climb trade study

As discussed in the previous trade study, it was obvious that the aircraft could achieve higher fuel efficiency at higher altitude. It was necessary to cruise climb at a later stage of flight in order to maintain a high L/D. Therefore, a simulated flight with cruise climb was plotted in Fig. 37 to compare the fuel consumption. The JJJP would try to climb to a higher flight level (+1,000 ft) when the service ceiling allowed. The blue line in the plot showed the altitude of the aircraft with respect to time. Four cruise climbs were conducted throughout the flight to maintain a high L/D. Over the 3,500 nmi mission, step climb can save over 550 lb of fuel per flight.

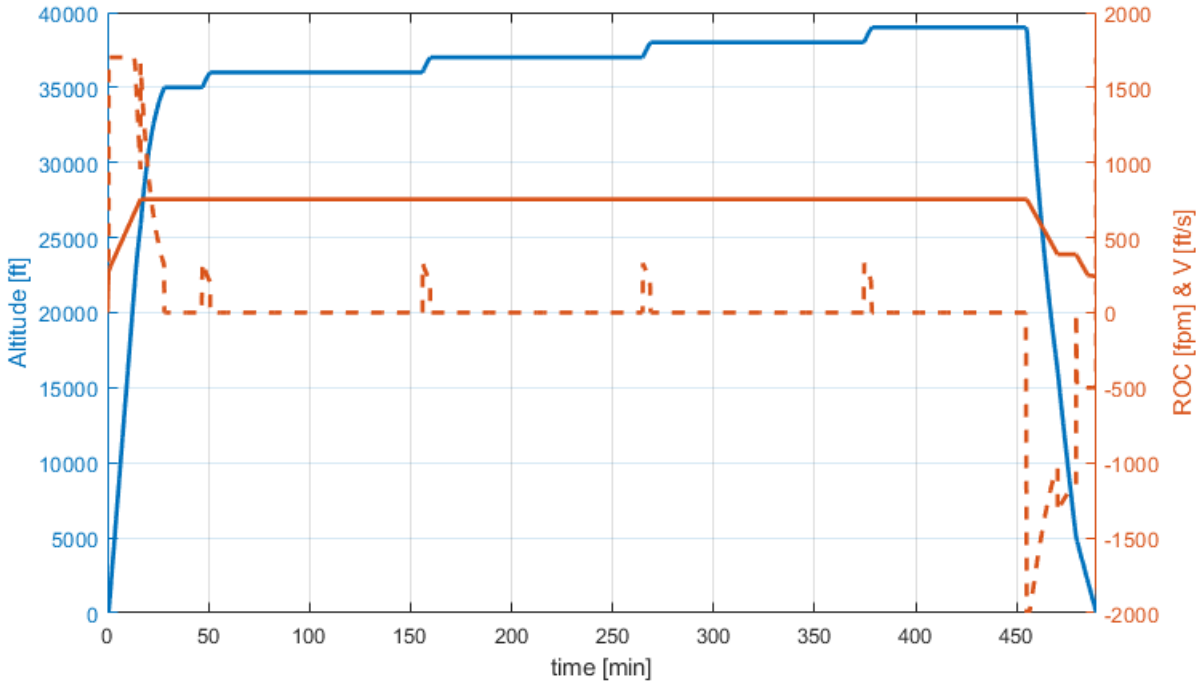

Fig. 37 Simulated flight with step climb

J. Fuel Requirement

For the 3,500 nmi mission, the aircraft did not need to carry full fuel capacity. Therefore, to obtain an optimal amount of fuel to carry, a script was used to solve iteratively an amount that fulfilled the regulation in 14 CFR § 121.639/645 and RFP, while also minimized the fuel burn. With the number obtained from trade study (M0.78 and FL370), the optimal amount of fuel carried was 98,900 lb, in which 83,610 lb was burnt to fly the 3,500 nmi mission. Upon the landing of the 3,500 nmi mission, there would be 15,290 lb of reserve fuel left in the tank. With step climb, the total fuel carried was decreased to 98,400 lb, in which 86,060 lb was burnt and 15,340 lb remained upon landing.

The amount of fuel remaining during the 3,500 nmi mission was shown in Fig. 38. It was assumed that startup and taxi burned 3,000 lb of fuel. Note that the takeoff and landing stage were so short and burned so little fuel that they were hard to tell on the plot. Specifically, takeoff burned 468 lb and landing burned 25 lb of fuel (since for landing the engine was basically in idle). Therefore on the plot the first sector is climb, the slope is steeper since engine operates at throttle level higher than cruise. Then there is cruise stage which burn most of the mission fuel. The third stage is descent and the curve is very flat, as the aircraft tries to glide to lower altitude. The last big stage is approach. As the flaps and slats are extended, the drag created is significant and engine no longer operates in idle region. At the end of the mission, roughly 15,000 lb of fuel remains in the tank. It consists of 200 nmi divert fuel, 35 min loiter fuel and 5% extra block fuel.

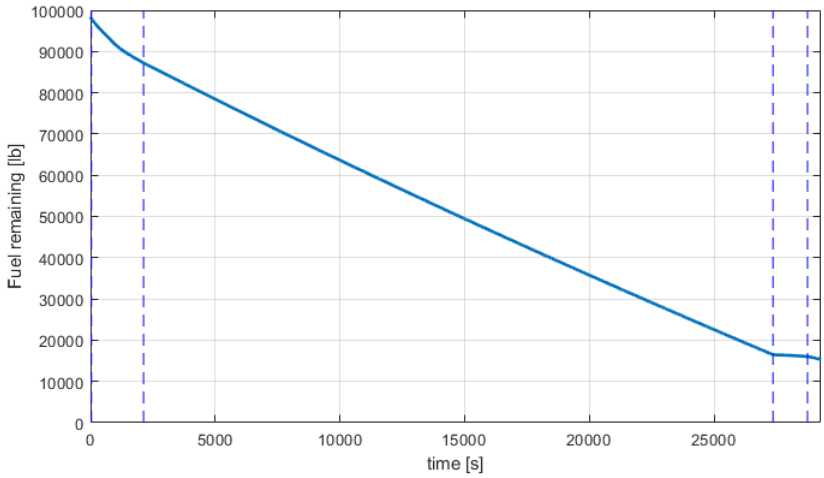

Fig. 38 Fuel plot of simulated flight (3,500 nmi)

Thanks to the UltraFan engine, JJJP has a 20% reduction in fuel consumption compared to Boeing 787 on 3500 nmi mission. Specifically, the fuel consumption per seat is only 1.83 L/100km, compared to 2.26 L/100km [35] for Boeing 787. Similarly, on short-haul mission (700 nmi), JJJP has 13% lower fuel consumption even compared to 737 Max. Specifically, the fuel consumption per seat is only 1.98 L/100km, compared to 2.28 L/100km [36] for 737 Max.

K. Performance Conclusion

The sizing process was conducted with the aforementioned factors in Section XII.A. The 94,300 lb of the total payload consists of 410 people on board, each weighing 200 lb and carrying 30 lb of baggage. The maximum payload weight is set to 150,000 lb so that the aircraft can potentially carry more cargo when flying short-haul flights. In the initial sizing code, the parameters were constrained so that the TOFL and LFL were shorter than 9,000 ft at ISA+15°C. The target range is set to 4,000 nmi with 5% extra of reserve fuel so that there was enough fuel to divert to another airport 200 nmi away and loiter for 35 minutes. In the higher fidelity simulation code, the actual BFL and LFL for the mission were found to be 7,850 ft and 4,420 ft, respectively. Using the parameters and $V_{\text{approach}} = 1.3V_{\text{stall}}$, the approach speed at the end of the 3,500 nmi mission was 141.6 KCAS, fulfilling the requirement of maximum approach speed of 145 KCAS. According to the payload-range diagram 33, the JJJP can carry up to 103,550 lb of payload for 3,500 nmi mission, surpassing the payload budget set at 94,300 lb. In conclusion, JJJP had met all of the performance requirements set in the RFP, including the tradable requirements of approach speed.

XII. Stability and Control

A. Stabilizer Configuration

Several stabilizer configurations were compared against each other for this design, including conventional, T-tail, and cruciform, each having their own pros and cons. Although both the T-tail and cruciform would help ensure the horizontal tail is unaffected by the jet exhaust, the fact that a low wing twin engine configuration was chosen (already putting the horizontal tail well out of proximity to jet exhaust) as well as the added structural weight to support the horizontal tail on the vertical tail made the conventional tail the clear choice. Its proven reliability in stability for similar aircraft and much lighter structural weight pushed this design to adopt it for its stabilizer configuration.

B. Stabilizer Sizing

In order to fully size the horizontal and vertical stabilizer, prior knowledge of some key geometric parameters, namely the volume ratios and moment lever arm between the tail aerodynamic center and the aircraft center of gravity was needed. Although there were historical values for these parameters, many of these had become outdated. Trade studies were done in order to determine volume ratios and moment lever arms of the horizontal and vertical stabilizer. The B777 and B787 were analyzed; the volume ratios and moment arms for these similar aircraft were presented in Table 22 along with the values for the JJJP [37, 38].

Table 22 Tail Sizing Trade Studies

Parameter	B777	B787	JJJP
C_{HT}	0.755	0.921	0.75
C_{VT}	0.054	0.049	0.05
l_{HT}	91.5 ft	81.81 ft	76.65 ft
l_{VT}	87.5 ft	77.04 ft	71.43 ft

The horizontal stabilizer was sized using the scissor plot shown in Fig. 39, constructed using methods outlined in Torenbeek [39]. The vertical stabilizer was sized using the volume ratio method outlined in Raymer [6]. The remaining geometric quantities were sized along historical ranges given in a lecture series by E.G. Tulapurkara [40]. The vertical tail volume coefficient was chosen based off those for the B777 and B787 due to there being doubt that the historical values presented by Raymer were still accurate. Table 23 outlined various geometric parameters of the tail, and a scaled dimensional drawing was shown in Fig. 40. It was chosen to include a horizontal tail dihedral angle of $\Gamma = 6$ deg (matching that of the wing) in order to ensure the stabilizer was completely out of the engine jetwash and disturbed air from the wing, for greater lateral-directional stability, as well as for aesthetic purposes. Lastly, the NASA SC(2)-0010

airfoil, a thin airfoil with thickness ratio of 10% at 37% chord, was chosen for both the horizontal and vertical stabilizers due to its symmetric geometry and transonic capabilities. The small thickness ratio reduced wave drag according to the Delta method [33], and it had the ability to delay shock waves due to its uniform thickness distribution.

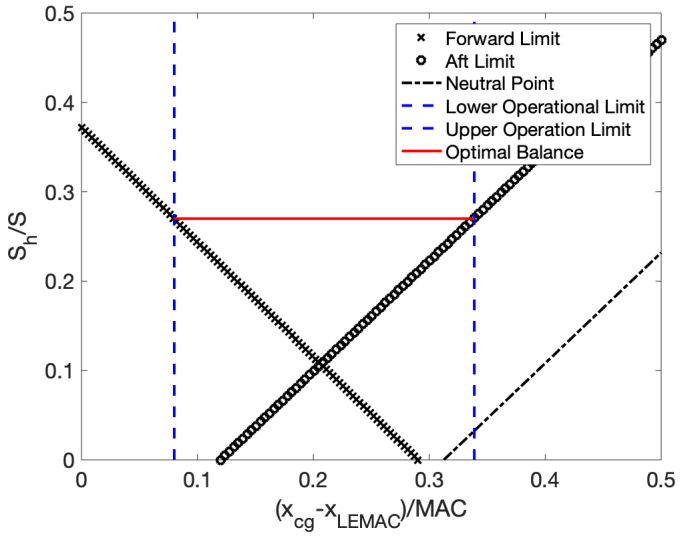

Fig. 39 Horizontal tail sizing scissor plot

Table 23 Tail Sizing

Parameter	Horizontal Tail	Vertical Tail
b	72.62 ft	28.75 ft
AR	5	1.7
λ	0.3	0.31
$\Lambda_{c/4}$	30 deg	35 deg
Γ	6 deg	–
Incidence Range	-2–13 deg	–
Area	1,054.8 ft^2	468.3 ft^2
LE Location	167.83 ft	161.09 ft
Volume Coefficient	0.75	0.05

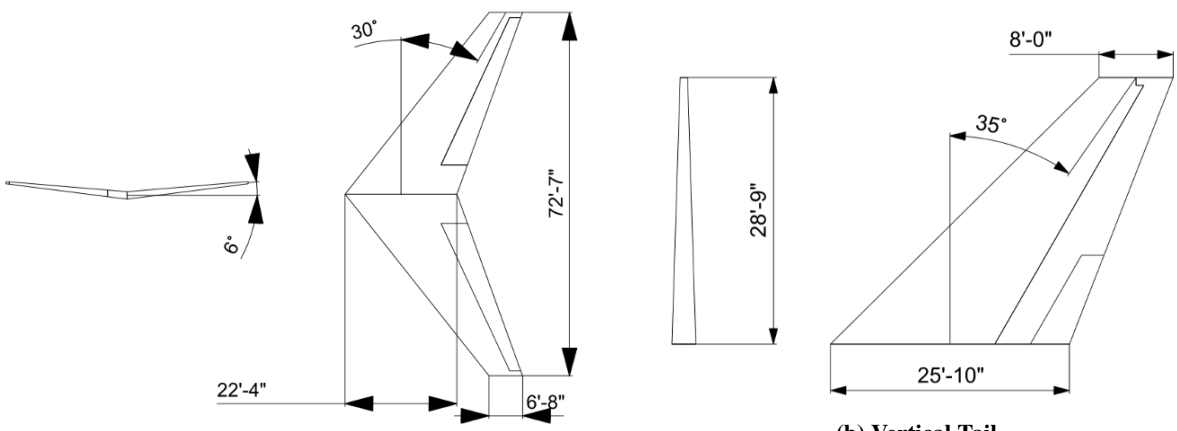

(a) Horizontal Tail **(b) Vertical Tail**

Fig. 40 Dimensional drawings of stabilizers

C. Control Surface Sizing

The JJJP utilized various control surfaces, namely an elevator, rudder, and ailerons, to maintain control of its attitude. All three of these flight control surfaces were sized using historical values given in Raymer [6]. The geometric quantities determined through this methodology were presented in Table 24 and scaled dimensionsal drawings of these devices is presented in Fig. 40 and on page 12. The span ratio and span listed for the aileron is for a single device

Table 24 Control Surface Sizing

Parameter	Elevator	Rudder	Aileron
Chord Ratio	0.4	0.4	0.22
MAC	6.37 ft	7.39 ft	5.49 ft
Span Ratio	0.9	0.9	0.1
Span	65.34 ft	25.88 ft	18.53 ft
Deflection Range	±25 deg	±25 deg	±25 deg

D. Incidence Angles

It was decided that the JJJP's horizontal tail will be able to adjust its incidence angle, allowing for a wide range of incidence angles as shown in Table 23. This adjustable tail design was chosen for the purposes of efficient trimming, allowing the elevator to be used solely for control. Further, Sadraey [41] points out that when flight cost was a major design requirement, it was better to utilize an adjustable horizontal tail instead of a fixed or all-moving tail. Through trim analysis, the necessary tail incidence angles for takeoff, cruise, and landing was determined in order to zero the

pitching moment of the JJJP.

E. Trim Analysis

Trim analysis was done using the methods outlined in and McCormick [42]. It was decided to have a variable incidence horizontal tail for the JJJP; this system was to be used to trim the aircraft, with the elevator being used mainly for control purposes. By varying the incidence of the horizontal tail, trim plots were made for takeoff, cruise, and landing and are presented in Fig. 41. Take note that the convention of positive incidence angle being downward (opposite of the wing) is used here. The goal is to achieve zero pitching moment about the center of gravity at cruise with as small as possible tail incidence, making the aircraft passively stable and requiring little input from the pilot. The wing incidence being 3 deg results in the need of 5.8 deg tail incidence at cruise. During takeoff and landing, there must be a greater tail incidence in order to produce a moment that allows the JJJP to ascend/descend at the proper angle of attack. Trim points were chosen to ensure the necessary lift at each mission segment was achieved. These incidence angles were all within the deflection range stated in Table 23.

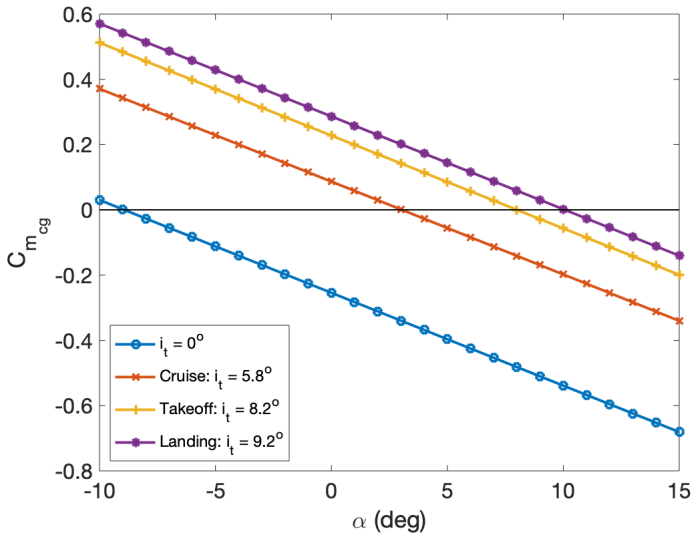

Fig. 41 Trim diagram

F. Longitudinal Static Stability

For the JJJP to have longitudinal static stability, it had to be able to resist changes in AoA by producing an opposing pitching moment. In order words, $C_{m_\alpha} < 0$. Various derivatives related to lift and moments were calculated using methods outlined in Raymer [6] and McCormick [42] and were collected in Table 25.

Table 25 Longitudinal Stability Derivatives

Derivative	C_{L_α}	C_{m_α}	$C_{m_{\delta e}}$	ϵ_α
Value	5.80	-1.63	-1.34	0.37

The negative value of C_{m_α} as well as the downward slopes of the trim plots shown in Fig. 41 indicate that the JJJP possessed longitudinal static stability. An increase in the AoA resulted passively in the production of a restoring pitching moment. Additionally, the negative value of $C_{m_{\delta e}}$ suggested that a positive elevator deflection (pitched up) further resulted in a counterbalancing pitch moment. Further, using equations given in Raymer [6], the neutral point and static margin were found using the forward and aft C_g limits and were tabulated in Table 26. The three lengths were measured from the nose of the JJJP whereas the static margin was given as a percentage of the MAC. Although slightly higher than similar aircraft, this positive static margin nonetheless indicated that the C_g of the JJJP was ahead of the neutral point, proving this aircraft was longitudinal statically stable .

Table 26 Neutral Point and Static Margin

Parameter	Neutral Point	Static Margin	Fore C_g	Aft C_g
Value	109.8 ft	19.3%-55.3%	98 ft	105 ft

G. Lateral-Directional Static Stability

In order to get a full understanding of the JJJP's stability, the lateral-directional static stability was also analyzed. Using the method outlined in McCormick [42], the various derivatives used to determine lateral-directional stability were found and were shown in Table 27. The negative value of C_{l_β} implied that the JJJP naturally produced a restoring roll moment given a change in sideslip angle. The positive value of C_{n_β} indicated that a counteracting yaw moment occurred in the event of a sideslip change. These, as well as the signs of the other derivatives in Table 27 proved that the JJJP was lateral-directional statically stable.

Table 27 Lateral-Directional Stability Derivatives

Derivative	C_{l_β}	C_{n_β}	C_{l_r}	C_{n_r}	$C_{l_{\delta r}}$	$C_{n_{\delta r}}$
Value	-0.124	0.162	0.172	-0.013	0.037	-0.120

H. Dynamic Stability

Dynamic characteristics were also analyzed besides static ones. The six degrees of freedom equations of motion of this aircraft, as given in McCormick [42], were solved for their roots, from which dynamic modes were determined as

well as other characteristics. These findings were tabulated in Tables 28 and 29. All but the spiral mode had negative real part, indicating dynamic stability. However, the doubling time of 53.7 seconds allowed plenty of time for the pilot to correct for this error, making it a nonissue.

Table 28 Longitudinal Dynamic Stability Analysis

Dynamic Mode	Roots	ω_n	ζ	T_P	$T_{1/2}$
Phugoid	-9.3e-4±0.039i	0.039 Hz	0.024	162 s	745 s
Short	-0.40±1.7i	1.7 Hz	0.23	3.7 s	1.8 s

Table 29 Lateral-Directional Dynamic Stability Analysis

Dynamic Mode	Roots	ω_n	ζ	T_P	$T_{1/2}$	τ	T_2
Roll	-1.2	1.2 Hz	1	–	0.6 s	0.85 s	–
Spiral	0.013	0.013 Hz	–	–	–	–	53.7 s
Dutch Roll	-0.044±1.9i	1.9 Hz	0.023	3.3 s	15.8 s	–	–

Additionally, the rudder sizing was confirmed by determining the necessary deflection in the case of one engine inoperative (OEI) for takeoff and landing and was presented in Table 30a. This rudder trim was determined using equations outlined in the lecture notes of Dieter Scholz [43]. With the takeoff rudder trim being well within the deflection range, the area of the rudder was confirmed to be large enough to counteract the most adverse condition of OEI.

Lastly, the FAA required transport aircraft be able to sufficiently perform normal lateral maneuvers with OEI (14 CFR §25.147). Due to the slight ambiguity in this statement, the FAA released in the Advisory Circular (AC) 25-7D [44] that the test case for this would be for the aircraft to perform a roll maneuver through 60 deg (30 deg bank angle in one direction to a 30 deg bank angle in the other direction). This maneuver was to be done within 11 seconds to meet the requirements per AC 25-7D. The roll time calculated from equations in McCormick [42] was shown in Table 30b and was found to be 8.5 seconds, well below the FAA's test case guidelines.

Table 30 OEI Lateral-Directional Control

(a) Rudder Trim

Mission Segment	δr
Takeoff	14.4 deg
Landing	1.2 deg

(b) Roll Time

Parameter	Value
δa	5 deg
Roll time	8.5 s

XIII. Structures and Loads

A. Aircraft Loads Analysis

1. V-n Diagram

In order to determine the aircraft's flight envelope and to understand the structural limits of the designed aircraft, a V-n diagram overlayed with a gust diagram was plotted using methods outlined in Roskam V and is shown in Fig. 42 [45]. This analysis helped find loads experienced during maneuvering and produced by gusts of wind. The gust lines being fully within the boundaries of the solid V-n plot in Fig. 42 indicated gust loads had very little impact on the JJJP. Unlike a much smaller airplane, the JJJP's large weight and high cruise speed allowed it to not be considerably affected by gusts. Further note, the limit load of 2.5 was chosen to comply with the minimum limit load given by 14 CFR §25.337(b).

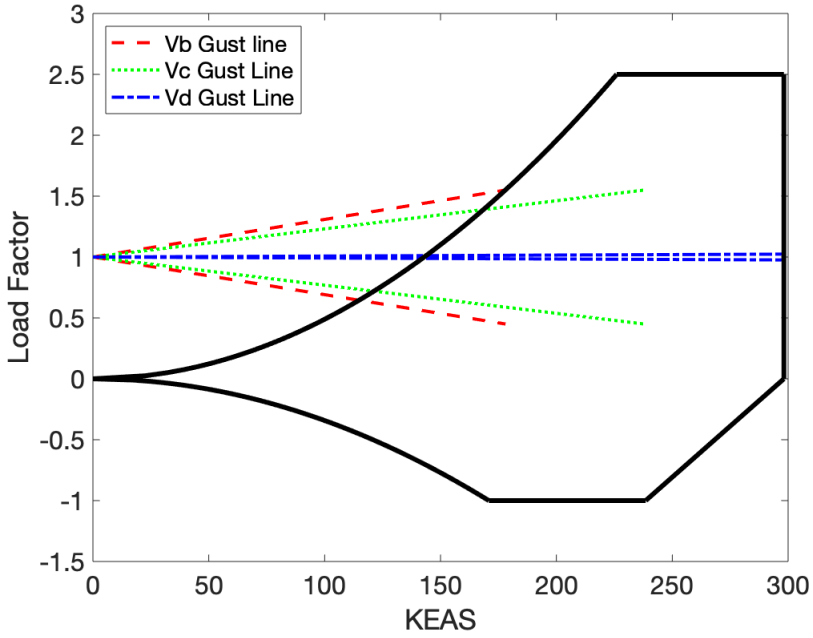

Fig. 42 V-n diagram

2. Load Cases and Load Paths

A qualitative analysis of some of the load cases of interest experienced by the JJJP was shown in Fig. 43. The loads on the wing included lift and the weight of the engine, idealized as a point mass. These forces were transferred from the wing box to the fuselage via skin panels, ribs, and spars. Further, the JJJP's fuselage experienced pressurization loads. With the cabin pressure chosen to be equivalent to the air pressure at 8,000 ft altitude per the RFP [1], a pressure differential of 7.78 psi was present at cruise, these values being tabulated in Table 31. This pressure differential was used to define the minimum skin thickness of the fuselage. These pressurization forces traveled through the fuselage via

the skin, stringers, and longerons. Lastly, the landing loads experienced by the landing gear traveled through the main struts (as well as partially through the supports) to the fuselage.

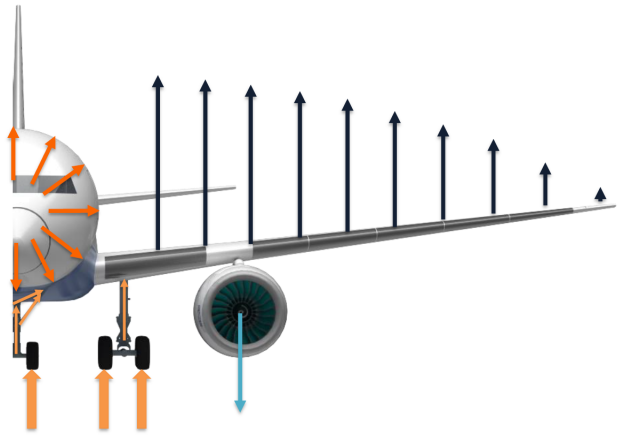

Fig. 43 Load paths

Table 31 Pressurization Parameters

Parameter	Value
Outdoor Pressure	3.14 psi
Cabin Pressure	10.92 psi
Pressure Differential	7.78 psi

Additionally, the lift distribution was approximated using Schrenk's approximation between a trapezoidal and elliptical lift distribution over the wing and was presented in Fig. 44a. From this, moment and shear diagrams for the wing were plotted and were presented in Figs. 44b and 44c. A safety factor of 1.5 was used for this methodology. The moment and shear load were at a maximum at the wing root tapering off to 0 at the wing tip. The ultimate moment and shear values, found at the spanwise root chord location, were found to be 8.084×10^7 lb-in and -1.998×10^5 lb. These plots were used for material sizing and selection, specifically the spars and ribs.

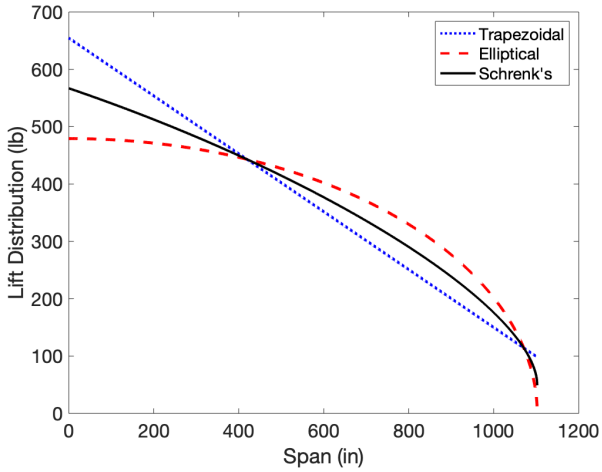

(a) Lift distribution approximation

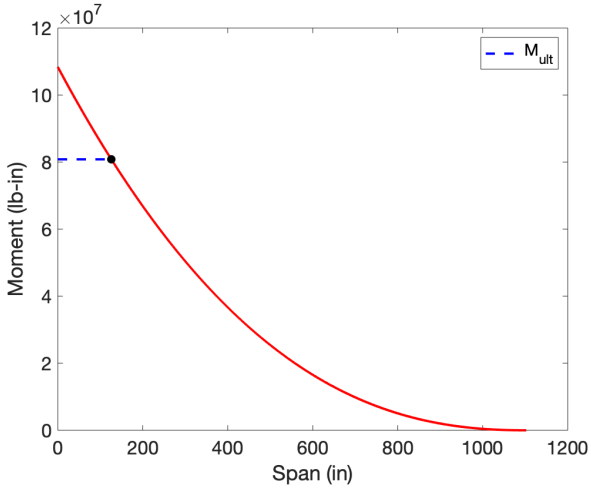

(b) Moment diagram

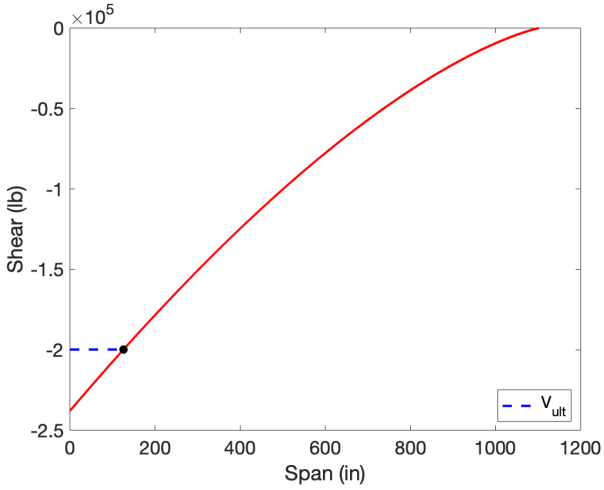

(c) Shear diagram

Fig. 44 Plots to determine ultimate moment and shear load

B. Material Selection

When considering what material should be used in the construction of the main structural components of an aircraft, the two most common materials used are either aluminum alloys or composites.

Depending on the composite, they can have high strength at very low densities making them appealing to the aerospace industry. The major problems that arise when dealing with a composite structure is the high cost of not only the material, but also the complex manufacturing processes involved in a composite layup. Along with a high cost, it is also extremely difficult to mend a composite fuselage and wing together as traditional fasteners will cause a stress concentration that could result in failure at those locations [46]. If these issues are overcome, maintenance becomes another key factor. Composite structures are much harder to conduct repairs on than metal ones and with this aircraft focusing on short hauls, the structure will be prone to fatigue making fast, cheap and reliable repairs vital to keeping the

aircraft flight worthy [46].

With this knowledge, it was decided to go with a primarily aluminum alloy construction. Aluminum alloys have been tested and used in industry for years, are relatively easy to manufacture and test, are readily available, and have many varieties with various material properties.

Because of this, four different aluminum alloys have been chosen to conduct a trade study including Al 2024, Al 7075-T73, Al 6061, and Al 7079. Depending on which structural component is being designed, different material properties of the aluminum alloy should be focused on. For things like the wing spars, ribs, along with fuselage frames a material with a high elastic modulus and yield strength are favored due to the high stress these components will see during every flight. As for the skin of the fuselage and wings, a material with a high elastic modulus is desired as well as high fracture toughness to avoid crack propagation in the case of damage to the surface. The physical properties if all the materials being considered can be seen compiled in Table 32 [47].

Table 32 Physical Properties of Aluminum Alloys

Material	Yield Strength (MPa)	Elastic Modulus (GPa)	Fracture Toughness (MPa-$\sqrt{m}$)	Density (g/cm^3)
Al 2024	324	73.2	26	2.76
Al 7075-T73	434	71.7	20	2.79
Al 6061	276	68.9	29	2.68
Al 7079	450	70	20	–

Based on this information, Aluminum 2024 is considered the best for the skin of the aircraft given its large elastic modulus and fracture toughness. These properties mean that the surfaces can experience high loads and still maintain its shape. For the fuselage this is important since there will be a pressure difference of 7.78 psi between the inside and outside the cabin when cruising at 37,000 ft. Additionally, with a high elastic modulus the fuselage will not bulge as much as a material with a lower elastic modulus. If there is extreme deformation of components such as the wing, the aerodynamics will vary largely from what was predicted, so maintaining the desired shape is critical to maximizing the performance of the aircraft. The fracture toughness determines how fast a crack will propagate in the material, with a higher value corresponding to a slower propagation. Aluminum 2024 has one of the highest values of fracture toughness which means if there is a crack in these surfaces, it will resist fracturing better than most of the other alloys investigated. For structural components such as wing ribs and spars, Aluminum 7075 has been chosen for its high yield strength and favorable elastic modulus, meaning it will be best suited for enduring the high shear and bending loads that these components see during the full flight envelope.

Aside from the main structural components of the wing and fuselage, materials for other various components needed

to be determined. For the landing gear, an aluminum alloy was not a viable option due to the high loads and cycling of this component making it prone to fatigue. Instead, the steel alloy, AISI 4340 was chosen for its high tensile yield strength, allowing for repeated landings with minimal maintenance needed to keep to keep the landing gear in service [48]. Another special consideration had to be given to the radome of the aircraft placed at the tip of the nose. Since all radio signals will need to pass through, aluminum was not an option as it can block many of the signals from being transmitted. To solve this issue the radome will be constructed of s-glass fiberglass which is non conductive and allows the transmission of radio signals, while having a tensile yield strength of 4750 MPa and can operate at a maximum temperature of 590 K making it a competent candidate for this component [49] .

C. Structural Arrangement

The main structural components of the the JJJP are analyzed in this section, including the fuselage, wing, empennage, and horizontal and vertical stabilizers. Each of these components have structural configurations meant to handle and distribute the loads expected through the full flight envelope to ensure failures will not occur. The complete structural configuration can be seen in Fig. 45.

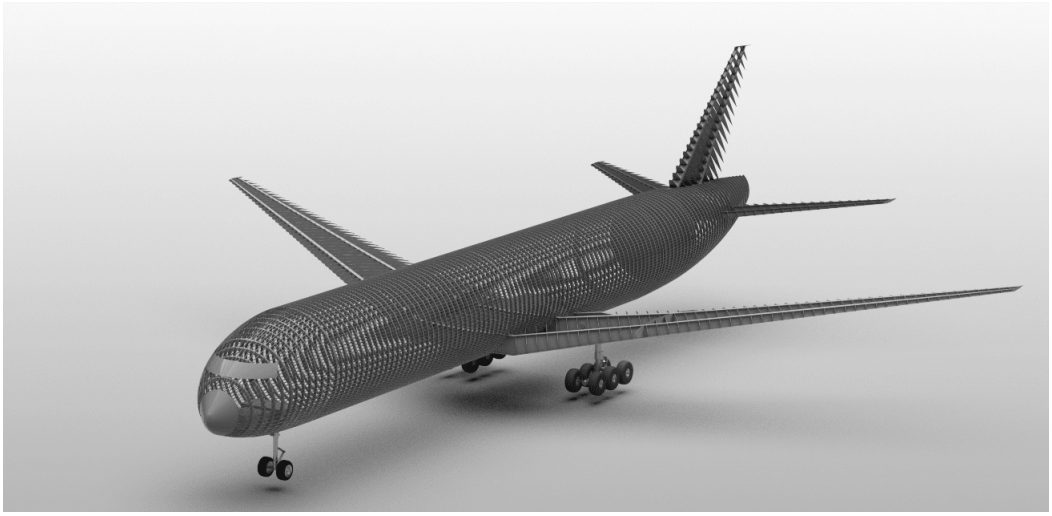

Fig. 45 Complete Aircraft Structure

1. Wing Structure

The main wing structure consists of a series of ribs attached to two main spars that run the length of the wing and connect at the center in the wing box as shown in Figure 46. Along with the main spars, there is also supplementary spar placed near the root of the wing that acts as a support for the landing gear strut.

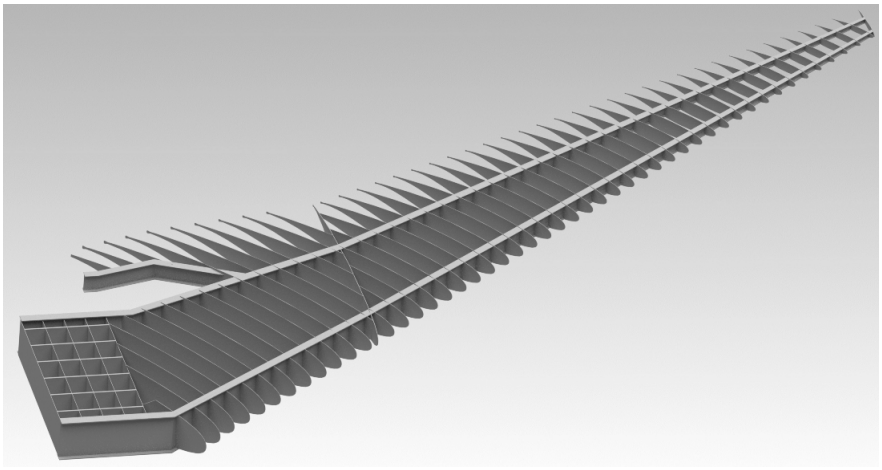

Fig. 46 Wing Structural Arrangement

This configuration is very common in the aerospace industry, especially for this class of transport aircraft, since it provides a large amount of strength while maintaining a relatively low weight to maximize performance [7]. The front and rear spar locations are typically constrained by the location of the the high lift devices on the wing, with a larger torque box being advantageous in rib sizing as the thickness can be reduced since there is better distribution of the shear torsional forces experienced during flight. For these reasons, the front spar was placed at 14% of the chord and the rear spar located at 60% of the chord along the span of the wing. The exact size of the spars was determined by the ultimate bending moment experienced at the interaction of the wing and body, while being constrained by the thickness of the wing at that location [50]. A diagram of the front and rear spar dimensions is shown in Fig 47.

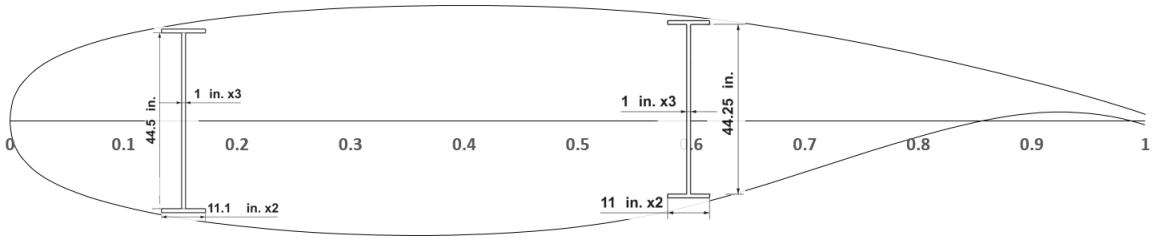

Fig. 47 Spar location and size at the root of the wing

Once the spar size and locations is determined it is then possible to size and space the ribs along the span of the wing. To do this, an idealized wing box analysis was used to calculate the shear flow through the rib at the intersection between the wing and fuselage as this is the location of the ultimate shear force experienced. Again the exact methodology to determine the rib thickness was done by following the methodology outlined in Niu [50]. From this the rib thickness was determined to be 0.35 in. thick which was kept consistent along the wing for consistency and ease of manufacturing. As for the spacing, an approximation was used from historical data of transport aircraft and was chose to be 24 in. apart

as presented in Roskam part 3 [7]. The orientation of the ribs was also considered as there are two primary option of doing so. The first option would be to have the spars parallel to the freestream. The advantage of this configuration is that the wing airfoil shape is held more accurately down the span of the wing, resulting in a slight improvement in the performance of the aircraft. The major drawback of this configuration is the fact that there are large stress concentrations at the intersection between the rib and the front spar resulting in reinforcements needed at these locations[50]. For this reason, the ribs were placed perpendicular to the front spar resulting in a more structurally sound construction.

Once the preliminary sizing of the wing structure was completed, a linear elastic finite element analysis was done to verify it could withstand the loads expected during the full flight envelope. To do this, a lift distribution taken from 1g Shrenks approximation during cruise conditions was applied to the wing of the aircraft down the span. Since the skin was not modeled in this simulation, the lift force was distributed along the top surface of the front and rear spar with the front spar taking 56% of the load and the rear spar taking 44%. This was decided based on the location at which the lift acts about at the root then doing a summation of the moments experienced by the front and rear spar. Along with lift, a point force was placed at the location of the engine to represent its effects on the structure during flight. Once this was done, the solution was obtained using the Nastran solver built into NX 12.0 , with the results shown in Figure 48.

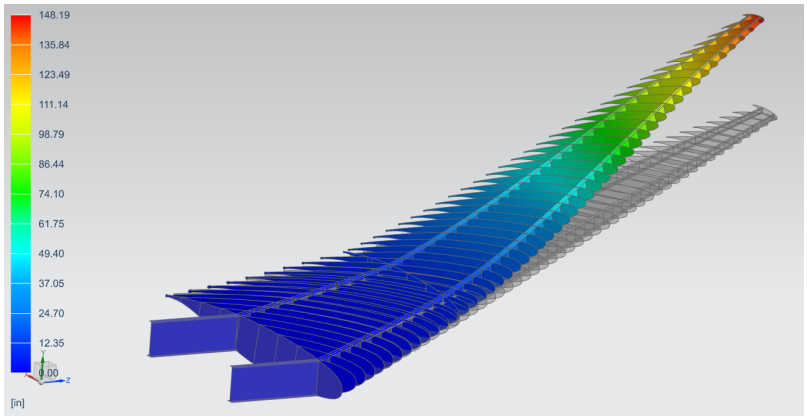

(a) Deflection of the wing.

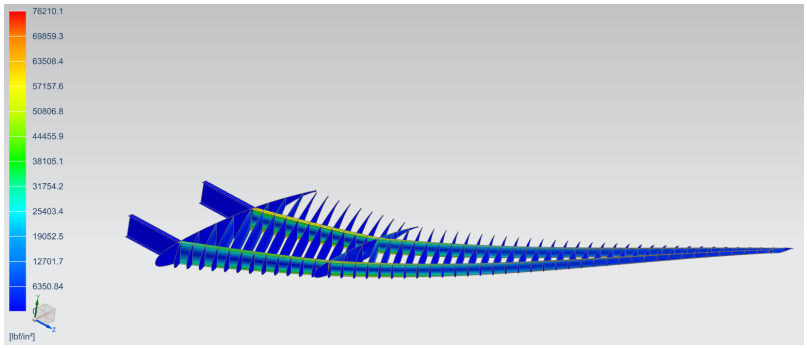

(b) Stress throughout the wing.

Fig. 48 Finite Element Analysis Results

From the simulation, it was determined that throughout most of the wing structure the stress levels were around 35,000 psi, along with a total displacement of 12.3 ft of the wingtip. Although it should be noted that the maximum stress value was seen at a single node where the wing and fuselage intersect, and is likely an unrealistically high value do to the way the mesh was constructed and connected at that location. Throughout the rest of the wing, The highest values observed were around 60,000 psi, which is well beneath the yield strength of 73,000 psi for Aluminum 7075. In terms of the deflection of the wing, a 12.3 ft deflection is consistent with aircraft of similar size, with the Boeing 777 having a maximum deflection of 15.5 ft [51], and the Airbus A350 seeing a maximum deflection of 17.6 ft [52]. Further refinement of the FEA setup may be helpful to get more accurate results for the maximum stress, allowing for iterations to be done optimizing the structure of wing.

For the attachment method used, a wing box is constructed running the width of the fuselage. This consists of two I-beams extended from the wing spar with longitudinal supports to add torsional rigidity. The wing box is connected to the frames of the fuselage by a series of bolts. Both wings will be bolted onto the wing box where they meet at the fuselage wing intersection with a set of lugs on the front and rear spar. This will allow for the aerodynamic forces to be efficiently transferred from the wing to the spars and absorbed by the wing box.

2. Fuselage Structure

The fuselage construction followed similar methodologies to that of the wing. The main structural components of the fuselage consist of the frames, stringers, bulkheads, and skin. Many of these parameters were determined following approximations found in Roskam Part 3 [7]. The results of this can be seen in Table 33.

Table 33 Dimensions of Fuselage Structural Components

Component	Frame Depth	Frame Spacing	Stringer Spacing	Skin Thickness
Value	6.04 in	20 in	9 in	0.07 in

Since the JJJP will be flying at an altitude of 37,000 ft, it is essential that the cabin be pressurized to a maximum of 8,000 ft pressure altitude. This means the inside of the cabin will have to maintain a pressure of 10.92 psi throughout the entire flight envelope, with a pressure difference of 7.78 psi between the cabin and atmosphere during cruise. The pressurization was used in determining the skin thickness of the fuselage. To do this, a thin walled hoop stress analysis was done to find the thickness required for safe operation of this aircraft [53]. Frame spacing and depth for this aircraft was done using the approximations outlined in Roskam Part 3 [7], then confirmed with a similarity analysis using a structural layout diagram of the Boeing 777-300. Using Siemens NX 12.0 to scale the image and measure the distance between frames, it was found that the Boeing 777-300 has a frame spacing of 21.5 inches, which very similar to the

frame spacing used on the JJJP. These results were to be expected as the size of both aircraft are very similar. Another design consideration taken into account of the fuselage came with the shape of the stringers to be used. Two of the most common shapes used in this class of transport aircraft are J-stringers and Z-stringers. Z-stringers are very structurally efficient at transferring loads and use less material to that of a J-stringer. J-stringers are less structurally efficient, but have the advantage of dual fasteners due to its geometry [50]. Although this is a beneficial fail safe to have, lower weight due to the smaller size and fewer fasteners needed for the Z-stringer proved to be more important than the extra fastening surface provided with a J-stringer.

Bulkhead and mainframe placement was also something to be considered when designing the structure of the fuselage. A total of two bulkheads and three mainframes were decided to be used on the JJJP. The bulkheads were placed in the nose and tail of the aircraft to maintain pressurization of the fuselage. The mainframes are placed right after the cockpit as well as at the front and rear spar of the wing box allowing for the loads from the wing to be transferred to the rest of the airframe structure. The full fuselage construction can be seen in Fig. 49

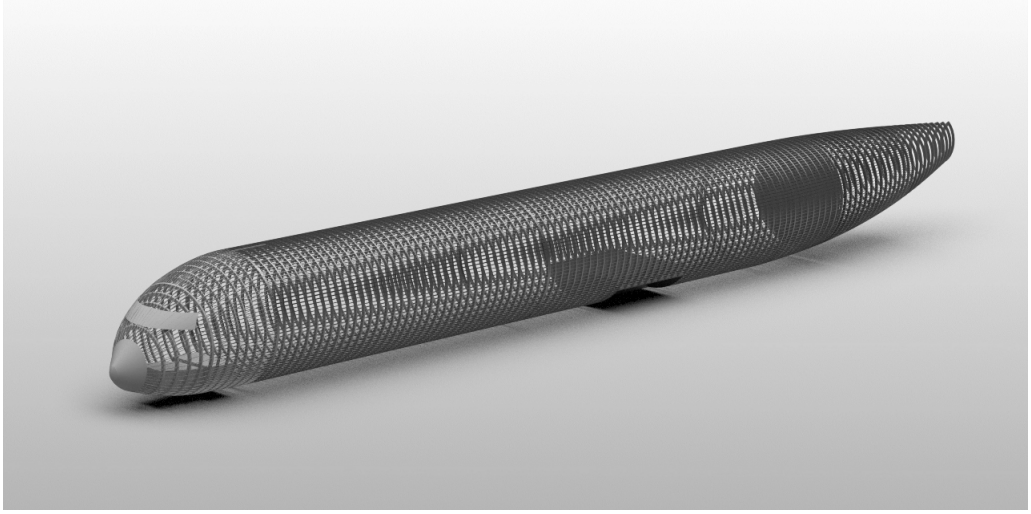

Fig. 49 Fuselage Structural Arrangement

3. Empennage Structure

The philosophy behind the empennage construction was the same taken as the fuselage and wing shown earlier. The tail cone section has identical frame and longeron dimensions as the fuselage tapering all the way down to the tip of the tail. While the horizontal and vertical stabilizers follow the same construction as the wing with two main spars and ribs perpendicular to the leading edge spar. The spacing of the ribs in the tail is set to 24 in. apart matching the estimations shown in Roskam Part 3 [7]. The horizontal tail surface also has a wing box similar to that of the wing, while the vertical tail will be mounted to the top of the fuselage along a reinforced longeron placed along the top surface of the tailcone. The horizontal and vertical stabilizers can be seen in Fig 50.

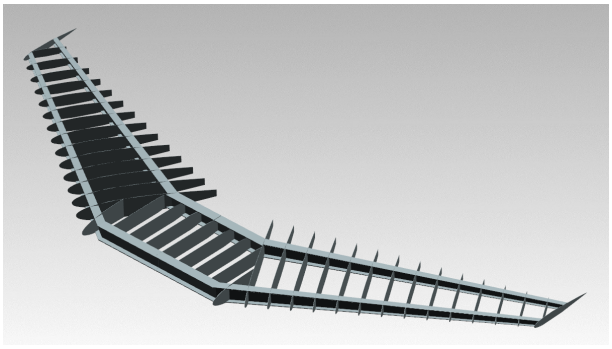

(a) Horizontal Stabilizer Structure

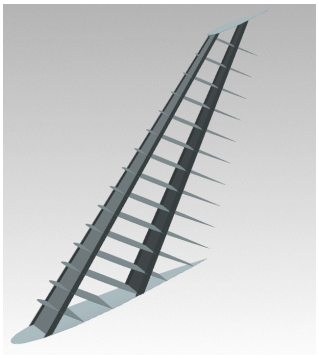

(b) Vertical Stabilizer Structure

Fig. 50 Vertical and Horizontal Stabilizer Structure

XIV. Mass Properties

A. Aircraft Component Weight Estimations

In Part V of his book, *Airplane Design*, Roskam provides two methods of estimating airplane component weights: Class I and Class II [45]. Class I consists of an empirical sampling estimation, wherein weights from other aircraft in the same class are averaged and scaled based off of the designed-aircraft's gross weight. Class II utilizes equations based on the aircraft's geometry and structure in order to estimate weights for the following components: fuselage, empennage, fixed equipment, powerplant, landing gear, nacelle, and wing [45].

Table 34 Configuration Datum

	x	y	z
Direction	Parallel to Ground Along Length of Fuselage	Parallel to Ground Span-wise Direction of Wings	Height of Aircraft
Location of 0	Tip of Nose	Tip of Nose	Ground

Table 35 Roskam Class I Weight Component Estimations

Component Group	Weight (lb)	C_g Location (x,y,z) (ft)
Wing	54,000	(90,0,15.5)
Landing Gear (Nose)	6,500	(19,0,4)
Landing Gear (Rear)	13,000	(105,0,4)
Empennage	33,000	(193,0,26)
Fuselage	50,000	(110,0,18.5)
Fixed Equipment	76,000	(110,0,18.5)
Nacelle	7,000	(88,0,7.5)

Using the Roskam Class I estimation method, a 2-dimensional analysis was performed to estimate the component weights of the aircraft. The weights were estimated using the methodology and data provided on page 11 in Part V [45]. The resulting weight estimations are provided in Table 35, along with the location of their respective C_g with respect to the datum described in Table 34. The analysis was limited to 2 dimensions, as landing gear height, engine pylon length, vertical tail span, and other parameters were in the process of being defined at the time of this analysis. The analysis was further simplified to one dimension (along the length of the fuselage), due to a symmetrical configuration.

The component weight analysis was expanded by performing Roskam's Class II method for determining component weights [45]. In this method, Roskam provides equations from four sources: US Air Force, Cessna, General Dynamics, and Torenbeek [45]. Roskam's commentary suggests that the equations from General Dynamic and Torenbeek should be representative for aircraft of this class. Both sets of equations were evaluated and the results were averaged for a final Class II estimation.

Finally, the resulting weight estimations were validated against the weight fractions that were provided by Roskam Class I analysis and the Boeing 787-8, for reference [54]. In some cases, the Class II equations specified weights for sub-components of the weight groups. The resulting weight groups and their sub-component weights are provided in Tables 36 and 37.

Table 36 Roskam Class II Weight Fractions (Component/W_E)

Weight Component Group	Class II Empty Weight Fraction	Class I Empty Weight Fraction	787-8 Empty Weight Fraction
Wing	0.13	0.11	0.12
Landing Gear	0.06	0.04	0.04
Empennage	0.02	0.02	0.02
Power Plant	0.06	0.07	0.07
Fuselage	0.10	0.10	0.09
Fixed Equipment	0.12	0.16	0.15
Nacelle	0.01	0.01	0.01

Table 37 Roskam Class II Weight Estimations

Component Group (Sub-Components)	Equations Used [45]	**Total Weight** (Sub-Component Weight) (lb)	C_g Location (x,y,z) (ft)
Wing	5.7	**62,000**	(101.5,0,15.5)
Landing Gear		**28,000**	
Nose Gear	5.41, 5.42	3,600	(25,0,4)
Main Gear	5.41, 5.42	24,400	(120,0,4)
Empennage		**11,000**	
Horizontal Tail	5.19	8,000	(179,0,24)
Vertical Tail	5.20	3,000	(174,0,37)
Fuselage	5.26,5.27	**48,500**	(85,0,18.5)
Nacelle	5.35,5.37	**5,000**	(90,0,7.5)
Powerplant		**30,500**	
Engine	Estimation From Similarity Analysis	26,000	(90,0,6.5)
Air Induction System, Engine Controls, Starting System	6.9,6.10	500	(145,0,18.5)
Fuel System	6.20,6.23	4,000	(136,0,6.5)
Fixed Equipment		**56,500**	
Flight Controls	7.5,7.6	4,400	(101.5,0,18.5)
Hydraulics & Pneumatics	Roskam Section 7.2 [45]	6,500	(145.5,0,18.5)
Electronic Systems	7.15,7.17	2,300	(145.5,0,18.5)
Instruments, Avionics, Other Electronics	7.23,7.25	5,200	(20,0,18.5)
Air-conditioning, Anti-Ice System, Pressurization System	7.29,7.30	4,200	(101.5,0,18.5)
Oxygen System	7.35,7.38	1,200	(145.5,0,18.5)
APU	7.40	300	(174,0,23.75)
Furnishings	7.44,7.45	27,000	(85,0,18.5)
Baggage and Cargo Equipment	7.48,7.49	2,200	(145.5,0,18.5)
Paint	7.51	3,200	(85,0,18.5)
W_E		**241,500**	(102,0,15)

Provided the component weights found in Table 37, along with the parameters (i.e. fuel weight) found in the initial sizing analysis, a comprehensive list of relevant operating weights can be found in Table 38.

Table 38 Operating Weights

Operational Status	MTOW	MRamp	MZFW	MLW	W_E
Weight (lb)	443,000	446,000	382,000	390,000	241,500

B. Structural C_g

Using the data from the two Roskam weight analyses, a C_g can be estimated for the aircraft structure. In addition to the Roskam weight estimation method, the Mass Properties Engine in OpenVSP was used to calculate a C_g of the model. The calculation is performed by dividing the model into 150 segments and calculating a C_g from using the segment weights. Similar to the Roskam Class I analysis, the OpenVSP analysis was limited to a single dimension. The OpenVSP model was later migrated to Siemens NX. The mass properties tool in NX also calculates a C_g value. The resulting C_g values are recorded in Table 39.

Due to lower fidelity in both the OpenVSP model and the NX model, in comparison to the constructed aircraft, the structural C_g values provided by the modeling methods are used only as validation for the values from the Roskam calculations. Furthermore, as the Class II values incorporate aircraft-specific geometry, rather than exclusively empirical data, the structural C_g provided by Roskam Class II was used as the final value.

Table 39 C_g Estimations

Method	C_g Location (x,y,z) (ft)
Roskam Class I	(101,–,–)
OpenVSP Mass Properties Engine	(106,–,–)
NX Mass Properties Engine	(104,0,10)
Roskam Class II	(102,0,15)

C. C_g Travel

As a result of attitude changes (e.g. pitching during take-off) and fuel burn, the C_g will shift during a mission. Furthermore, for any given flight, it unknown how full the passenger and cargo cabins will be, respectively. Thus, a calculation must be performed for C_g that accounts for the extremes (forward or aft) in possible loading distributions. To account for this, Torenbeek suggest that a load and balance diagram be derived by calculating C_g at a variety of extremes. These extremes account for MTOW, MZFW, MLW, OEW, take-off pitch, landing pitch, and fuel burn [55].

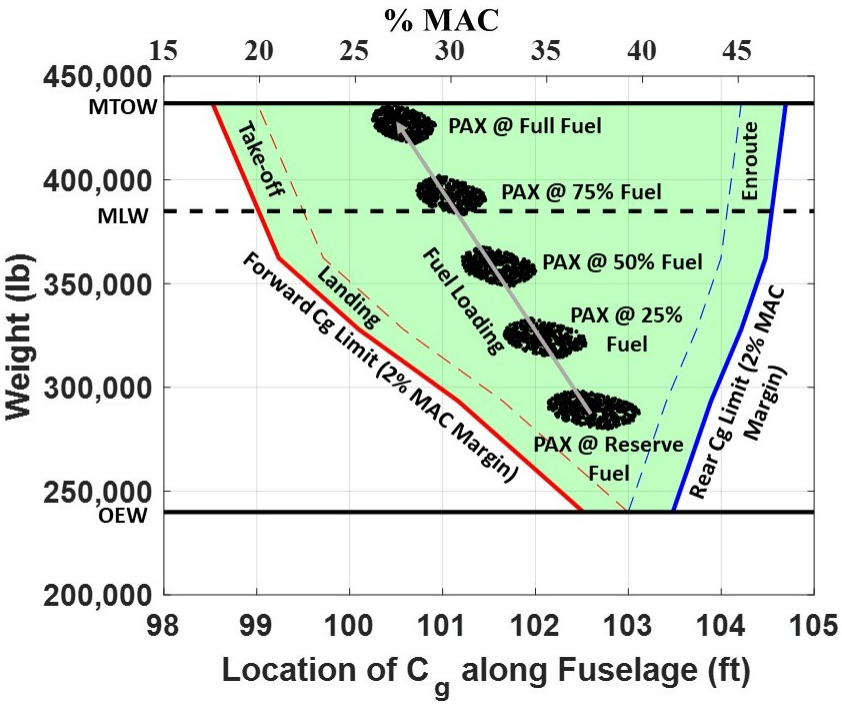

Fig. 51 Loads and Balance Diagram

As shown in Fig. 51, the C_g of the aircraft travels from 98.5 ft to 104.7 ft aft of the nose (17.5% MAC to 47.5% MAC) – the shaded region of the plot. To capture this travel, the C_g of the fuel was set to be entirely at the front, center, and rear of the fuel tanks, respectively. The total aircraft C_g was calculated at each of these increments, as well as across a range of remaining fuel weights.

Torenbeek describes the loading and distribution of passengers to be entirely arbitrary [55]. Thus, the C_g travels due to passenger distribution. To capture this phenomena, a Monte Carlo simulation was ran, where in the number of passengers and crew were randomized in a uniform distribution from zero to 410, and their respective seating locations were randomized, provided the seat layout described in Section VIII.C. Aisles, galleys, and restrooms were included in the possible locations where weight my exists, accounting for the full interior of the cabin. The simulation was run 5000 times per operational loading condition (e.g. MTOW, MLW, varying fuel weight, etc.). The result of the Monte Carl simulation was distinct clusters of passenger-driven C_g travel. Torenbeek describes this behavior as the “loading potato” [55].

Finally, Torenbeek notes that “a margin of a few percent M.A.C is usually assumed” [55]. Thus, a forward and rear limit was set with a 2% MAC margin.

D. Cargo Hold Location Trade Study

Interestingly, it became quickly evident that the traveling C_g, as a result of the randomized passenger distribution, followed a nearly-quadratic trend with linear decreases of operational weight. This discovery yielded the question of whether the location of the baggage hold (i.e. the location along the length of the fuselage allocated for baggage and other cargo) could offset this quadratic trend, trying to keep the C_g as close to the structural C_g as possible during the flight. A similar Monte Carlo simulation was run, repeating the process, but with the location of the cargo load being the randomized variable. The qualification for success of this trade study would be a quantifiable increase in flight duration that the C_g remained close to the structural C_g during flight. After completing the Monte Carlo simulation, it was found that the only way the cargo loading would have sufficient offsetting effects was in lucky cases where the location of the cargo grossly opposed the loading of the passengers. It was assessed that the randomization of the passenger loading could easily vary flight-to-flight. Thus, the location of the cargo hold was determined exclusively by stability-driven requirements, similar to the wing placement and other high weight components.

XV. Landing Gear

A. Trade Study

The first step in designing a landing gear system is deciding what type of configuration will be optimal for the application at hand.The first decision to be made is weather the landing gear system will be fixed or retractable. The factors when deciding are based on drag, weight, cost, and maintenance. Although cost and weight are important, for transonic flight the drag produced will be the major factor in deciding what system to pursue. For this reason, fixed landing gear will not be realistic option for this type of aircraft as the drag being produced during cruise will have detrimental effects on the performance expected. The next decision needed to be made is the configuration to be used on this aircraft. The three most common types of landing gear are tricycle, bicycle, and tail draggers. When choosing a configuration for a transport aircraft, the factors deemed most important are stability of the system, line of sight, ease of use, and practicality [56]. A figure of merit can be seen in Table 40 , with the weighting system of 1-3. For this study a 3 was most favorable while a 1 is unfavorable. The basis for which stability was determined came from the likelihood of a lateral tip over and loss of control when steering on the runway. Line of sight is taken into account for the pilots visibility of the runway on takeoff and landing based off of the landing gear configuration. Ease of use took into account the takeoff and landing procedure with each type of landing gear configuration. Practicality was based off of the space and placement available for the landing gear on this particular plane being designed.

Table 40 Landing Gear configuration Figure of Merit

Factor	Tricycle	Bicycle	Tail Dragger
Stability	3	1	2
Line of sight	3	2	1
Ease of use	3	2	1
Practicality	3	1	2
Total	12	6	6

Based on this assessment, the tricycle landing gear configuration is the best choice for this situation, as is of no surprise as this is almost exclusively the configuration chosen of other aircraft in the same class. This configuration results in favorable ground control, a level floor during taxi for comfort of the passengers, as well as easy takeoff and landing procedures for the pilots.

B. Configuration

Once the configuration is selected it is then possible to determine the location and height of the main and nose gear. The most aft cg location was used to ensure stable takeoff and landing procedures. The dimensions were calculated following the methods detailed in Roskam Part II meeting the criteria for lateral tip-over, longitudinal tip-over, and ground clearances [57]. With the dimensions of the landing gear known as well as the MTOW, the next step would be to determine the loads experienced by the nose and main gear. This was done again following the approximation in Roskam Part II [57]. These equations give an estimate for the loads experience by the landing gear and with this information it is possible to use Table 9.2 in Roskam Part II to estimate the size of the tires needed as well as the number of wheels per strut [57]. The results of the calculations for the landing gear to be used on the designed aircraft are shown in Table 41.

Table 41 Landing Gear Specifications

	Distance from Nose	Height	Wheels per strut	Tire size (in x in)	Tire Pressure	Load per Strut	Shock Absorber Length	Shock Absorber Diameter	Shock Absorber Stroke Length
Nose Gear	21 ft	10.5 ft	2	40 × 15.5	190 psi	2.91×10^4 lb	17.4 in.	6.2 in.	12 in.
Main Gear	108 ft	11.4 ft	6	52 × 20.5	200 psi	2.13×10^5 lb	17.4 in.	15.7 in.	10 in.

With the current landing gear configuration, the tailstrike angle was calculated to be 15 deg and a lateral tipover angle of 12 deg. These values are both sufficient in preventing tail strikes from happening on takeoff or landing as well

as providing clearance for the nacelles while taxiing. After the loads, location, and height of the landing gear system were determined, it is then necessary to go a step further and obtain information on the shock absorbers required for a safe landing. Oleo shock absobers were chosen to be used due to their high efficiency at transferring the loads to the airframe structure upon landing, and the sizing methodology used follows what is shown in Roskam Part 4 and takes into account descent rate as well as the maximum landing weight [56]. The results of these calculations can also e seen in Table 41. Knowing the exact dimensions along with the expected load, exact tires were then selected for this aircraft. For the nose, Goodyear 405K89-2 Flight Leader tires were chosen and are rated for 39,500 lbs which is well above what is expected. For the main gear, Goodyear 520K09-7 Flight Leader was chosen which are rated at 63,700 lb [58]. This is well above the 35,500 lb of force expected by each tire on the main gear, allowing for a large factor of safety and ensuring a safe landing is possible even in the event of a tire blowout. Due to the high loads of seen by the landing gear during every flight, a material stronger and more durable than Aluminum must be used to maximize lifespan of this system. For this reason AISI 4340 will be used for its favorable strength, toughness, and fatigue strength. Although there are stronger titanium alloys, the cost of these materials is much greater and the physical properties of the steel chosen will be adequate for this application.

For the actuation system of the landing gear, the nose gear will retract forward into the nose of the aircraft as this is the safest configuration since it reduces the chances of the gear shearing off during landing. A forward retraction also allows for gravity to assist in the deployment of the gear in the case of a failure in the retraction system. The main gear will fold inboard to the wing and fuselage structure as this is optimal for avoiding systems such as fuel tanks and high lift devices located in the wing structure. The retraction system will be hydraulically powered as discussed in the Systems subsection. A visualization of the stowed landing gear configuration can be seen in Fig 52.

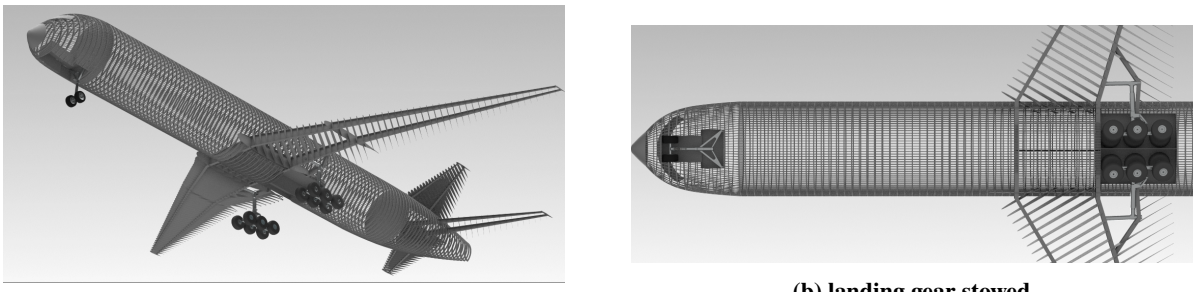

(a) landing gear retracted

(b) landing gear stowed

Fig. 52 Landing gear configurations

XVI. Folding Wingtip System

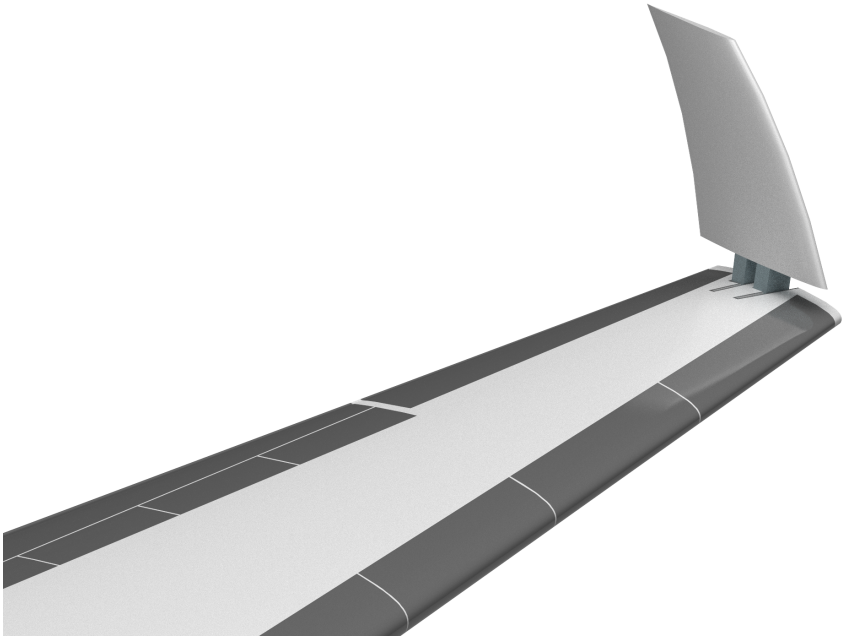

Fig. 53 Folding wingtip CAD model

A. Structures

The wing frame includes additional structure at the folding wingtip hinge and surrounding location to ensure integrity during flight. The main wing section and wingtip have two sets of 0.175 in ribs at the hinge boundary. The hinge itself is composed of two sets of 0.5 in titanium brackets and shafts. The maximum loads on the hinge are during flight, and are determined by the shear and moment calculations based upon a schrenk's lift distribution. The resulting shear and moments acting on the hinge are 4,800 lb and 186,000 lb-in respectively, which includes a 1.5 safety factor. Utilizing a FEM analysis, the maximum equivalent (Von-Mises) stress of the brackets was determined to be at the shaft holes. The bracket thickness was then sized to be meet a 1.25 safety factor, at 0.5 in thick. Four sets of shafts are utilized for rotation and locking of the hinge. The shear and moment forces result in a maximum transverse load of 44,000 lb per shaft. The resulting shear stress is low enough to ensure a safety factor of 5.

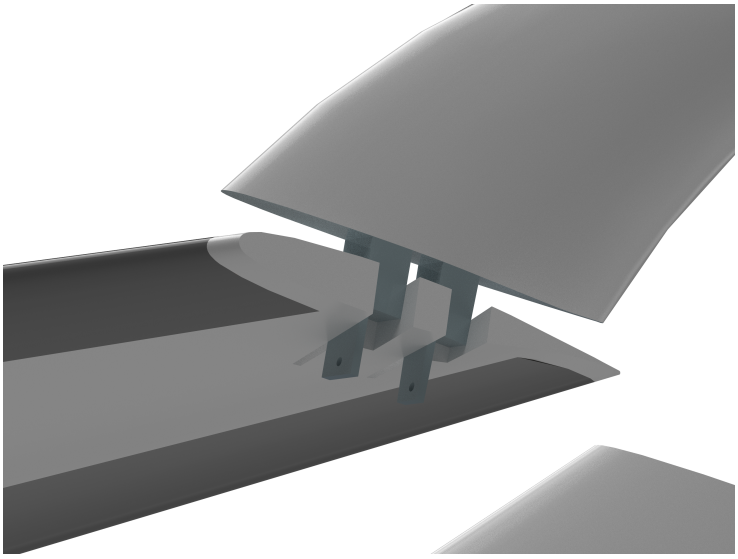

Fig. 54 Folding wingtip structural hinge CAD model

The structural weight breakdown can be seen in Table 42. The total weight is approximately 100 lb.

Table 42 Wingtip Structures Weight

Structures Weight Per Side	Weight
Hinge Brackets	18.3 lb
Ribs	21.3 lb
Rotating and Locking Shafts	10.6 lb
Total per Side	50.2 lb

B. Systems

The systems within the folding wingtip are a significant part of the logistics and weight of the overall wingtip design. There are two major actuation systems being used that consist of four total actuators. Two electric actuators are being used to lock the wingtip in place during flight mode. They only require a small amount of power to slide the pins in and out of place, so electric actuation is a viable option in this case. The other two actuators will be hydraulic rotary actuators that actuate the wingtip up and down. This system was chosen to be hydraulic because it contrasts with the electric locking actuator which in turn makes the wingtip systems less likely to fail all at once. The hydraulic actuators were also chosen because the design will use the close-by hydraulic power from the ailerons when the plane is on the ground. The system was designed this way because aileron actuation is not needed during taxi, so some hydraulic power can easy be rerouted to the wingtip system with very little extra hydraulic line run.

The wingtip folding system was designed with rotary actuation because after an analysis of linear actuation, it was decided that with the hinge design, the moment arm and stroke of the actuator would make it difficult to actuate the wingtip properly. This was because of the very small moment arm the actuator would have, along with the fact that the arm would have to stick out of the bottom of the wing. This would make a gap in the wing skin that would need to be filled, but fixing this problem would add more complexity and weight to the design. The rotary actuator has a simpler process for this design, making it a better choice.

The wingtip rotates on a hinge inside the end of the wing. The rotary actuator will rotate the hinge pin and the wingtip with it that will be fixed to the hinge pin. To calculate the weight added by these systems, a simple analysis was done. The moments from both weight of the wingtip along with potential gusts were calculated as a function of the angle that the wingtip is folded to determine the maximum torque that the actuators would have to overcome at any one point in time. It was determined that the maximum torque from weight comes at 0 deg (extended position) and maximum torque from gusts comes from 90 deg (folded position). Overall, adding them together does not result in a significant increase at torque for any one point, as they are biggest at opposite angles. Through this calculation it was found that the actuators needed to overcome a torque of 8,600 lb-in. Adding an extra factor of 10 percent to allow the actuation to occur in a timely manner makes the torque needed 9,500 lb-in.

After determining a torque needed, an estimate could be made on the weight of a system. Using existing aerospace grade hydraulic rotary actuators from companies such as Parker, an estimate of weight of the system was found using linear interpolation based on the ranges of torque and weight of the existing actuators [59]. The actuators for the locking mechanism only move the pin into place, so they were estimated off the size of small linear actuators from Moog [60]. Table 43 shows the weight added by the wingtip systems. The total systems weight added for both sides is 85 lb.

Table 43 Wingtip Systems Weight

Actuator Weight Per Side	Weight (lb)
Rotary Actuator	37.5
Locking Actuator	5
Total Per Side	42.5

C. Folding Wingtip Trade Study

The primary motivation for the folding wingtip system was to gain the performance benefits of a 184 ft wingspan while maintaining access to Group IV airports that require a 171 ft wingspan. A larger wingspan results in lower fuel required but a heavier wing and resulting aircraft. For this design decision to be valid, the decrease in fuel cost must be greater than the increase in unit cost. As such, a trade study was performed between two cases - an aircraft with 184 ft

wingspan and folding wingtips (the JJJP) and an equivalent aircraft with a 171 ft wingspan and no folding wingtips.

The initial respective aircraft were based upon the optimal aspect ratio and wing area as determined by the sizing analysis in section VII. The empty weight calculation is based on the Roskam Class II weight estimation methodology [45]. The fuel burn is based on the timestep integration specified in section XI. The fuel burn calculation is based on a 700 nmi mission with a 400 passenger payload and the minimum fuel necessary to meet the range.

Table 44 Trade Study Performance Comparison

Wingspan	184 ft (JJJP)	171 ft
Wing Area	3,880 ft^2	3,565 ft^2
Aspect Ratio	8.7	8.2
L/D	16.3	15.6
Empty Weight	241,500 lb	229,200 lb
Fuel Burn	18,240 lb	18,390 lb

Utilizing the CERs specified in section XVIII, a cost analysis was performed based upon the parameters specified in Table 44. The unit cost was based off the Roskam unit cost analysis, assuming 1000 units manufactured [61]. The operational cost was based off the Raymer operating cost analysis, assuming 4,500 flight-hours per year [6]. For the purposes of this trade study, a 0% profit was implemented. The total lifetime cost is simply the sum of the unit cost and operational cost over a 25 year timespan. The results can be seen in Table 45.

Table 45 Trade Study Cost Comparison (in Millions)

Wingspan	184 ft (JJJP)	171 ft
Unit Cost	$ 168.1	$ 167.9
Lifetime Operational Cost	$ 2,648	$ 2,657
Total Lifetime Cost	$ 2,816	$ 2,825

The trade study concludes a savings of approximately $ 9,300,000 or 0.36% of the overall lifetime cost. The monetary savings may seem relatively small. However in a competitive airline industry in which profit margins are thin and one in which aircraft are bulk ordered, the overall savings are significant.

XVII. Auxiliary Systems

A. Flight Controls

The flight controls are an integral part of the systems of the aircraft. In order to do any basic function with the aircraft, the flight controls are required. Flight controls include the input to the control system, the control surfaces, and the method in which that information is brought to the control system.

This aircraft will utilize a fly-by-wire (FBW) system of flight controls. A FBW system uses a primary flight computer that sends electronic signals relayed from the pilot controls to the control surfaces instead of the conventional method of using pulleys and long lengths of cable to actuate the control surfaces. There are a few reasons why the FBW system is a better choice than the conventional flight control systems. In fact, with their decision for making the 777 a FBW system, Boeing gives the following six reasons : Overall weight reduction, integration of several systems into one, better handling of the aircraft, ease of maintenance, ease of manufacturing, and greater flexibility with changes and integration of new systems into the aircraft [62]. On the downside, the cost of the system is significantly increased, although savings from reduced weight are gained when the aircraft is in service. This is a trade off between cost now and cost later, but in the end the positive traits of the FBW system outweigh the extra cost. One of the biggest advantages for this aircraft will be the weight savings that the FBW system provides. Since this aircraft is designed for short haul missions, reducing weight is one of the biggest ways to improve efficiency. FBW also has some added safety benefits that come along with it. Because the system is running all of the controls through the primary flight computer, it is easy to enact safety protocols that aid the pilot in emergency situations as well as keeping the aircraft out of emergency situations. The use of the primary flight computer also allows for an easy integration and use of autopilot equipment, as it can easily receive inputs and feedback to fly the aircraft.

The FBW system, in order to create safety in redundancy, will employ three primary flight computers (PFC) with three lanes that each control the surfaces of the aircraft. One PFC will take input from the autopilot, while the other take input from the pilot controls. They will also be configured in a way that allows for another PFC to help out in the case of a failure or overload of another PFC. This means the system has a significant amount of redundancy that translates to a safer aircraft. Shown in Fig 55 is a basic diagram showing how the FBW system works and interacts with the aircraft to get input from the cockpit to the actuator control electronics. These electronics communicate the inputs to the actuators in order to correctly actuate at the right time. In the system, the flaps, ailerons,leading edge slats, and each side of the elevator will each have 2 actuators. The rudder will employ 3 actuators. The spoilers and trim are each slated to have one actuator.

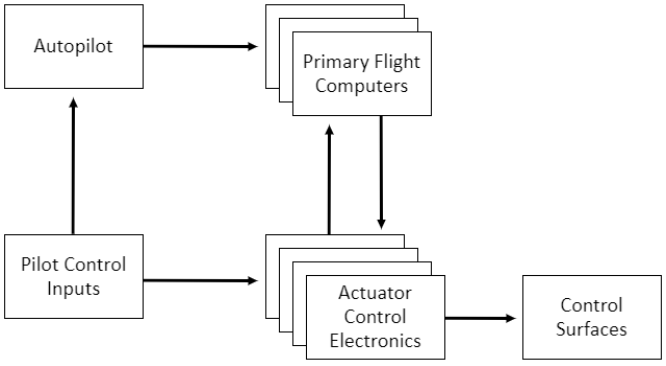

Fig. 55 Fly-by-wire flight control setup diagram

B. Engine Controls

Engine controls in the aircraft are what converts pilot input into the corresponding action within the engine. Some of the main aspects that the engine controls deal with are fuel connections, throttle input, cockpit alerts and warnings, air data requirements, fire detection and protection, engine start and restart, and engine health monitoring [63]. The JJJP, along with most other modern aircraft, will utilize a Full Authority Digital Electronic Control (FADEC) unit to control the engine and all of it's functions [63]. The FADEC will allow the integration of the engine into the flight controls with the rest of the aircraft. This integration will allow all the information that is going to and from the engine to be consolidated. The pilot can then have warning lights or buzzers from the instruments to allow proper warning if something is wrong. Doing this makes the aircraft safer without causing a data overload for the pilot. An example of the layout of the FADEC system and how it provides feedback is shown in Fig 56 [63]. The FADEC system for this aircraft will come from Rolls-Royce because they are the developers of the engine and have the technical capabilities to create a FADEC system.

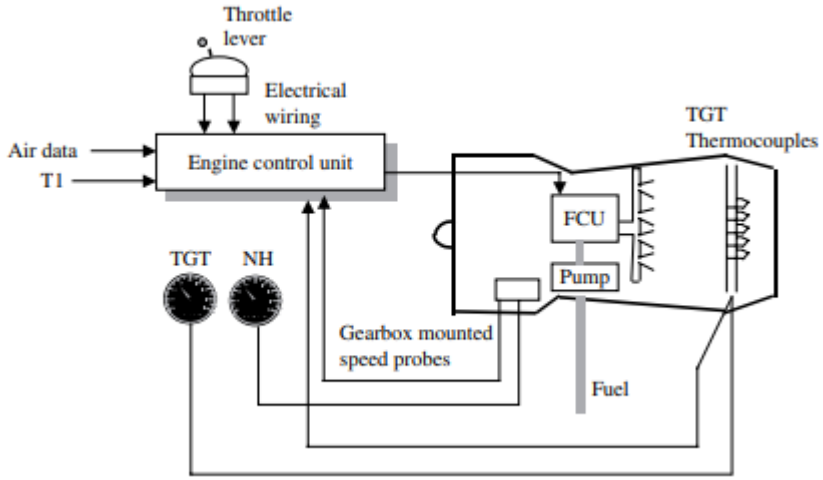

Fig. 56 FADEC setup diagram

C. Fuel System

The fuel system stores fuel in the aircraft and transports it when needed to the engines, APU, or out of the aircraft. The fuel system of the JJJP can be seen below in Fig 57. This system uses two wing tanks and one center tank. Each engine can be fed from the wing tank on its respective side, or the center tank. Fuel can also be transported from side to side, either through the center tank and into the other wing, or past the center tank altogether and into the other side. Another line that can be fed by any of the three tanks goes from the center back to the APU.

Within the fuel systems, there are a number of safety precautions that will be put into place. Check valves will be placed throughout the system to keep problems in the system isolated. Surge tanks will also be implemented in case of a decrease in fuel density while the tanks are full. The size of the surge tanks were calculated from a change in density after a temperature change of 15 °C. Finally, there will also be vent tanks that hold fuel that is about to be jettisoned in case of an emergency to decrease the weight of the aircraft. The vent tanks were sized off of historical data.

The location of the tanks inside the aircraft are shown in Fig. 58. Going from inboard to outboard, there is the center tank in the fuselage, the main wing tanks that are split up into two sections, the surge tanks, and the vent tanks. The two sections of the wing tank function as one tank, but are separated to help prevent major fuel sloshing. Each tank uses a wet wing approach, because it allows the wing to keep its internal structure, creates baffles from the ribs to help prevent sloshing, and effectively uses the space in the wing.

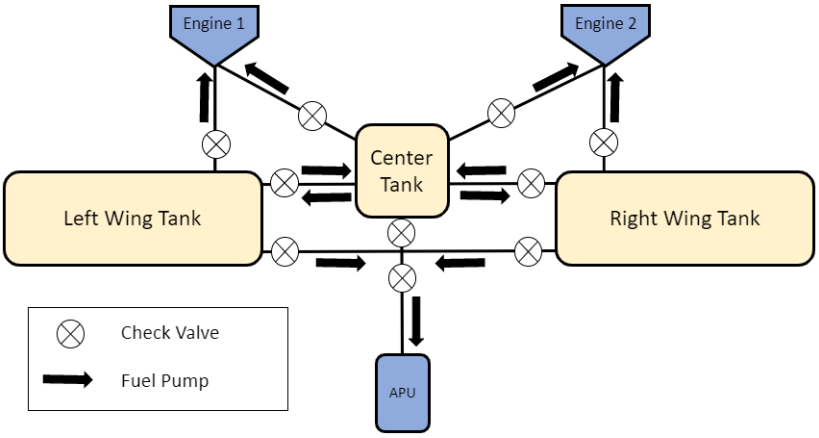

Fig. 57 Fuel system diagram

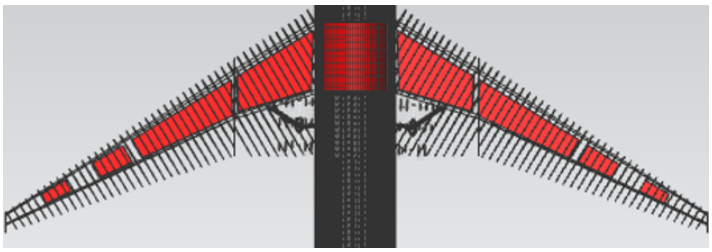

Fig. 58 Fuel tank location inside the aircraft structure

Because the maximum range required of 3,500 nmi is significantly less than any other commercial aircraft of this size, achieving the necessary fuel volume requirement was not an issue. The fuel volumes of each tank are shown in Table 46. The tank volumes were calculated using the maximum fuel volume needed at standard temperature and pressure along with the available space within the aircraft structure. The required fuel volume calculated from performance data is 19,450 gal.

Table 46 Fuel Tank Volumes

Tank	Volume (gal)
Wing	7,100
Center	5,250
Surge	300
Vent	150
Total	20,350

D. Hydraulics System

The hydraulic system of this aircraft will be used for wheel braking, nose wheel steering, flight control actuation, and high lift device actuation. Figure 59 shows a basic layout of the hydraulic system layout of the JJJP.

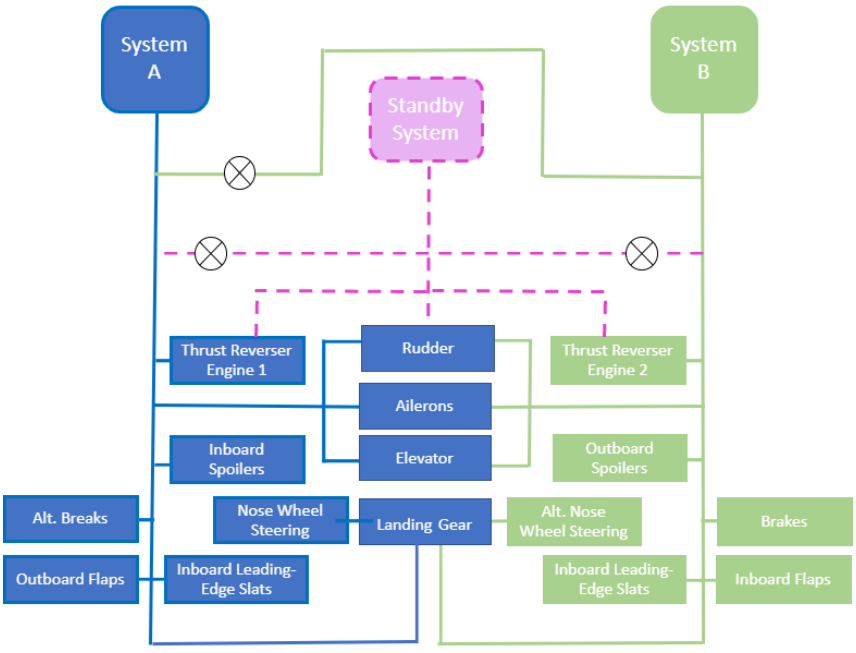

Fig. 59 Hydraulic system diagram

The two hydraulic reservoirs on the left and right side of the aircraft are the main reservoirs, and the one in the center is the standby system.The standby system will only actively be supplying pressure to the rudder of the aircraft along with thrust reversers when activated. The left and right side systems will be run off power from the engine, whereas the center standby system will be driven electrically with an option to run it using a ram air turbine in emergencies. The systems are connected so if one system fails, another can supply emergency power to continue the operations of the aircraft. Each control surface will also have at least one electric backup hydraulic actuators, which is a self contained system that would still work if all three of the hydraulic systems were compromised. This creates more redundancy in the system that leads to a safer hydraulic system overall. It should also be noted that the two main reservoirs do not exclusively operate the systems on that given side. Some control surfaces are staggered between systems so that all the control surfaces do not automatically fail when there is a problem. Instead, the other system that is still running gives partial control to each side of the wing, keeping things balanced until emergency power can be obtained. Also, fail-safes are put into place that will allow the standby reservoir or the main reservoirs to reroute power to other parts of the system in the case that one of the other reservoirs goes down. This is managed by shutoff valves that are shown in Fig. 59, along with other check valves that will be implemented in various places in the hydraulic design. As the design progresses and more specific needs of the hydraulic system are established, more specifics of the system will be put into place.

E. Electric System

The electrical system generates and provides power to all the electrical systems on the aircraft. These systems mainly consist of avionics, actuation, flight controls, and sensors. The electrical system is modeled after the Boeing 777 electrical system, because the electrical power requirements are similar based on the design of the other systems in the aircraft [64]. The power for these systems is taken from one generator on each engine as well as well as a generator on the APU. These generators provide 120 kVA of power each. Power for the electrical system is stored in one lithium-ion battery that is kept near the front of the aircraft. This battery deviates from the 777 design, but with increasing battery technology, a lithium-ion battery should not be an issue for this aircraft by 2029. From historical data, the battery was estimated to need to weigh 70 lb in order to be big enough to store the necessary power [65]. The battery requires DC power, so some other equipment must be used to convert from AC to DC and back to AC. To convert from AC to DC, a Transformer Rectifier Unit can be used. Going back to AC, a power inverter is needed. The power required for the systems in the aircraft will either run on 28 VDC or 115 VAC [64]. For systems with lower amperage requirements, 28 VDC will be used. Much of the avionics of the aircraft along with the wingtip locking actuators will run on DC. For higher amperage systems 115 VAC will be used because it can achieve a higher amperage. The power follows a path from the engines/APU to the front of the aircraft were the electrical equipment bay and battery is. The power is then distributed throughout the aircraft to all the systems that need it.

F. Pneumatic System

The pneumatic system provides air pressure to various parts of the aircraft. It does this by bleeding air out of the engine or the APU and supplying it to the necessary systems. Those systems include the environmental control system, deicing system, pressurization, engine starting, and windscreen ice/rain prevention. Figure 60 shows a simple diagram of the general layout of what will be expected on the JJJP [63].

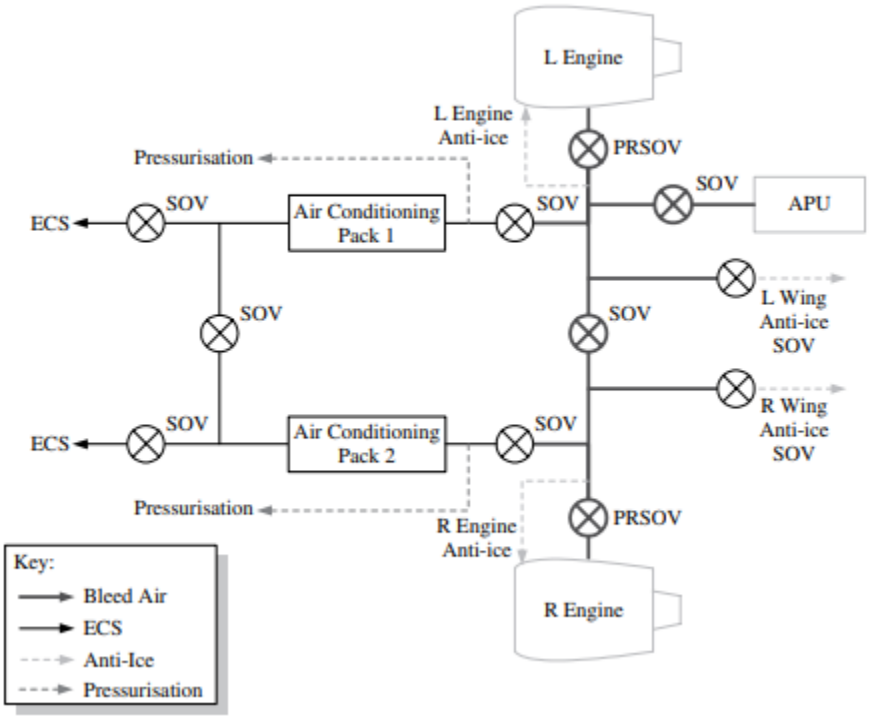

Fig. 60 Pneumatic system diagram [63]

G. Environmental Control System

The environmental control system seeks to keep the passengers comfortable and the rest of the cargo and equipment at a safe temperature. The environmental control system mainly takes bleed air from the pneumatic system and uses it take care of things within the aircraft. Its main function is to keep the cabin pressurized and at a comfortable temperature for the passengers on the aircraft. A basic diagram of what the temperature control system in the aircraft will look like is shown in Fig 61 [63]. Using this system, the cabin will be pressurized to 8,000 ft in accordance with 14 CFR Part 25.841.

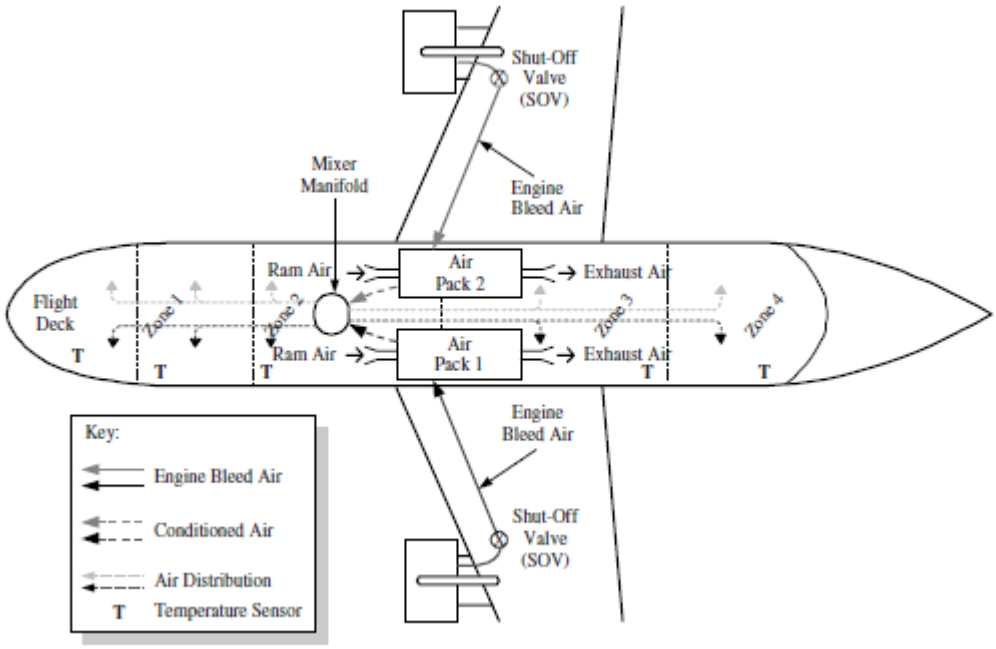

Fig. 61 Temperature control diagram [63]

Another large part of the environmental control system is keeping ice off of the aircraft. This aircraft, in order to meet RFP requirements, must have a deicing system [1]. As previously stated, the deicing power will be provided by the pneumatic system. Hot air from the engine will be brought to the leading edges of the wings, tail, engines, and windscreen. This method provides a simple yet effective way of keeping ice from building on critical areas of the aircraft. Shown in Fig 62 is a diagram of how the system will utilize the hot engine air to prevent ice on the leading edge of the wing [63].

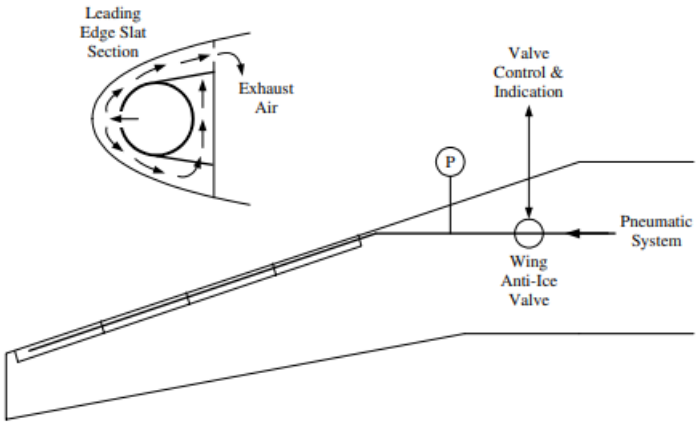

Fig. 62 Leading edge deicing diagram [63]

H. Emergency Systems

The aircraft will be equipped with emergency equipment for passengers, flight attendants, as well as the aircraft overall. Supplemental oxygen will be built into the aircraft as well as portable oxygen masks with tanks will be put into the aircraft to fulfill 14 CFR §121.333 in the FAR. Five hand fire extinguisher will be conveniently located throughout the aircraft in case of a fire. One crash axe and two megaphones will also be installed in the aircraft, all in accordance with 14 CFR §121.309. In the case of an evacuation of the aircraft, the aircraft will employ approved emergency exit slides at each exit in accordance with 14 CFR §25.810. Finally, if there is an evacuation, all of this equipment will help the passengers in order to exit in the allotted 90 seconds as stated by the FAA in 14 CFR §121.291. The aircraft will also have life preservers, life rafts with appropriately equipped survival kits, and approved locator transmitters can be installed for over-water operations in accordance with 14 CFR §121.339. For the aircraft itself, fire detectors, fire suppressants, angle of attack sensors, and other emergency equipment to report the health of the aircraft will be implemented to make the JJJP a safe aircraft for its passengers.

I. Avionics

Avionics in an aircraft manage communication, navigation, as well as integrate many other systems together in order to display relevant information to the pilot for apt decision making. It is important to have a comprehensive yet not overwhelming avionics system so that the pilot has all information and flight data necessary. However they should not bogged down with unnecessary information. The avionics should also contain redundancy in order to achieve acceptable safety standards. When looking at suppliers for more modern Boeing and Airbus aircraft, it is clear that they are trying to achieve this. They never order all their equipment from the same company and have multiple companies supplying equipment with equivalent capabilities. [66, 67].

For example, the Boeing 777 is using both Honeywell and Collins Aerospace for the majority of their flight and data management systems [67]. Honeywell Aerospace supplies Boeing with AIMS, which integrates the multiple functions of avionics into one single system [67]. Collins Aerospace also provides the B777 with flight control systems that are used on the aircraft [67]. If they were to only use one avionics manufacturer, they run the risk of the company having the same problem in different parts of the avionics because the problem was not found. Because these are different systems created by different companies, they are much less likely to fail at the same time or exhibit the same problem.

The JJJP will be using an Integrated Modular Avionics(IMA) for its Flight Management System(FMS). IMA is the opposite of the traditional federated architectures, and its concept is very similar to a desktop computer, where everything gets processed by the centralized processing units. That is, the IMA is essentially a "barebones computer" that allows for increased customization. The caveat being that all the modules need to be compatible. By having IMA, the number of line replaceable units(LRU) is significantly lower. For example, Boeing utilized the IMA approach to off shave 2,000 pounds off the avionics suite of the new Boeing 787 [68]. IMA is an economic solution to avionics because

of its flexibility, weight savings, and maintenance savings. Figure 63 demonstrated that Federated system require every LRU to have its own processor. In contrast, IMA uses a centralized processor, and it will reduce the communication needed for its systems. Thus, IMA reduces weight and complexity [69]. The following IMA architecture commonly used by major commercial aircraft were put into comparison: Rockwell Collins Pro Line Fusion, Honeywell Aerospace Airplane Information Management System (AIMS), and General Electric Common Core System(CCS). The Pro Line Fusion was commonly seen in smaller aircraft such as the Airbus A220 and the Bombardier Global 5000, and Honeywell AIMS was used on older Boeing 777. GE CCS was determined to be the JJJP's avionics integrator, because it was used on the Boeing 787 Dreamliner as well as the new Boeing 777X. Ultimately, the GE Common Core System was chosen to be the JJJP's avionics integrator, because the other two option was simply eliminated. The Pro Line Fusion only exists in small commercial aircraft and business jets. On the other hand, the Honeywell AIMS was an IMA used in older Boeing 777. CCS is a promising solution to avionics. According to GE, CCS saves hundreds of pounds of weight by having less wiring, therefore reduced fuel cost [70].

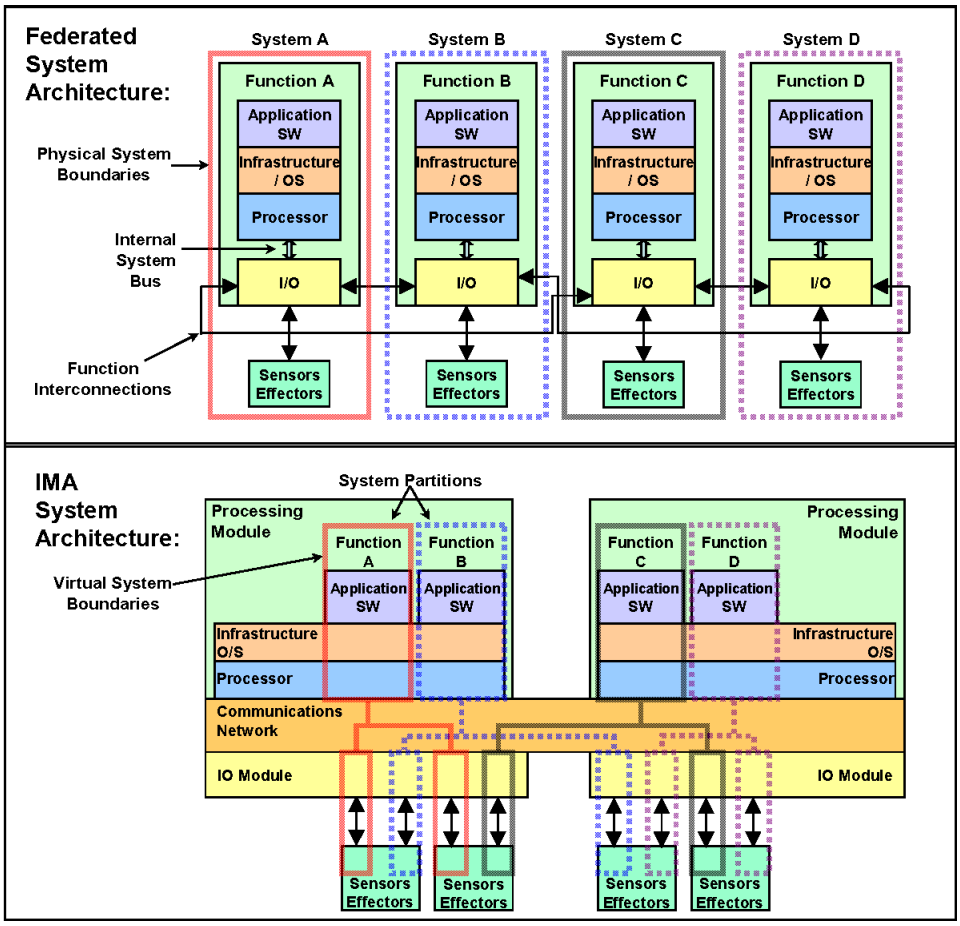

Fig. 63 A Comparison of federated system and IMA system.

For avionics integration, systems of the Boeing 787 Dreamliner was used, which is listed in Table 47 [71]. One important note here is systems will come with packages. For example, Honeywell navigation package comes with inertial reference system, air data system, and multi-mode receiver [71]. As well as pitot tube, instrument landing system (ILS), GPS, GPS landing system (GLS), and VHF omni-directional radio range (VOR) from the Honeywell Multi-mode receiver. On other hand, the Collins Aeropsace ISS-2100 package offers weather detection, traffic alert, and collision avoidance. Additionally it has terrain awareness and warning function integrated into a single system [72]. The system was capable of VFR and IFR flight with the navigation package, along with autopilot from Honeywell. In extreme weather condition, Honeywell flight control offers CAT II approach, windshear guidance, and integrated thrust management [73].

Table 47 List of Integrated Avionics

Category	System	Model
Communication	Airborne Communitcation Systems	Avionica satLINK Iridium communications gateway
Communication	Communication Antennas	Cobham SATCOM HGA-7001 high gain satcom antenna system
Communication	Radio Communications Equipment	Collins Aerospace Communications system
Communication	Communication Antennas	HR Smith Antennas
Flight and Data Management	Flight Management Systems	GE Aviation Systems Common Core System (CCS)
Flight and Data Management	Operating System	Green Hills Software Integrity-178B operating software
Flight and Data Management	Avionics Management Systems	Collins Aerospace Avionics Management Systems package
Flight and Data Management	Flight Control System	Honeywell Aerospace Flight Controls and Autopilots
Indicators and Instruments	Electronic Flight Instrument Systems	Collins Aerospace LCD Displays & Fuel Quantity Indicators
Indicators and Instruments	Electronic Flight Instrument Systems	Thales Avionics Electronic Flight Instrument Systems
Navigation & Guidance	Navigation Aids	Honeywell Aerospace Navigation package
Warning Systems	Configurable Integrated Surveillance System	Collins Aerospace ISS-2100 package

XVIII. Cost Analysis

A. RDTE & Flyaway Cost

Two methods were utilized for estimating the research, design, testing, and evaluation (RDTE) cost and flyaway cost. The first was the RAND DAPCA IV model as specified in Raymer [6]. DAPCA IV is a cost model developed by the RAND corporation which estimates the amount of hours necessary for RDTE and flyaway (production) in terms of engineering, tooling, manufacturing, and quality control. The hours are then multiplied by their respective labor rates, from which the total RDTE and flyaway costs can be determined. The second method is laid out in Roskam VIII [61]. It follows a similar process of estimating manhours and process costs, but is higher fidelity and uses more aircraft parameters as inputs.

Certain economic factors were assumed. The DAPCA IV cost model is calibrated to 2012 and the Roskam model is calibrated to 1989. As such, the respective historical inflation rates were utilized between that time and 2020 based off the U.S. Bureau of Labor Statistics (BLS) data [74]. From there, a steady 2% inflation rate was assumed between 2020 and 2029. In calculating unit cost, a 15% profit margin was also applied. The final cost estimations are presented in Table 48.

Table 48 RDTE & Flyaway Cost (in Millions)

Methodology	Production Quantity	RDTE	Flyaway
DAPCA IV	500	$ 7,000	$ 99,200
	1000	$ 7,800	$ 178,000
	2000	$ 8,700	$ 325,200
Roskam	500	$ 3,200	$ 86,500
	1000	$ 3,200	$ 164,800
	2000	$ 3,200	$ 317,100

One result of this estimation is that RDTE cost is fairly constant across various production runs. This is because the majority of these costs are incurred well before production begins. Flyaway cost increases as expected considering that the main component is manufacturing. The result of this is that unit cost decreases with higher production runs due to the production learning curve.

B. Direct Operating Cost

Direct operating costs were estimated utilizing approximations from Raymer [6]. This includes fuel, crew, maintenance, depreciation, and insurance costs. Fuel costs were based on the fuel burn and mission time for a 700 nmi flight. For the JJJP, a two-man cockpit crew was assumed. Regarding maintenance, 10 manufacturing manhours per flight-hour was implemented. The depreciation model was based on a 90% value loss over a 12 year lifespan. The final results are presented in Table 49.

Table 49 Operating Cost (Top Row - $/Hour, Bottom Row - $/Year)

Flight-Hours per Year	2500	3500	4500
Fuel	$ 10,100	$ 10,100	$ 10,100
	$ 25,300,000	$ 35,400,000	$ 45,500,000
Crew	$ 1,010	$ 1,010	$ 1,010
	$ 2,530,000	$ 3,540,000	$ 4,550,000
Maintenance Crew	$ 1,130	$ 1,130	$ 1,130
	$ 2,820,000	$ 3,940,000	$ 5,070,000
Maintenance Material	$ 6,080	$ 6,080	$ 6,080
	$ 15,200,000	$ 21,300,000	$ 27,400,000
Depreciation	$ 4,220	$ 3,010	$ 2,340
	$ 10,500,000	$ 10,500,000	$ 10,500,000
Insurance	$ 520	$ 490	$ 480
	$ 1,300,000	$ 1,720,000	$ 2,140,000
Direct Operating	$ 24,780	$ 23,540	$ 22,850
	$ 61,900,000	$ 82,400,000	$ 102,800,000

C. Unit Cost

Unit cost was estimated utilizing two separate methodologies. The first was using both the DAPCA IV and Roskam CER. RDTE + Flyaway costs were simply divided by the production quantity to determine a unit cost. The second was by reviewing historical data. A simple analysis was done of aircraft empty weight vs. unit cost. The data included aircraft from the Boeing commercial aircraft family (B737, B747, B767, B777) [75]. A linear line of best fit was calculated, and then a unit cost was determined based off the JJJP empty weight. The slope of the line of best fit is

about $914 per pound. This matches a rough rule-of-thumb quoted in Raymer of about $800 per pound [6]. The data is presented in Fig. 64.

A summary of all results are presented in Table 50. The unit costs from the DAPCA IV and Roskam method are lower than that of the historical data analysis. Sources of error for this estimate are discussed in the model uncertainties section.

Table 50 Unit Cost Results (in Millions)

Production Quantity	DAPCA IV	Roskam	Historical
500	$ 233.5	$ 196.9	$ 240.2
1000	$ 204.3	$ 184.5	
2000	$ 183.6	$ 176.0	

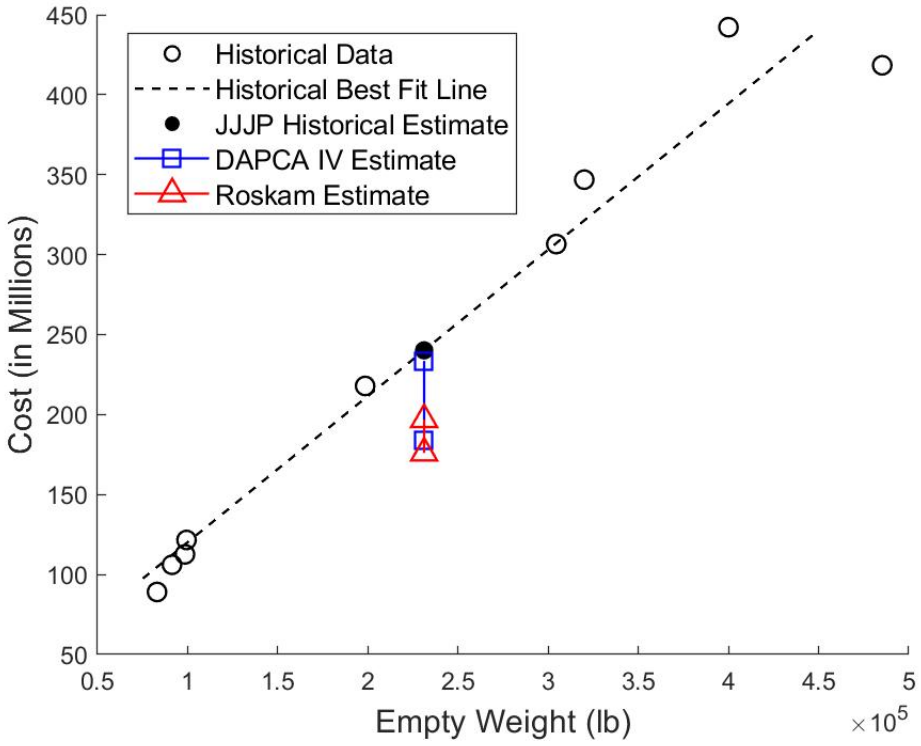

Fig. 64 Empty weight vs. unit cost

D. Cost Reduction Methods

The main design objectives of this aircraft are to minimize manufacturing and operating cost. As such, a number of cost reduction methods have been considered. One design decision was the choice of material for the airframe. The 3 main options were a fully aluminum structure, a fully composite structure, and a partial aluminum-composite structure (B777X). Composite frames provide a higher fuel efficiency which is beneficial for long range missions, however there are diminishing returns as range decreases. Simply from a manufacturing and maintenance standpoint, it was decided to pursue a fully aluminum frame for the entire aircraft.

Another set of methods are centered around the passenger experience. Recently, many low-cost carriers have been able to reduce operating costs while maintaining a consumer base. One example is installing Wi-Fi for in-flight entertainment as opposed to in-seat entertainment. This would benefit the customer and result in a lower systems weight/cost, however the antenna and radome necessary for this increases the fuselage skin friction drag. Another method is choosing lightweight seats with lower padding compared to normal seats. The shorter 700 nmi mission time means that passengers won't be as susceptible to strain as on a long-haul flight.

One cost reduction method that was explored was a windowless airframe. This concept is fairly simple. The removal of all cabin windows results in significant loss in structural weight. To maintain passenger comfort, high quality television panels would be setup throughout the cabin to visualize the exterior and replicate windows. A preliminary sizing paper by the University of Bologna estimated about 3,200 lb for a Boeing 777 type aircraft [76]. This accounts for structural weight savings and electronics weight gains. The implementation of a windowless airframe would result in reduced fuel burn and manufacturing costs but slightly higher operating and maintenance costs. The overall fuel cost and emissions savings for an airline would be significant. However, the ticket price savings for a passenger would be approximately $ 6 for a 700 nmi mission. It was then assessed that the average consumer would likely not find this tradeoff worth the potential discomfort of flight, and the concept was not further pursued.

E. Model Uncertainties

The models used in this section are fairly low fidelity and are subject to many sources of error propagation. One is lack of knowledge in the pricing models of third-party suppliers. Pricing of specific onboard auxiliary systems and avionics modules are not directly known. Avionics cost was calculated using a weight based estimation of $ 4,500 per pound as suggested by Raymer [6]. However, the JJJP does not use systems or avionics that stray significantly from the industry average, so the magnitude of error should be minor.

This cost model is also unable to account for possible technical delays during the development phase which would result in a higher RDTE cost than predicted. The majority of the aircraft uses design features with high technology readiness levels (aluminum airframe, folding wingtips, FBW system). However, the UltraFan engine utilized will push technological boundaries in terms of blade design and efficiency. As such, potential time delays and budget overruns

could come about.

Finally, this model is not able to account for pure economic factors that are present at large firms. For example, while a unit cost can be estimated, heavy discounts are often given to airlines that purchase bulk orders. Also, financial factors such as interest rates, profit margins, and inflation are realistically more complex than modeled in this report. Labor in the form of engineering, manufacturing, and support is not subject to constant hourly rates as specified in DAPCA IV. For example, airframe manufacturing in the United States is heavily influenced by labor union agreements.

XIX. Environmental Considerations

A. Acoustics

When considering the acoustic profile of the aircraft there are three locations at which sound levels are measured with limits set by the size and year of certification. The three measurements taken are lateral, flyover, and approach. Lateral is the full power reference noise measurement point at a distance of 1,476 ft from the center line of the runway. The flyover measurement is taken at a distance of 21,325 ft from the start of takeoff roll, while approach is the measurement taken at a distance of 6,561 ft from the centerline of the runway threshold [77]. For the JJJP, the noise levels allowed depend on the maximum takeoff weight as well as time of certification. The exact levels of each stage were found by using Fig. 67 [78].

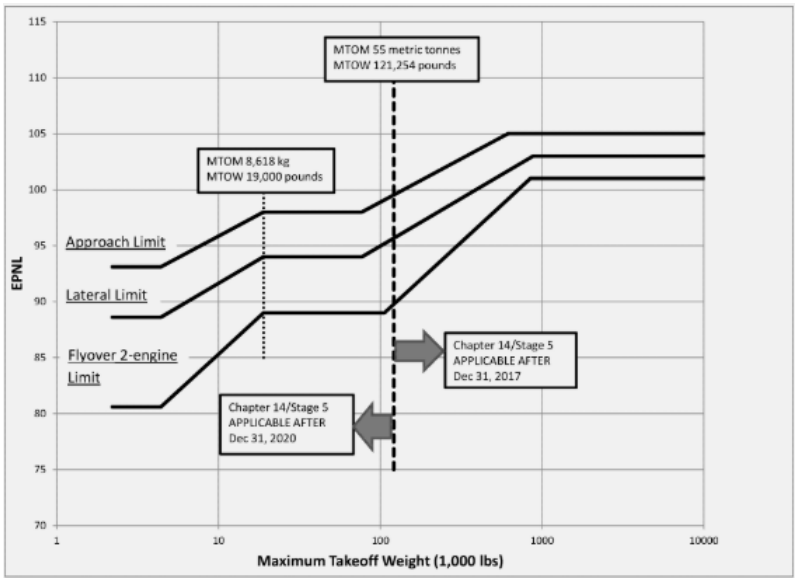

Fig. 65 Noise requirements for Stage 5 aircraft

From this the noise levels that need to be met at each limit were determined to be 97 EPNdB for flyover, 101 EPNdB for lateral, and 103 EPNdB for approach. To know whether or not these levels can be met, acoustic data was taken from the European Aviation Safety Association (EASA) database[79]. Information regarding the noise measured at each

location along with the exact engine model used was gathered. Following the trends observed from this information would then allow for an estimation to be made of the acoustic profile of the JJJP, with the result shown in 66.

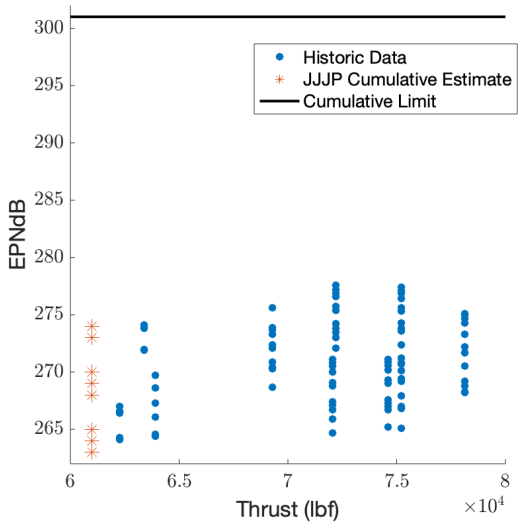

(a) Cumulative noise level estimate

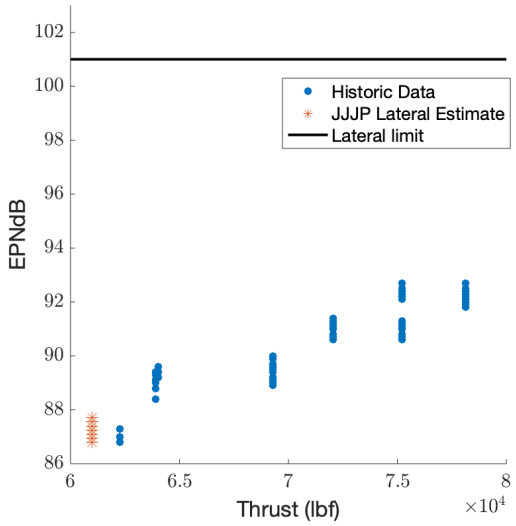

(b) Thrust effects on lateral noise levels

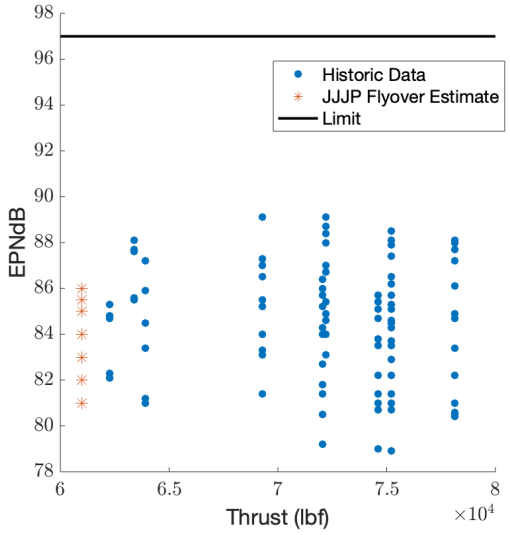

(c) Thrust effects on flyover noise levels

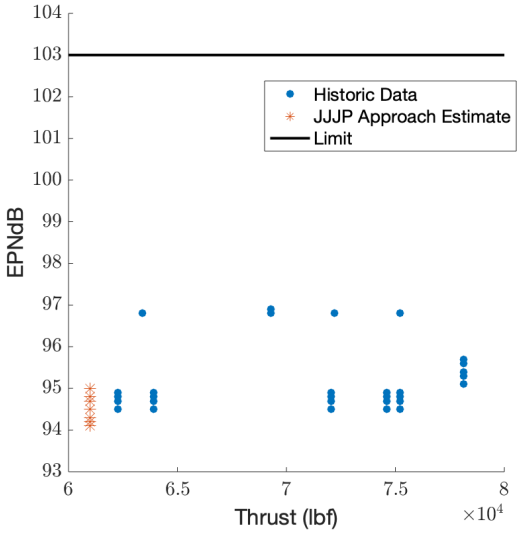

(d) Thrust effects on approach noise levels

Fig. 66 Acoustics data showing effects of thrust on the noised produced at each stage

From this, the effects of thrust can be seen in the lateral section, with a trend of increased noise with an increase in thrust as this is the position where max thrust must be used. When using this data to see where the JJJP will be in terms of noise produced, the plane is expected to use 62,500 lb of thrust per engine during takeoff and following the trend that puts it near 86-88 EPNdB. This range is well under the 101 EPNdB allowed for a stage 5 aircraft. For flyover, the results are somewhat less clear, as it is very common for aircraft to cut back on power when approaching this location in order

to meet the noise requirement, thus thrust has less of an effect on the noise seen at this location [77]. If assuming worst case scenario base on this data, the maximum noise produced by the engine to be used on this aircraft would range between 81-86 EPNdB which is well below the limit of 97 EPNdB allowed. At approach it can be seen that thrust has almost no effect on the noise produced as during this stage the engines are most often near idle producing very little thrust and noise . The outliers in this data may be due to airframe noises that con sometimes be unavoided due to the construction of the aircraft or aborted landings requiring an increasing in thrust and thus noise produced . By following the trends of other aircraft, the noise produced for this aircraft can be estimated at 94-95 EPNdB that is still under the allowed limit of 103 EPNdB allowed by the stage 5 requirements.

There are some uncertainties when creating a model like this based purely on historical data of engines. This is even more the case in this situation as the JJJP is planning on using the Rolls Royce UltraFan engine which currently has not yet entered service, so there is no acoustics data available for this exact model. In order to estimate the noise being produced, different variations of the Rolls Royce Trent 1000 were investigated as this is the closest engine on the market at this time to the UltraFan. Although, since the Ultrafan does have a bypass ratio much larger than most engines on the market today, these estimates for the acoustic profile are very conservative. With a low bypass ratio engine, the exit velocity of the air through the engine is much lower resulting in a more quiet and less turbulent exhaust overall. This reduces the noise produced when compared to an engine with similar thrust but lower bypass ratio. Another uncertainty comes with construction of the aircraft and noises that it may make when flying that are very hard to model and predict at this stage in design.

B. Emissions

In terms of environmental concerns, the emissions profile of this aircraft is of upmost importance, especially with trends in political and social movements demanding for more consideration of the effects all industries have on the environment. One of the added benefits of having such an efficient aircraft and engine such as the JJJP and Rolls Royce UltraFan is the increased performance allows for less fuel to be burned per mile than some older planes on the market with outdated technology. To get an accurate estimation of the total emissions to be expected from this aircraft, the total flight hours per year ranged from 2500 to 4500 hours and an average life span of 25 years was predicted from this aircraft to get an idea of the total emissions produced from flight of this aircraft. The results of this can be seen below in Table 51.

Table 51 Lifetime Emissions Estimate

Flight Hours per Year	2500	3500	4500
CO_2 Produced	1,04,500 MT	1,456,500 MT	1,872,500 MT

The results in Table 51 not only include the emissions from the total flight hours, but also a fixed amount associated with the emissions of manufacturing. The production of metal is a very high energy process, thus there are usually high amounts of emissions generated from it. Since this aircraft is largely comprised of aluminum, it was estimated that for every pound of aluminum, 9.2 pounds of CO_2 are produced [80]. This estimate can be further refined if specific manufacturing processes are investigated deeper as well as looking into using recycled materials to further reduce the total emissions as well as cost of the aircraft.

XX. Conclusion

A new type of high capacity short range aircraft is necessary to adjust for a developing global airline market. The AIAA RFP outlines the requirements for a potential aircraft with complementary design objectives. The major constraints are a 400 passenger capacity and 3,500 nmi range. Design objectives are to minimize operational and production cost. Given this problem statement, the JJJP was designed.

The JJJP features a conventional tube-and-wing design. It can carry a nominal payload of 93,400 lb to a maximum range of 3,500 nmi at a cruise speed of Mach 0.78. A high aspect ratio wing and UltraFan engines ensure high efficiency at an affordable cost. The 7 ft folding wingtips allow it to operate out of Group IV airports. The MTOW and empty weight are 443,000 lb and 241,500 lb respectively. Entry into service is expected in 2029 at a unit cost of $ 180 million. JJJP is able to meet all RFP requirements and all major FAA requirements.

Based upon all assessments in this report, the JJJP design does not contain any flaws that would require revision. As such it can be recommended for further detailed design and production.

Fig. 67 JJJP CAD rear view

XXI. References

[1] "Request for Proposal High Capacity Short Range Transport Aircraft," , 2020. URL https://www.aiaa.org/docs/default-source/uploadedfiles/education-and-careers/university-students/design-competitions/undergraduate-team-aircraft-design-competition/undergraduate-aircraft-high-capacity-short-range-transport-aircraft.pdf?sfvrsn=b6081273_0.

[2] "Boeing 777 Specs, what makes this giant twin work?" , 2020. URL http://www.modernairliners.com/boeing-777/boeing-777-specs/.

[3] "Boeing 787 Dreamliner Specs," , 2020. URL http://www.modernairliners.com/boeing-787-dreamliner/boeing-787-dreamliner-specs/.

[4] "787 Airplane Characteristics for Airport Planning," , 2018.

[5] "GENX high bypass turbofan engines," , 2004.

[6] Raymer, D. P., *Aircraft design: a conceptual approach*, American Institute of Aeronautics and Astronautics, 1989.

[7] Roskam, J., *Layout Design of Cockpit, Fuselage, Wing, and Empennage: Cutaways and Inboard Profiles*, DARcorporation, 1997.

[8] "AC 150/5300-13A," , 2014. URL https://www.faa.gov/documentLibrary/media/Advisory_Circular/150-5300-13A-chg1-interactive-201907.pdf.

[9] Dix-Colony, K., "Operating the 747-8 at Existing Airports," *AERO*, 2010. URL https://www.boeing.com/commercial/aeromagazine/articles/2010_q3/3/.

[10] Wall, M., "Stratolaunch to launch hypersonic vehicles from world's biggest airplane," 2020. URL https://www.space.com/stratolaunch-hypersonic-vehicles-worlds-biggest-airplane.html.

[11] Morales, J., "The A380 Transport Project and Logistics," , 2006.

[12] Mai, T., "Technology Readiness Level," , 2017.

[13] Street, F., "Are windowless planes the future of travel?" 2019.

[14] "AC 25.773-1," , 1993. URL https://www.faa.gov/documentlibrary/media/advisory_circular/ac_25_773-1.pdf.

[15] "ULD Container Types: LD-3," , 2020. URL https://www.searates.com/reference/ld3/s.

[16] "TP400-D6 ENGINE – THE MOST POWERFUL TURBOPROP ENGINE IN PRODUCTION," , 2020. URL http://www.europrop-int.com/the-tp400-d6/.

[17] Mark, "Elasticity of Demand for Air Travel," 2015. URL https://econfix.wordpress.com/2015/05/07/elasticity-of-demand-for-air-travel/.

[18] NTSB, "Aircraft Accident Report AA191 Chicago O'Hare May 25 1979," , 1979.

[19] "EASA type-certificate data sheet GEnX," , 2020. URL https://www.easa.europa.eu/sites/default/files/dfu/TCDS%20IM%20E%20102_issue10_20191213.pdf.

[20] "EASA type-certificate data sheet Trent 1000/7000," , 2020. URL https://www.easa.europa.eu/sites/default/files/dfu/TCDS%20E%20036%20issue%2016_20191105.pdf.

[21] Kjelgaard, C., "Rolls-Royce UltraFan Design Frozen," 2018. URL https://www.ainonline.com/aviation-news/air-transport/2018-07-16/rolls-royce-ultrafan-design-frozen.

[22] O'Connor, K., "Rolls-Royce Begins Building UltraFan Demonstrator," 2020. URL https://www.avweb.com/ownership/engines/rolls-royce-begins-building-ultrafan-demonstrator/.

[23] "EASA type-certificate data sheet Trent XWB," , 2020. URL https://www.easa.europa.eu/sites/default/files/dfu/EASA%20E111%20TCDS%20issue%2012_Trent%20XWB.pdf.

[24] "EASA type-certificate data sheet GE-90," , 2020. URL https://www.easa.europa.eu/sites/default/files/dfu/EASA%20TCDS%20IM%20E%20002_GE90%20series_Issue4_Final_18Dec2019.pdf.

[25] Bensel, A., "Characteristics of the Specific Fuel Consumption for Jet Engines," 2018. URL https://slack-files.com/files-pri-safe/TST914E8Z-FTU9VALSF/characteristics_of_the_specific_fuel_consumption.pdf?c=1583735532-9a0b3b403a89e214.

[26] Dimitriadis, G., and Léonard, O., "Aircraft Design: Aircraft Propulsion," 2018. URL http://www.ltas-cm3.ulg.ac.be/AERO0023-1/ConceptionAeroTurbomachine.pdf.

[27] "Airfoil Tools," , 2020. URL http://airfoiltools.com/search/index.

[28] "Boeing 777 Specs, what makes this giant twin work?" , 2017. URL http://www.modernairliners.com/boeing-777/boeing-777-specs/.

[29] Roskam, J., *Airplane Design Airplane Design Part VI: Preliminary Calculation of Aerodynamic Thrust and Power Characteristics*, DARcorporation, 1997.

[30] Rodrigo Martinez-Val, E. P., and Palacin, J., "Historical Perspective of Air Transport Productivity and Efficiency," 2012.

[31] Rudolph, P. K. C., *High-Lift Systems on Commercial Subsonic Airliners*, National Aeronautics and Space Administration, September 1996.

[32] Harry L. Morgan, J., *Experimental Test Results of Energy Efficient Transport (EET) High-Lift Airfoil in Langley Low-Turbulence Pressure Tunnel*, Langley Research Center, December 2002.

[33] R. C. Feagin, e. a., *Delta Method, an Empirical Drag Buildup Technique*, Lockheed - California Company, 1978.

[34] Nicolai, L. M., and Carichner, G. E., *Fundamentals of Aircraft and Airship Design, Volume 1 – Aircraft Design*, AIAA, 2010.

[35] Hamilton, S., and Fehrm, B., "737 MAX 8 could be enabler for some LCC Long Haul," 2014. URL https://leehamnews.com/2014/12/08/737-max-8-could-be-enabler-for-some-lcc-long-haul/.

[36] Bhaskara, V., "ANALYSIS: A320neo vs. 737 MAX: Airbus is Leading (Slightly) – Part II," 2016. URL https://web.archive.org/web/20160206082857/http://airwaysnews.com/blog/2016/02/05/a320neo-vs-737-max-pt-ii/.

[37] "Data A: Aircraft Data File Table 4: Boeing Aircraft," , 2001. URL https://booksite.elsevier.com/9780340741528/appendices/data-a/table-4/table.htm.

[38] "Boeing 787 -8 (Dreamliner) sample analysis. (2005)," , 2006. URL http://www.lissys.demon.co.uk/samp1/index.html.

[39] Torenbeek, E., *Advanced Aircraft Design: Conceptual Design, Analysis and Optimization of Subsonic Civil Airplanes*, John Wiley Sons Ltd., 2013.

[40] "Wing Design-Selection of Wing Parameters," , 2020. URL https://nptel.ac.in/courses/101/106/101106035/.

[41] Sadraey, M. H., *Aircraft Design A Systems Engineering Approach*, John Wiley Sons, Ltd, 2013.

[42] McCormick, B. W., *Aerodynamics, Aeronautics, and Flight Mechanics*, John Wiley & Sons, Inc, 1995.

[43] Scholz, D., "Aircraft Design," , 2017. URL https://www.fzt.haw-hamburg.de/pers/Scholz/HOOU/.

[44] "AC 25-7D," , 2018. URL https://www.faa.gov/documentLibrary/media/Advisory_Circular/25-7D.pdf.

[45] Roskam, J., *Airplane Design Part V: Component Weight Estimation*, DARcorporation, 1997.

[46] Jordan, K. B., *Care and Repair of Advanced Composites*, SAE International, 1998.

[47] "MatWeb Material Property Data," , 1996. URL http://www.matweb.com/Search/MaterialGroupSearch.aspx?GroupID=178.

[48] "AISI 4340 Steel, normalized, 100 mm (4 in.) round," , 1996. URL http://asm.matweb.com/search/SpecificMaterial.asp?bassnum=M434AE.

[49] "S-Glass Fibre," , 2001. URL https://www.azom.com/properties.aspx?ArticleID=769.

[50] Niu, M. C.-Y., *Airframe structural design*, SAE International, 1998.

[51] "Boeing 777 Wing Test," , 2010. URL https://www.youtube.com/watch?v=Ai2HmvAXcU0.

[52] "Pushing the A350 XWB to the brink," , 2013. URL https://www.youtube.com/watch?v=B74_w3Ar9nI.

[53] "Thin Walled Vessel," , 2006. URL http://www.eng.fsu.edu/~kalu/ema4225/lec_notes/Web%20Class_6_final.

[54] "Lissys Ltd opens up its Boeing 787 analytic performance tool," 2008. URL http://www.lissys.uk/boeing787.html.

[55] Torenbeek, E., *Synthesis of Subsonic Airplane Design*, Kluwer Academic Publishers, 1982.

[56] Roskam, J., *Airplane Design Airplane Design Part VI: Layout Design of Landing Gear Systems*, DARcorporation, 1997.

[57] Roskam, J., *Preliminary Configuration Design and Integration of of the propulsion system*, DARcorporation, 1997.

[58] "Global Aviation Tires," , 2018. URL https://www.goodyearaviation.com/resources/pdf/databook-6-2018.pdf.

[59] "Hydraulic Rotary Actuator - LTR Series (light duty)," , 2017. URL https://ph.parker.com/us/en/hydraulic-rotary-actuator-ltr-series-light-duty.

[60] "Actuation and Motion Systems Product Guide," , 2010. URL https://www.moog.com/content/dam/moog/literature/MCG/actprodguide.pdf.

[61] Roskam, J., *Airplane Cost Estimation: Design, Development, Manufacturing and Operating*, DARcorporation, 1997.

[62] Bartley, G. F., "Boeing B-777: Fly-By-Wire Flight Controls," 2001. URL https://www.davi.ws/avionics/TheAvionicsHandbook_Cap_11.pdf.

[63] Moir, I., and Seabridge, A., *Aircraft Systems: Mechanical, Electrical, and Avionics Subsystems Integration*, John Wiley & Sons Ltd, 2008.

[64] Andrade, L., and Tenning, C., "Design of Boeing 777 electric system," *Aerospace and Electronic Systems Magazine, IEEE*, Vol. 7, 1992, pp. 4 – 11.

[65] "Batteries and Advanced Airplanes," , 2016. URL https://787updates.newairplane.com/787-Electrical-Systems/Batteries-and-Advanced-Airplanes.

[66] "Airbus A320," , 2020. URL http://www.airframer.com/aircraft_detail.html?model=A320.

[67] "Boeing 777," , 2020. URL http://www.airframer.com/aircraft_detail.html?model=B777.

[68] Ramsey, J. W., "Integrated Modular Avionics: Less is More," 2007. URL https://www.aviationtoday.com/2007/02/01/integrated-modular-avionics-less-is-more/.

[69] Watkins, C., *Integrated Modular Avionics: Managing the Allocation of Shared Intersystem Resources*, AIAA, 2006.

[70] Wagenen, J. V., "GE Aviation to Bring Common Core System to Boeing 777X," 2014. URL https://www.aviationtoday.com/2014/12/22/ge-aviation-to-bring-common-core-system-to-boeing-777x/.

[71] "Boeing 787 Dreamliner," , 2019. URL http://www.airframer.com/default.html.

[72] "ISS-2100 Configurable Integrated Surveillance System," , 2020. URL https://www.collinsaerospace.com/en/what-we-do/Commercial-Aviation/Flight-Deck/Surveillance/Integrated-Surveillance/Iss-2100-Configurable-Integrated-Surveillance-System.

[73] "Flight Controls and Autopilots," , 2020. URL https://aerospace.honeywell.com/en/learn/products/cockpit-systems-and-displays/flight-controls-and-autopilots.

[74] "CPI Inflation Calculator," , 2020. URL https://data.bls.gov/cgi-bin/cpicalc.pl.

[75] StartupBoeing, "ABOUT BOEING COMMERCIAL AIRPLANES," 2018. URL http://www.boeing.com/company/about-bca/#/prices.

[76] Bagassi, S., *PRELIMINARY DESIGN OF A LONG RANGE WINDOWLESS AIRCRAFT CONCEPT*, *Department of Industrial Engineering, University of Bologna, 2018.

[77] "Noise Certification," , 2006. URL https://www.icao.int/Meetings/EnvironmentalWorkshops/Documents/Noise-Certification-Workshop-2006/Boettcher_3.pdf.

[78] "Stage 5 airplane noise standards," , 2017. URL https://www.federalregister.gov/documents/2017/10/04/2017-21092/stage-5-airplane-noise-standards.

[79] "EASA certification noise levels," , 2020. URL https://www.easa.europa.eu/easa-and-you/environment/easa-certification-noise-levels.

[80] "Amounts of CO2 Released when Making Using Products," , 2012. URL http://www.co2list.org/files/carbon.htm#RANGE!A83.